Fabrication of 1-Dimensional Nanowires from Genetically Modified M13 Phage through Surfactant-mediated Hybridization and the Applications in Medical Diagnosis, Energy Devices, and Catalysis

by

Youjin Lee

B.S. & M.S. Seoul National University

SUBMITTED TO THE DEPARTMENT OF
MATERIALS SCIENCE AND ENGINEERING
IN PARTIAL FULFILLMENT OF THE REQUIREMENT FOR THE DEGREE OF

DOCTOR OF PHILOSOPHY

AT THE
MASSACHUSETTS INSTITUTE OF TECHNOLOGY
JUNE 2010

Signature of Author: _____

Department of Materials Science and Engineering

May 10, 2010

Certified by: _____

Angela M. Belcher

Professor Materials Science and Engineering and Biological Engineering

Thesis Supervisor

Accepted by: _____

Christine Ortiz

Chair, Departmental Committee on Graduate Students

Fabrication of 1-Dimensional Nanowires from Genetically Modified M13 Phage through Surfactant-mediated Hybridization and the Applications in Medical Diagnosis, Energy Devices, and Catalysis

by

Youjin Lee

Submitted to the Department of Materials Science and Engineering on May 10, 2010 in Partial Fulfillment of the Requirement for the Degree of Doctor of Philosophy in Materials Science and Engineering

ABSTRACT

Biological building blocks served as excellent templates for the preparation of various nano-materials due to their beneficial interactions at the molecular level. The bio-mineralization of genetically engineered M13 bacteriophage resulted in one-dimensional nanowires having outstanding properties in diverse applications. As a bridge between the chemical synthesis of nanostructures and the bio-mineralization of M13 phage, surfactant molecules were introduced to the biological systems. The specific affinity of M13 phage with Au-binding peptides was strong enough to attract Au ions despite the existence of surfactant molecules. Consequently, the surfactant-mediated bio-mineralization of M13 phage enabled us to precisely control the morphologies and structures in nanometer scale.

The Au-binding M13 phage could also integrate other noble metals (Ag/Pt/Pd) to prepare homogeneous Au-based noble metal alloy nanowires in structures and compositions, and their electrochemical properties upon the systematic changes in compositions were investigated. Especially for the Au-Pt system, the catalytic activity study on the two distinct structures, the alloy and the core/shell, provided us important factors to design new catalysts with optimized activities.

Thesis Advisor: Angela M. Belcher

Title: Germeshausen Professor of Materials Science and Engineering and Biological Engineering

Thesis Committee: Professor Darrell J. Irvine and Professor Francesco Stellacci

ACKNOWLEDGEMENT

First of all, I would like to thank my advisor Angela M. Belcher for her unwavering support and constant encouragement not only in research but also in my life at MIT. She inspired, guided, and advised me with her intellectual senses and never spared praise for the results during the whole year. Whenever I needed help, she also shared her experiences as a researcher, as a daughter, and as a mom so that I could make better decision at all times.

I thank professor Gerbrand Ceder for his fundamental insight to interpret experimental results with scientific theory and professor Yang Shao-horn for her meticulous contemplation of analyzing results and answering to my trivial questions. I also thank professor Darrell J. Irvine and professor Francesco Stellacci for being my thesis committee with insightful feedback. I gratefully acknowledge Angelita Mireles at DMSE for her guidance to fulfill my academic courses, encouragement to finish my degree, and her counseling as a working mom. I also acknowledge Michelle Barron, Vesal Dini, and Jared Embelton for their help and support in the lab.

I thankfully acknowledge my collaborators, Dr. Junhyung Kim, Dr. Yun Jung Lee, Dr. Debadyuti Ghosh, and Dr. Dong Soo Yun for their fruitful results and discussions. I also appreciate my lab members: especially, my UROP, Tiffany Chen, for her help to finish my work during the last two years, Yun Jung for enriching my Ph.D. life, Dr. Yun for his unceasing encouragement, Andrew for all of his help, and Jifa, Rana, Mark, Jennifer, Yoon Sung, Heechul, Robbie, Hyunjung, John, Dahyun, Xiangnan, Forrest, David, and all the lab members for their friendship. I also thank to my Korean friends at MIT for sharing our experience to overcome difficulties.

I really appreciate my father in heaven and my mother in Korea for their undoubted love, sacrifice, and encourages during my whole life. I gratefully acknowledge my best friend, my husband Dr. Joungkeun Lim, for providing me with emotional support and allowing me enough time to finish my work by being a primary caretaker of our little one. Thanks to my son, Joonsuh, for everything and thanks to my brother and his family.

During the last six years at MIT, there are very important moments of my life and I really appreciate all of my friends for being with me with their empathy.

BIOGRAPHIC NOTE

EDUCATION

Massachusetts Institute of Technology, Cambridge, MA Present
Ph.D. Candidate in Material Sci. & Eng.
Research focus: surfactant-mediated biomineralization for 1-D nanostructure

Seoul National University 2004
M.S. in Interdisciplinary Program in Nano-science and Technology
Thesis title - Synthesis of monodisperse ferrite nanoparticles under Reflux condition

Seoul National University 2002
B.S. in Department of Chemical Engineering
Summa Cum Laude
Thesis title - Electroplating of copper with chemical additives as a kinetic enhancer

SCHOLARSHIP

Fellowship from MIT 2004-2005
Samsung Scholarship 2006-2009

PUBLICATION

Lee, J., Kim, J., **Lee, Y.**, Yoon, S., Oh, S. M., Hyeon, T.
Simple Synthesis of Uniform Mesoporous Carbons with Diverse Structures from Mesostructured Polymer/Silica Nanocomposites *Chem. Mater.*, 2004, **16**, 3323

Lee, Y., Lee, J., Bae, C. J., Park, J.-G., Noh, H.-J., Park, J.-H., Hyeon, T.
Large-Scale Synthesis of Uniform and Crystalline Magnetic Nanoparticles Using Reverse Micelles as Nanoreactors under Reflux Conditions *Adv. Funct. Mater.*, 2005, **15**, 503

Bae, C. J., Angappane, S., Park, J.-G., **Lee, Y.**, Lee, J., An, K., Hyeon, T.
Experimental studies of strong dipolar interparticle interaction in monodisperse Fe_3O_4 nanoparticles *Appl. Phys. Lett.*, 2007, **91**, 102502.

Lee, J.*, **Lee, Y.***, et al
Simple synthesis of functionalized superparamagnetic magnetite/silica core/shell nanoparticles and their application as magnetically-separable high-performance biocatalysts *Small* 2008, **4**, 143. ***equal contribution**

Lee, Y.J.*, **Lee, Y.***, Oh, D., Chen, T., Ceder, G., Belcher, A.M.,
Biologically Activated Noble Metal Alloys at the Nanoscale: for Lithium Ion Battery Anodes
Nano Lett., 2010 (accepted) ***equal contribution**

Lee, Y., Kim, J., Yun, D.S., Nam, Y.S., Qi, J., Gasteiger, H.A., Shao-horn, Y., Belcher, A.M.
A Genetic Template for Facile Synthesis of homogeneous Au-M (M: Ag, Pt, Pd) Alloy
Nanowires, 2010 (submitted)

Lee, Y*., Kim, J.*, Yun, D.S., Chen, T., Shao-horn, Y., Belcher, A.M.
Virus Templated Au/Pt core/shell Nanowires for Fuel Cell Reactions, 2010 (submitted)
***equal contribution**

Table of Contents

List of Figures

List of Tables

Chapter 1. Introduction

The main goal of this work is developing new method for synthesis of inorganic nanowires with the M13 phage template, the biological building block with filamentous structure. The incorporation of surfactant molecules into the M13 phage system can extend the application of M13 phage in diverse reaction condition, which was limited due to the stability of M13. Moreover, the cooperative interaction between the surfactant molecules and the inorganic nano-structures also improve the morphologies, yields, and stability and results in state-of-the-art properties in materials for medical diagnosis and fuel cell catalysts.

M13 phage has been utilized as templates for various one-dimensional nanowires because of the structural advantage, the high aspect ratio with dimensions of 880 nm in length 6 nm in diameter for wild type M13. The M13 phage consists of approximately 2700 major coat proteins (p8) helically wrapped around its single stranded DNA, and minor coat proteins (p3, p6, p7, and p9) at each end. The modification of subunit protein through the insertion of DNA fragments produces M13 phage with various peptide sequences selected at each protein. The M13 phage with specific peptide sequence against specific materials such as noble metal, carbon nanotubes, and semi-conductors has been successfully utilized as template for fabricating delicate inorganic hybrid structures. The ionic interaction between metal ions and E4 phage (M13 phage with four glutamate) as well as the specific interaction between inorganic materials and M13 with specific binding motifs provided nanowires of high quality and the cutting-edge properties.

Here, to extend the opportunity of M13 phage in bio-mineralization with delicately controlled structure, stepwise inclusion of surfactant molecules was proposed.

In chapter 2, as a first trial to check compatibility of surfactant molecules with M13 phage, magnetic nanoparticles coated with surfactant molecules, having positive charges, were hybridized into E4 phage. In a similar way of the synthesis of cobalt oxide and silver nanowires, which utilized the positive and negative charge interaction between E4 phage and cations, the negative charge on p8 major protein of E4 phage attracted magnetic nanoparticles of positive surface charges and resulted in E4 phage covered with magnetic nanoparticles. From the modification of p3 minor protein on E4 phage, specific peptide sequence targeting SPARC (Secreted Protein Acidic and Rich in Cystein) on prostate cancer cell lines was displayed, and M13 phage with dual functionality (targeting and imaging) was proposed. The minor protein was stable even after the addition of magnetic nanoparticles coated with surfactant molecules and showed enhanced selective from the targeting peptide sequence on p8 and intensified contrasting under MR imaging. The *in-vitro* and *in-vivo* experiments are currently the focus of my collaborator Dr. Debadyuti Ghosh.

After confirming the robust M13 structure in the presence of surfactant molecules, in chapter 3, surfactants were directly added during the bio-mineralization of Au nanowires from the specific Au-binding M13 phage, the p8#9. The incorporation of CTAB, an ionic alkylammonium surfactant, resulted in nanowires of well-defined structure by stabilizing the high-energy surfaces without losing the benefit from the specificity of p8#9. The well-defined surface of nanowires arising from the integration of surfactant molecules further allowed fine control of diameter sizes of Au nanowires, and the electrochemical properties of Au nanowires with various sizes were investigated for the oxidation of CO molecules for the application of Au nanowires as a co-catalyst in low

temperature fuel cell electrodes. The electrochemical analysis of Au nanowires was done by Dr. Junhyung Kim and professor Yang Shao-Horn.

The surfactant-mediated bio-mineralization of p8#9 was further extended to the synthesis of Au-based alloy nanowires (Au-Ag, Au-Pt, and Au-Pt-Pd) in chapter 4 and 5. In chapter 4, Au-Ag alloy nanowires with various compositions and different surface characteristics (free surface vs. stabilized surface with surfactant) were prepared and tested as Li-ion battery anodes. Despite the cost issue of Au and Ag for the practical applications, the systematic changes in potential profile during the lithiation process and the capacity retention with the surface structure and composition provided good model systems for exploiting electrochemical properties of nanomaterials with multi components. The chapter 4 was co-written by Dr. Yun Jung Lee and similar content is available at part of her thesis. She prepared Ag viral nanowires and measured the electrochemical properties of all samples. Theoretical explanations and thermodynamic mechanisms in collaboration with professor Gerbrand Ceder.

In chapter 5, the incorporation of Pt, the most active catalyst metal in various field, resulted in Au-Pt alloy nanowires with various compositions and morphologies. The application of Au-Pt alloy nanowires as electro-catalysts verified synergistic effect: the activity of Au-Pt alloy nanowires approaching that of Pt despite high contents of Au. The promotional effect of catalyst from the combination of two active materials was also verified in chapter 6, from the Au/Pt core/shell nanowires prepared by adding Pt nano-shell on Au core nanowires described in chapter 3. The dendritic Pt shell was grown only on the surface of Au nanowires selectively and the thickness (coverage of Pt shell) was deftly controlled. The Au/Pt core/shell nanowires with various shell thicknesses, in other

words, various Au:Pt compositions were tested for electro-catalysts both in anodes and cathodes requiring different criteria (Pt with co-catalyst preventing Pt poisoning for anode and high loading of Pt for cathode) in low temperature fuel cell. The electrochemical measurement of Au-Pt alloy nanowires and the Au/Pt core/shell nanowires were done by Dr. Junhyung Kim and professor Yang Shao-Horn.

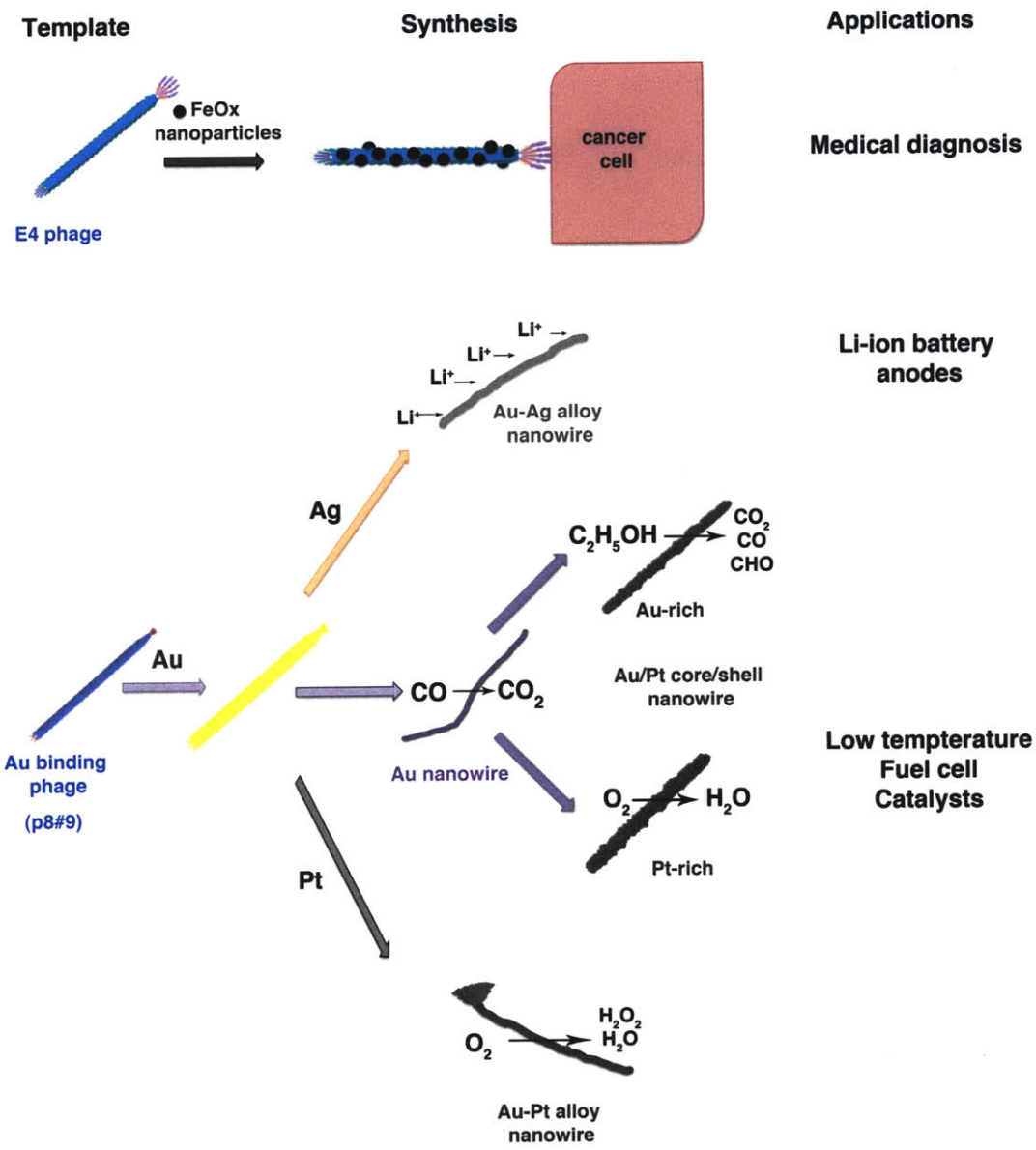

Figure 1.1 Graphic of Contents. The simplified graphic summarizes the contents of this thesis. In chapter 2, positively charged magnetic nanoparticles were introduced to E4 phage with specific cancer targeting peptides to prepare magnetic phage to enhance contrast at tumor sites in the MR imaging. The Au-binding phage, p8#9 was utilized as a specific template for various Au-based nanowires. Firstly in chapter 3, Au nanowires with various diameter sizes were prepared, and the Au nanowires served as core materials for the preparation of Au/Pt core/shell nanowires in chapter 6. The addition of Ag and Pt ions during the Au nanowire synthesis provided Au-Ag (chapter 4) and Au-Pt (chapter 5) alloy nanowires with controlled compositions.

Chapter 2. Magnetic phage as contrast enhancer in MR imaging

2-1. Introduction

Nano-technology has been one of the critical issues in science and engineering for the last few decades. Nano-materials are defined as materials with scale of 10^{-9} m dimension, and show different physical and chemical properties from the same materials in bulk state[1]. This different property, even in the same materials, can be explained as a result of the vast increase in surface ratio upon the total volume. Because the nano-materials are composed of hundreds or thousands of atoms or molecules assembled together, its study can also bridge the atoms or molecules and the bulk materials that have many important properties. The interesting feature of nano-materials is not only the difference of property from its bulk state but the fact that the properties are also varied in their size in the nano-meter scale. Magnetic nano-materials have different magnetic coercivity and hysteresis as the particle size differs, and optical nano-materials absorb different wavelengths of light, thus emitting different color[2]. Cadmium Selenide nanoparticles, one of the well-studied semi-conducting quantum dots, are a good example because they emit rainbow color, the full visible light color, when the particle sizes were tuned from 1.5 nm to 8 nm[3].

During the last few decades, much research was done to make new nano-materials with various dimensions: nanoparticles, nanorods, and nanowires. Moreover, in some fields, the real application of nano-materials into a device was successfully done and the products are now commercially available. By reducing the device dimension to nano-scale, computer chip size became compact even as the capacity increased, and we can use much thinner and lighter electronic devices such as a laptop, an mp3 player, and a

memory card. By utilizing a new or an improved property in nano-materials, advances in our daily life supplies such as cosmetics, house appliances, and clothing became feasible.

One of the milestones for the real application of nano-materials exists in diagnostic and therapeutic medical treatment[4]. Of course, from the development of nanotechnology, people tried to use the nano-materials to solve intractable issues of life science, and cancer was one of them[5]. Nanoparticles seem to be a good candidate for cancer research because they have higher surface area that can be utilized for attaching therapeutic or diagnostic functional groups[6]. The size (10 nm to 100 nm) is in the range of proper interaction with the receptors located on the cell surfaces. Moreover, the tumor cells usually show reduced efficiency for lymphatic drain, which results in accumulation of nanoparticles inside. With these characteristics, much research was done with the nanoparticles useful for detection of cancer cells with higher efficiency and accuracy and for potentially therapeutic purposes[7].

Despite the huge number of results reported previously, the application of nano-materials into a real medical case is just being realized, and most of the research done for cancer with nano-materials is the detection of tumor site with nanoparticles *in vitro* of human cells or *in vivo* with mice[8,9]. The challenge in cancer research is the early and incisive detection from a non-invasive method because cancer cells are easily activated when they are exposed into the air or physically stimulated. Magnetic resonance imaging (MRI) is one of the non-invasive in vivo conditions for cancer diagnosis. Metal ferrite (MFe_2O_4, M could be Mn, Co, Fe or Ni) nanoparticles, loaded with enzyme targeting the cancer cell surface ligands, were tested as a contrast enhancer in dark imaging MR detection, and gadolinium oxide and manganese oxide are for bright imaging[10,11,12]. Even

if there was a size effect in the same materials, among the ferrite nanoparticles, manganese ferrite intensified the contrast significantly[13]. Nevertheless, for the safety testing issue to the human body, iron-based ferrites are the only acceptable contrast enhancer so far.

Initially, magnetic nanoparticles received attention due to its magnetism utilized as magnetic storage media[14]: they maintained the magnetic moment after the magnetic field removed. However, magnetic nanoparticles smaller than about 20 nm lose their magnetism under the absence of magnetic field at room temperature because their magnetism decreased as the particle size decreased, and the thermal fluctuation energy overcome the magnetic moment of the individual magnetic nanoparticle[14]. The change of magnetism is confirmed theoretically and experimentally and called superparamagnetism. This paramagnetism of iron oxide nanoparticles at room temperature will be adopted in MRI detection.

There are lots of reports about the synthesis of iron-based magnetic nanoparticles: thermal decomposition of $Fe(CO)_5$ complex in an organic solvent, co-precipitation of ferric and ferrous ions in water, reverse micelles(modified co-precipitation of iron salt in water nanodrop), sonochemical decomposition of iron ions[15,16,17,18]. They all have advantages and disadvantages when we evaluate them from a different point such as cost, yield, scalability, safety, and reproducibility. Magnetic nanoparticles from the thermal decomposition method of iron pentacarbonyl are of importance due to its monodispersity and crystallinity. The co-precipitation method is the cost-effective and safe one because they used iron salts even the nanoparticles show broader size distribution than those from iron pentacarbonyl. The well-known LSS (Liquid Solid Solution) strategy is the middle

of two methods mentioned above[15]. In LSS strategy, cost-effective metal salts were used to prepare a metal-surfactant complex, the precursor of nanoparticle synthesis in the thermal decomposition method, and the precursor and solvent were refluxed at high temperature to get nanoparticles with narrow size distribution comparable to those prepared from iron pentacarbonyl.

2-2. Synthesis of magnetic nanoparticles

The synthesis of magnetic nanoparticle can be explained in two steps: preparation of precursors and high temperature decomposition of the metal oleate complex. Figure 2.1 described the synthesis of nanoparticles from the precursor preparation to surface modifications. As we explained in the previous section, hazadrous chemicals should not be used during the synthesis and the application steps for our purpose here. Hydrated metal precursors were dissolved in de-ionized water, and surfactants (sodium oleate) were dissolved in hexane. The two mediums of water and hexane were not miscible under these conditions due to their difference in polarity. However, the addition of ethanol, miscible both in water and hexane, made the solution homogeneous with a vigorous stirring at elevated temperature around 60 °C. In the solution, the metal ions dissolved in water collided with surfactant molecules existing originally in the hexane layer and then produced a metal-oleate complex. After about three hours at elevated temperature, the interaction between metal ions and the surfactant molecules became stable. The mixture then was cooled down to room temperature without any extra cooling force. The transfer of metal ions from water to hexane was visible because of their difference in gravity; initially metal ions were dissolved in the bottom layer and finally they went to the upper layer. The first row of Fig. 2.1 illustrates the transfer of the ferric ion during the precursor preparation. After the formation of Fe-oleate complex, excess hexane and ethanol were removed by evaporation and viscous red-black precursors remained.

The precursors were re-dispersed in solvents (boiling temperature increases as the number of carbon of solvents increases) which have a high boiling temperature and then

mixed with additional surfactants. The solution was heated to temperature from 270°C to 350 °C according to the desired particle size. Usually the reaction mixture was heated to optimum temperature within 30 minutes to get nanoparticles with narrow size distribution. After the final reaction at high temperature, the solution was cooled down to room temperature in an ambient condition. Nanoparticles were collected from the excessive organic surfactants and the solvent medium by centrifugation. Because we have a non-polar layer of surfactant on the surface of nanoparticles, the addition of polar solvent precipitates the nanoparticles due to their density and leaves other chemicals in the supernatant solution. After cleaning, synthesized magnetic nanoparticles were stably stored in hexane more than a year. The synthetic method here is adapted from the synthesis of maghemite nanoparticles, but due to the similar properties of maghemite (γ-Fe_2O_3) and magnetite (Fe_3O_4), confirmation of magnetic nanoparticle is challenging. Moreover, the synthetic magnetic nanoparticles in nanometer sizes show mixed composition of both maghemite and magnetite[17,20]. Therefore we will used the notation of magnetic nanoparticles as FeO_x.

Nano-materials exhibit different properties from their bulk materials, and the properties of nano-materials are influenced by their size and dimension. Therefore, for example, if we measure several properties of 4 nm and 12 nm magnetic nanoparticles, respectively, they will show different magnetic hysteresis, coercivity, and susceptibiliy, even if they are the same magnetic nanoparticles with the same lattice parameter and composition. Magnetic nanoparticles in this research are utilized for MRI application, so their magnetic relaxation under the magnetic field is the key value for our experiment. If the nanoparticles have diverse size distribution in one sample, we cannot get relaxation

time with high signal to noise ratio because nanoparticles with different sizes give diffferent values. Thus, the magnetic nanoparticles should have narrow size distribution to give consistent response signal and to minimize noise under the magnetic field. Particle size was confirmed with transmissional electron microscopy (TEM) analysis. Figure 2.2 (a) represents the TEM image of 12 nm magnetic nanoparticles taken at lower magnification and higher magnification (inset), and Fig. 2.2 (b) is the TEM image of 4 nm magnetic nanoparticles. 4 nm sized nanoparticles were stacked like atoms in a lattice structure due to their conformal size. The images showed narrow size distribution of nanoparticles so that the nanoparticles can be utilized for our research, which requires consistent magnetic property. We confirmed the crystallinity of nanoparticles from high magnification TEM and from the X-ray Diffraction (XRD).

Methods

Preparation of Fe(oleate)$_3$ precursors: 5.4 gram of $FeCl_3 \cdot 6H_2O$ was dissolved in 30 mL of de-ionized water completely. In a round bottom flask, 18.25 gram of sodium oleate with 70 mL of hexane were mixed gently with magnetic stirring at mild temperature around 30 °C. The addition of brownish clear solution of Fe to the homogeneous solution of sodium oleate witth hexane resulted in two phases in the flask. The solution was heated to 70 °C for three hours after the addition of 40 mL of ethanol to make one phase solution. When the final solution was cooled down to room temperature, viscous brown precursor floated on top of clear solution. The final solution was washed with de-ionzed water to remove any residual salts and then dried to remove hexane.

Synthesis of magnetic nanoparticles: 1.5 mL of viscous Fe(oleate)$_3$ was carefully transferred to round bottom flask with 0.5 mL of oleic acid 7 mL of 1-octadecene. The 1-octadecene could be substituted by other hydrocarbene solvent with more carbon numbers. The solution was heated to 300 °C in 15 minutes, boiled for another 30 minutes, and was cooled down to room temperature by removing the heat source. The very oily resultant solution with black color contains excess organic surfactant and solvents, so nanoparticles were collected after consecutive washing with acetone and ethanol followed by centrifugation.

2-3. Surface modification of magnetic nanoparticles for water-stability

Because the magnetic nanoparticles are stable only in organic solvents such as hexane, they are not directly applicable to most of biological systems. Several leading groups already reported bare magnetic nanoparticles with good crystallinity and magnetic property in aqueous system[20], but they were not applicable to our system. Because magnetic nanoparticles without any surfactant on their surface inherently have magnetic affinity between themselves, they cannot keep optimum distance from each other and thus cannot interact with the biological template (the M-13 phage in this research). So we chose the magnetic nanoparticle system with biologically friendly chemical surfactants on its out side and treated the surface to be incorporated into the condition for living cells and phages with various pH and buffer strengths.

Magnetic nanoparticles were chemically modified to be stable in water by functionalizing the surface with the amine or carboxyl group. We adopted the well-known approach with the lipid layer chemistry but modified it for our purpose; we used surfactant molecules, which have smaller molecular weight and shorter hydrocarbon chain length than the typical lipids. According to research papers about water stable nanoparticle treated with lipid molecules after the synthesis, it was not easy to make a stable water solution as they were in organic solvents[21-23]. It is assumed that in the water solution, nanoparticles were located in a distance because their hydrodynamic radius was increased due to the incorporation of water molecules between lipids. For example, people reported that the Cross Linked Iron Oxide (CLIO: one of the most widely used magnetic nanoparticle for biological application) sample with 4 nm core magnetic diameter showed hydrodynamic diameter bigger than 40 nm[24]. As a result, the TEM

images of water-stable nanoparticle prepared typical methods showed sparsely located nanoparticles over the whole grid area, and the solution of nanoparticles just retained very diliute concentration compared to when they were in organic solvents[22,25]. The increased volume of magnetic nanoparticles in the water system was not a problem for the signalling itself, but it limited the transfer or movement of nanoparticles under magnetic field, which is essential for in vivo experiments and real application.

By using surfactant molecules with a shorter carbon chain, we achieved two advantages over the typical methods: reduced the hydrodynamic radius, similar to that of in an organic solvent and increased concentration comparable to that in an organic solvent. Figure 2.3 (a) shows magnetic nanoparticles, from a water solution after the surface modification, closely packed together in a monolayer even though it's not perfect coverage. Nanoparticles can be located right next to the others because their diameter is not greatly increased. This implies that nanoparticles from the surfactant modification system have a smaller hydrodynamic radius than the typical water-soluble nanoparticles treated by lipid molecules. This hypothesis was proved by light scattering data. Nanoparticles showed slightly positive and slightly negative charges on their surface according to the functionality of surface modification and that the value of hydrodynamic radius of nanoparticles in water was slightly bigger than the radius observed in TEM analysis: the average hydrodynamic radius value obtained by light scattering was 25% larger than the value observed from TEM image of nanoparticles in hexane solvent for 12 nm nanoparticle case.

Methods

Modification of surface of magnetic nanoparticles: in a 20 mL glass vial, 1 mL of FeOx nanoparticles dispersed in hexane with concentration about 6.2 mg/mL was transferred. The magnetic nanoparticles were slowly stirred with magnetic stirring bar at mild temperature around 30 °C. In a 15 mL falcone tube, 13 mL of DI water and 1 mL of 3% wt HCl solution were mixed. 0.5 mL of oleylamine was transferred to 14 mL of very diluted HCl solution and slightly vortexed. The oleylamine solution was then added to the FeOx solution with mild heating and stirring. 0.5 mL of ehtanol was added to the nanoparticle solution and the solution was heated to about 80 °C with vigorous stirring. After two hours reaction, the solution turned to be homogeneous. The solution was collected by centrifugation and transferred to de-ionized water after washing.

2-4. Stability test of water-soluble magnetic nanoparticles

Another advantage of the reduced hydrodynamic diameter of nanoparticles is that the nanoparticle solution can stably retain higher concentration of nanoparticles comparable to the concentration in organic solvent. The picture image of two solutions in Fig. 2.3(b) was taken from magnetic solution kept in ambient static condition for 30 days after the preparation. Any aggregation or precipitation was visible for all 30 days, and TEM image taken from the solution sample after 30 days was the same with the image taken right after the synthesis. It was still impossible to increase the concentration of the water-stable solution to the level of organic nanoparticle solution with stability for over 30 days, but the concentration of water-stable nanoparticles was increased up to 70 mM Fe concentration. The stability of nanoparticle solution was tested in various conditions: temperature, pH, and buffer strength.

In terms of the temperature, solutions were stable at room temperature and human body temperature in the static condition but started to show phase separation in 4 °C after 15 days when the nanoparticles were dispersed in de-ionized water. The surfactants which were used for stabilizing nanoparticles during the chemical synthesis and surface modification began to solidify due to their melting temperature and floated near the top of the solution.

By adding hydrochloric acid and acetic acid, we also controlled the solution pH from 7 to 1 and tested the stability of nanoparticles with amine coated sample at static condition. The solutions showed no aggregation or phase separation, but in the solution with pH lower than 3, changes of solution color was observed. Generally magnetic nanoparticles are susceptible to acidic condition. Solutions were also tested in various pH

from 7 to 13 with sodium hydroxide solution. Nanoparticles were stable up to pH 10 both in solution and TEM images, however, at pH higher than 11, nanoparticles were separated from the whole solution after mixing and made two phases: one is the top oily solution of nanoparticles and the other is slightly turbid aqueous solution at the bottom. Figure 2.4, the TEM image of nanoparticles aggregated in pH 11 solution after one day, shows aggregated microstructure with organic layer covering the nanoparticles. The nanoparticles were stable despite the aggregation at pH 11 (Fig. 2.4(b)). We found that the aggregation from the high pH solution was reversible. Acid solution was added to the phase separated magnetic nanoparticle solution at pH 11, and after short agitation, the solution was kept at room temperature for about 5 days. Then the solution showed homogeneous color without any phase separation, and from the TEM image taken after 5 days of acid addition, we confirmed the reversibility of aggregation of magnetic nanoparticles in different pH solution.

2-5. Multi-functional magnetic phage with specific binding to cancer cell

The N-terminus of p8 can be genetically engineered to display peptides along the virus. Previously, a tetraglutamate motif (E4) was displayed on the p8 surface and their carboxylic acid side chain groups resulted in the slightly negative charge of the modified E4 virus in buffer conditions. The M-13 phage with tetra-glutamate on the major protein named E4, was utilized as a wire template for bio-inorganic materials due to its stable structure and high affinity for several metal cations[27,28]. Here, we expanded this affinity concept from ions to nanoparticles.

We succesfully prepared water stable magnetic nanoparticles with carbonyl group and amine group in physiological buffer condition (pH ~7). Amine-functionalized nanoparticles were used for attachment due to potential electrostatic interactions with the negatively charged E4 phage. Initially, magnetic nanoparticles resupsended in water were mixed with E4 phage in TBS at various concentrations. The final TBS concentration ranged from 20 to 75% of the original concentration. Any significant aggregation of nanoparticles or phase separation after the mixing was not observed for a week, but the solution color was darker on the bottom. One drop of solution mixture was taken for TEM analysis. Figure 2.5, the low magnification TEM image, demonstrates the uneven distribution of black color (the magnetic nanoparticles) over the whole range and implies nanoparticles have the tendency to locate along the E4 phage, despite the phage entanglement. The magnetic phage, E4 phage decorated with magnetic nanoparticles, was successfully prepared by incubating E4 phage in buffer solution with magnetic nanoparticles dispersed in de-ionized water as shown in Fig. 2.6 (b).

2-6. Response of magnetic nanoparticles and magnetic phage under external magnetic fields

The application of magnetic phage as a selective targeting agent on prostate cancer cell line is simply sketched in Fig. 2.6(c). To explore appropriate enhancement of contrast in MRI (Magnetic Resonance Imaging), the magnetic repsonse of the water-stable magnetic nanoparticles was measured by using magnetic spectrophotometry. Maghemite nanoparticles were detectable under the dark imaging mode of MRI, so R2 value, which defines the relation between the transversal spin-spin relaxation time (T2) with various Fe concentration (mM), was obtained. The R2 value of magnetic nanoparticles is also a size-dependent property, so we have different R2 values upon the nanoparticle sizes. As the nanoparticle size increases, the R2 value showed a higher value from 15 % up to 100 % than the typically used CLIO (Cross Linked Iron Oxide) samples[29]. The R2 value of typical CLIO sample is about 30 to 40 $[mMs]^{-1}$.

In addition to the examining the magnetic response of the nanoparticles, we looked at the magnetic reponse of magnetic phage. The R2 values of magnetic phage changed as the magnetic nanoparticle size changed, but generally the R2 value of the magnetic phage was about 10 % to 20 % lower than that of the free nanoparticles. As shown in Fig. 2.7, the R2 value of 12 nm magnetic nanoparticle solution was about 65.1 $[mMs]^{-1}$ but the value of magnetic phage loaded with 12 nm nanoparticles was about 58.7 $[mMs]^{-1}$. This result suggests that monodisperse nanoparticles can be loaded onto phage and exhibit a magnetic response under a magnetic field, therefore, the magnetic phage could be utilzed as targeting agent to enhance MR contrast at selective region of prostate cancer cell lines by adding a targeting peptide sequence on p3.

2-7. Preparation of magnetic phage with targeting peptides

As previously mentioned, M-13 has proved a useful tool for peptide display. Previous work has shown phage display can be used to identify peptides and single chain antibodies as cell targeting ligands *in vitro* and *in vivo*[30]. Since the DNA that encodes for the virus is encapsidated by virus, there is a physical linkage between the peptide displayed on the surface and its DNA sequence. This enables screening of random library of peptides displayed on phage to screen potential peptides against target molecules and easy identification via DNA sequencing. We can combine our approach to identify peptide binders against inorganic mateials with selection of peptide binders against biomolecule targets, such as cell surface receptors overexpressed on tumors. Kelly *et al* used *in vivo* phage display to select a peptide with specificity towards the the secreted protein, acidic and rich in cysteine (SPARC) receptor.[31] This protein is involved in a signaling loop with vascular endothelial growth factor (VEGF)[30]. Upon ligand-receptor binding, this activates production of VEGF, which in turns bind to VEGF receptor and activates further SPARC expression. This molecular pathway is overexpressed in prostate cancer and SPARC has been shown to be a biomarker indicative of the stage of prostate cancer and the potential for metastasis.

We modified the p3 proteins with selective targeting peptide sequence and added magnetic nanoparticles to prepare bi-functional M13 phage toolkit for both targeting and imaging of special cell lines. The result shown in Fig. 2.8 confirms the intact structure of targeting sequence after the addition of magnetic nanoparticles on p8 to prepare magnetic phage. When the concentration of magnetic phage with targeting sequence decreased, the absorbance also decreased systematically. Therefore, the targeting peptides are

considered to be as active after the formation of magnetic phages in solution. As shown in the control set of phage, without targeting sequence on p3, any correlation between the phage concentration and the absorbance was observed.

After confirming the stability of targeting peptides in magnetic phage, the SPARC-targeted magnetic phage solutions of vairous concentrations (10^9 and 10^{10} pfu) were tested on two cell lines. One is a prostate cancer cell line with highly expressed SPARC (C42B) and the other is a low-expressing negative control prostate cancer cell line (DU145). The cells were incubated with magnetic phage with SPARC-targeting peptides and then harvested and lysed (*in vitro*). The lysates were measured for the transversal relaxation time (T2) as shown in Fig. 2.9. The reduced value of T2 (shorter relaxation time) at C42B cell lines clearly proved better uptaking of magnetic phage on SPARC-positive cell lines, implying enhanced contrast under MR field.

2-8. Conclusion

Mono-disperse magnetic nanoparticles were prepared from cost-effective and less-toxic $Fe(oleate)_3$ precursors. With the surface modification of as prepared magnetic nanoparticles, which were only dispersed in organic solvents, water-stable magnetic nanoparticles with reduced hydrodynamic radius were successfully prepared. The magnetic nanoparticles were then fused with M13 phage with additional four glutamate functionality on major protein coat on p8. The resultant magnetic phage, E4 phage with magnetic nanoparticles on p8, showed relaxivity comparable to that of CLIO nanoparticles widely used as contrast enhancer in biological labs. The modification of p3 on E4 phage followed by the addition of magnetic nanoparticles to build bi-functional magnetic phage witih targeting peptide sequence on SPARC exhibited excellent selectivity over SPARC positive prostate cell lines *in vitro*.

2-9. References

1 Klabunde, K. J. *Nanoscale Materials in Chemistry*. (Wiley-Interscience, 2001).

2 Sun, S. & Zeng, H. Size-Controlled Synthesis of Magnetite Nanoparticles. *J. Am. Chem. Soc.* **124**, 8204-8205 (2002).

3 Murray, C. B., Kagan, C. R. & Bawendi, M. G. Synthesis and characterization of monodisperse nanocrystals and close-packed nanocrystal assemblies. *Annu. Rev. Mater. Sci.* **30**, 545-610 (2000).

4 C. M. Niemeyer, C. A. M. *Nanobiotechnology: Concepts, Applications and Perspectives*. (Wiley-VCH, 2004).

5 Ferrari, M. Cancer nanotechnology: Opportunities and challenges. *Nat. Rev. Cancer* **5**, 161-171 (2005).

6 Levy, L., Sahoo, Y., Kim, K.-S., Bergey, E. J. & Prasad, P. N. Nanochemistry: Synthesis and Characterization of Multifunctional Nanoclinics for Biological Applications. *Chem. Mater.* **14**, 3715-3721 (2002).

7 Liotta, L. A., Ferrari, M. & Petricoin, E. Written in blood. *Nature* **425**, 905-905 (2003).

8 Oyewumi, M. O., Yokel, R. A., Jay, M., Coakley, T. & Mumper, R. J. Comparison of cell uptake, biodistribution and tumor retention of folate-coated and PEG-coated gadolinium nanoparticles in tumor-bearing mice. *J. Controlled Release* **95**, 613-626 (2004).

9 Newton, J. R., Kelly, K. A., Mahmood, U., Weissleder, R. & Deutscher, S. L. In vivo selection of phage for the optical Imaging of PC-3 human prostate carcinoma in mice. *Neoplasia* **8**, 772-780 (2006).

10 Yan, F. *et al.* Synthesis and characterization of silica-embedded iron oxide nanoparticles for magnetic resonance imaging. *J. Nanosci. Nanotechnol.* **4**, 72-76 (2004).

11 Zhang, Y., Sun, C., Kohler, N. & Zhang, M. Q. Self-assembled coatings on individual monodisperse magnetite nanoparticles for efficient intracellular uptake. *Biomed. Microdevices* **6**, 33-40 (2004).

12 Harisinghani, M. G. *et al.* Noninvasive detection of clinically occult lymph-node metastases in prostate cancer. *New England Journal of Medicine* **348**, 2491-U2495 (2003).

13 Lee, J. H. *et al.* Artificially engineered magnetic nanoparticles for ultra-sensitive molecular imaging. *Nat. Med.* **13**, 95-99 (2007).

14 O'handley, R. C. *Modern Magnetic Materials: Principles and Applications* (Wiley-Interscience, 2000).

15 Hyeon, T., Lee, S. S., Park, J., Chung, Y. & Na, H. B. Synthesis of Highly Crystalline and Monodisperse Maghemite Nanocrystallites without a Size-Selection Process. *J. Am. Chem. Soc.* **123**, 12798-12801 (2001).

16 Kang, Y. S., Risbud, S., Rabolt, J. F. & Stroeve, P. Synthesis and Characterization of Nanometer-Size Fe3O4 and Y-Fe2O3 Particles. *Chem. Mater.* **8**, 2209-2211 (1996).

17 Lee, Y. J. *et al.* Large-scale synthesis of uniform and crystalline magnetite nanoparticles using reverse micelles as nanoreactors under reflux conditions (vol 15, pg 503, 2005). *Adv. Funct. Mater.* **15**, 503-509 (2005).

[18] Shafi, K. *et al.* Sonochemical synthesis of functionalized amorphous iron oxide nanoparticles. *Langmuir* **17**, 5093-5097 (2001).

[19] Wang, X., Zhuang, J., Peng, Q. & Li, Y. D. A general strategy for nanocrystal synthesis. *Nature* **437**, 121-124 (2005).

[20] Park, J. *et al.* One-Nanometer-Scale Size-Controlled Synthesis of Monodisperse Magnetic Iron Oxide Nanoparticles13. *Angew. Chem. Int. Ed.* **44**, 2872-2877 (2005).

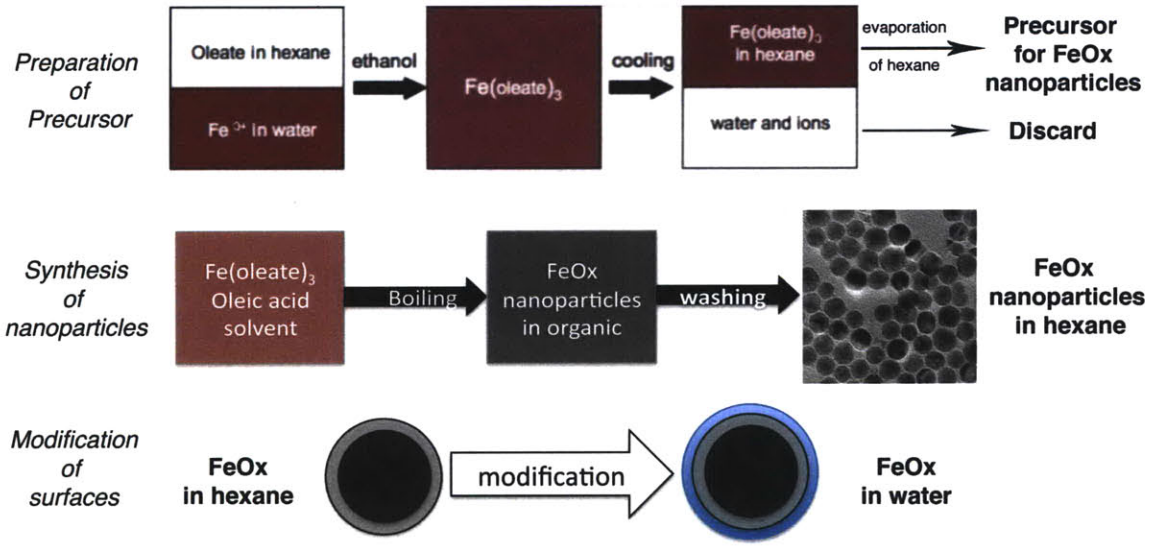

Figure 2.1 Schematic diagram for the preparation of water soluble FeO_x nanoparticles. The precursor was prepared by the LSS method described above. After the formation of precursor, hexane was evaporated and viscous $Fe(oleate)_3$ was transferred to a round bottom flask. Additional surfactant, oleic acic and solvent were mixed with viscous precursors and the resultant mixture was heated to temperature above 270 °C very quickly. The solution was then boiled for thirty mintues and cooled down to the room temperature. The nanoparticles were washed and purified by the addition of the polar solvent (mixture of acetone and ethanol with 1:1 vol. ratio) followed by centrifugations. As-prepared nanoparticles are stable in organic solvents such as hexane. Surface modification with oleylamine or PEG successfully transferred the FeO_x nanoparticles into water.

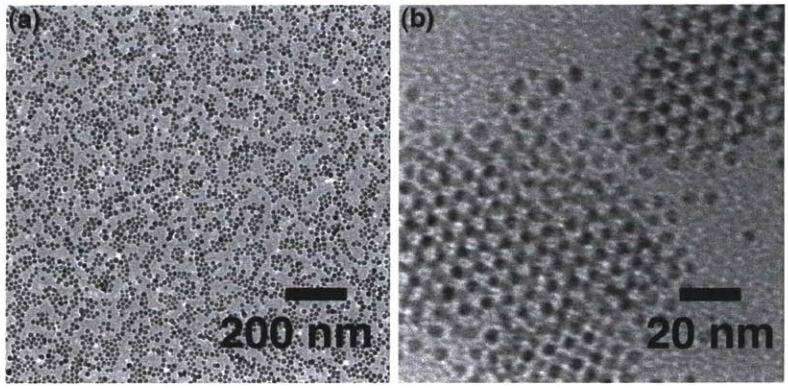

Figure 2.2 TEM images of magnetic nanoparticles (FeO_x) dispersed in hexane after purification. (a): 12 nm and (b): 4 nm.

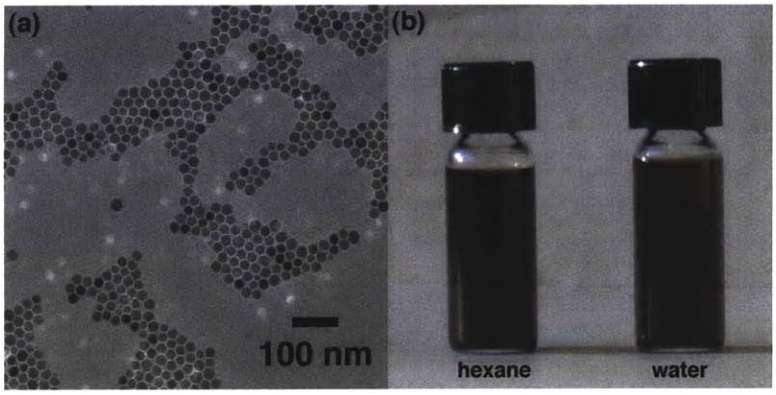

Figure 2.3 Water-stable magnetic nanoparticles after surface modification. (a) TEM image of magnetic nanoparticles dispersed in water solution after the surface modification, (b) Picture of solution of magnetic nanoparticles dispersed in hexane (left) and de-ionized water (right) in 30 days after the preparation at room temperature.

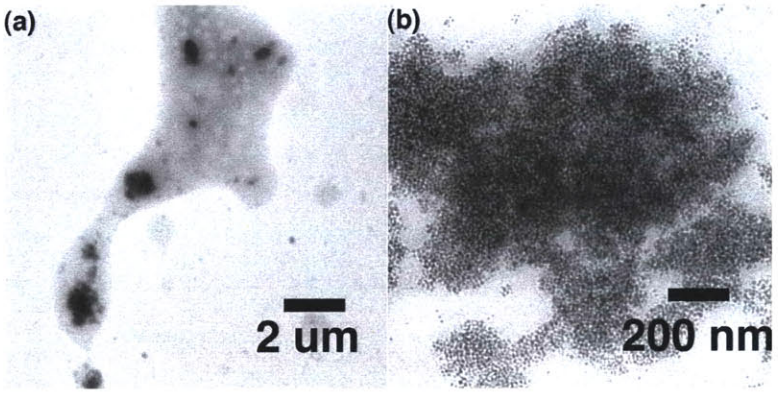

Figure 2.4 TEM images of amine-treated magnetic nanoparticles at pH=11. (a) The low-resolution TEM image shows aggregated nanoparticles with organic layer covering the them. (b) The individual nanoparticles were stable in solution of high pH.

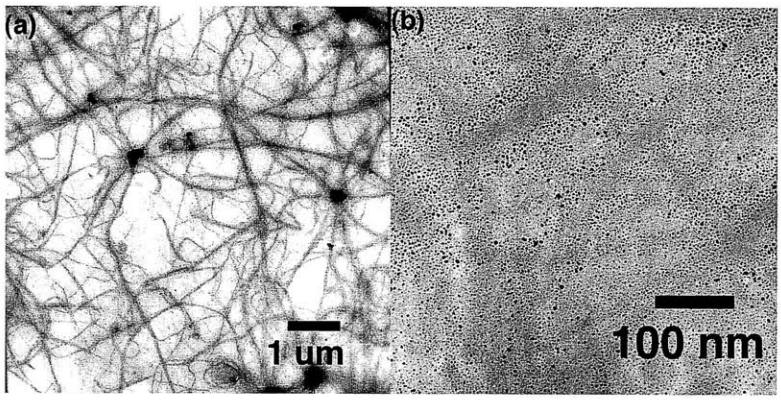

Figure 2.5 Low-magnification TEM images from the mixture of water-soluble magnetic nanoparticles with E4 phage. (a) The dark filamentous line appeared aggregated E4 phage with magnetic nanoparticles functionalized with amine. (b) When the image was magnified, magnetic nanoparticles were dispersed selective area TEM grid, implying interaction between E4 phage and magnetic nanoparticles.

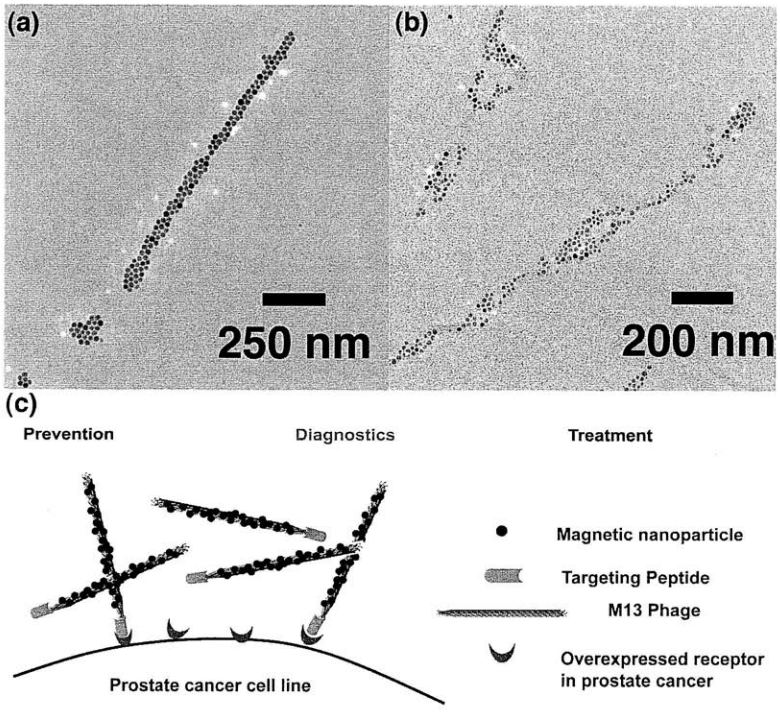

Figure 2.6 TEM images of magnetic phage and the simplified mechanism for targeting prostate cancer from magnetic phage with specific peptides. (a) Magnetic phage structure in de-ionized water: E4 phage with amine functioned magnetic nanoparticles from electrostatic interaction (b) When the magnetic phage was prepared in the buffer solution, the density of nanoparticles was decreased. (c) M13 phage as a multifunctional genetic scaffold with specific cancer targeting and contrast enhancement in MR imaging.

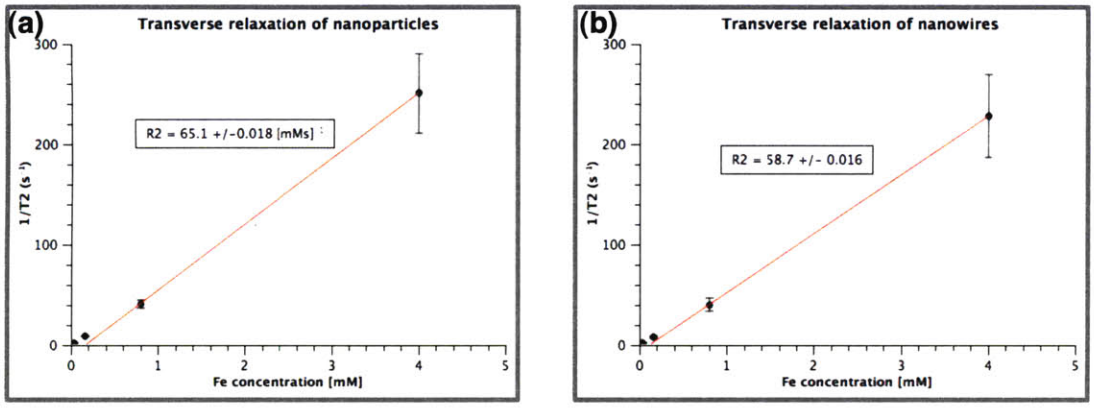

Contrast agent	Relaxivity (R2) $[mMs]^{-1}$
CLIO	~30-40
γ-Fe_2O_3 nanoparticle (12 nm)	65.1
magnetic phage	58.7

Figure 2.7 Magnetic responses of magnetic nanoparticles and magnetic phages. (a) Relaxation of magnetic nanoparticles and (b) magnetic phages confirmed enhancement of magnetic phage as contrasting agent in MRI than the typical CLIO materials.

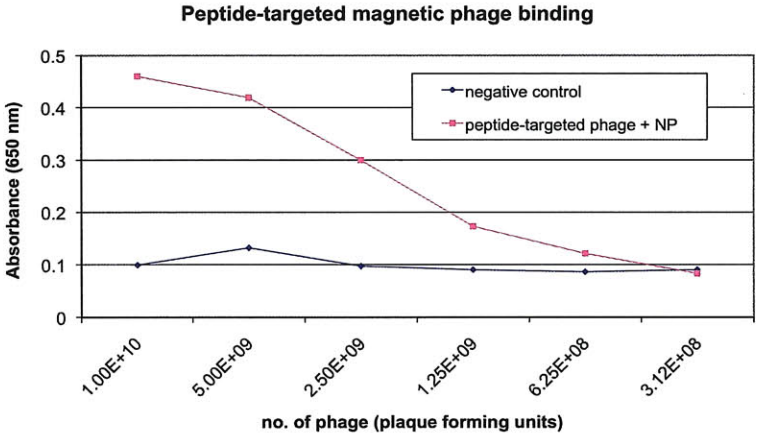

Figure 2.8 Confirmation of targeting ability of peptides on magnetic phage. M13 phage with targeting peptide sequence at pIII was decorated with magnetic nanoparticles and tested against target molecules. The quantitative analysis was done by ELISA (Enzyme-linked immunosorbent assay). The systematic decrease in absorbance when lowering the phage concentration suggests that the nanoparticle attachment on M13 phage does not interfere the ability of pIII to target molecules.

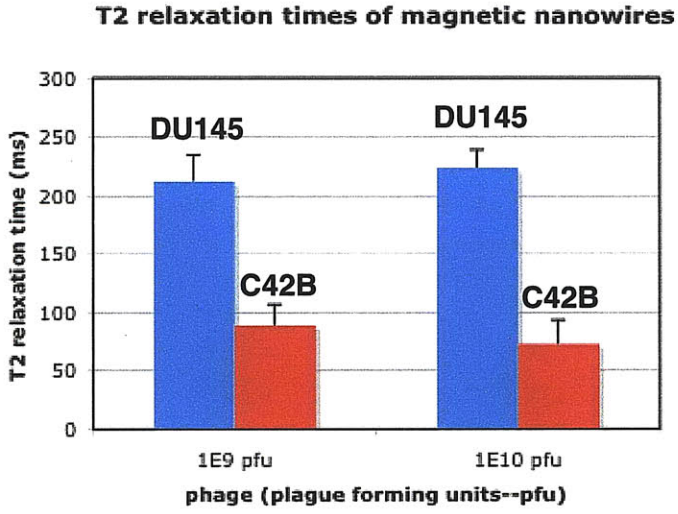

Figure 2.9 Specificity test of magnetic phage with SPARC targeting peptides at various phage concentrations. Prostate cell lines with different SPARC expression were incubated with magnetic phage with SPARC targeting peptides. DU 145 (negative control with lower SPARC expression, shown as blue bar) and C42B (highly expressed SPARC, shown as red bar) clearly exhibited differences in T2 relaxation time, implying higher uptake of magnetic phage in C42B cell lines (the SPARC-positive cell lines).

Chapter 3. Synthesis of Au nanowires from p8#9 template

3-1. Introduction

Reports of low temperature catalytic activity of nanometer-sized Au reinforce the utility of Au as a highly stable, highly active noble metal[1,2]. The catalytic activity of Au nanoparticles is greatly dependent on their sizes, surface structures, substrates, and impurities, and as a result much attention has been given to designing new catalysts based on high quality Au nanoparticles[3,4,5,6,7]. For instance, Au nanoparticles are being used as catalysts in fields as diverse as seed materials for nanowire growth, electro-catalysts for fuel cells, hydrogenation and oxidation of organic compounds, and constituents of pollution control materials[8,9,10,11,12]. There has been notable progress made recently in synthetic methods and characterizations for Au nanoparticles and Au nanorods[13,14]. The latter can be prepared by the seed-mediated synthesis, a modification of the conventional synthesis of colloidal Au nanoparticles, yielding Au nanorods with anisotropic dimensions and high aspect ratio[15,16,17]. Although less progress has been made in developing high yield Au nanowire synthesis methods in aqueous phase, several groups have prepared Au nanowires of micrometer length in organic solvents resulting in higher yields, excellent transport properties, and at relatively low reaction temperatures[18,19,20].

A significant challenge in this research is the development of synthetic methods capable of producing uniform monometallic and alloy nanowires in useful quantities with controlled size and composition for applications in electrocatalysis. In particular, applications of Au nanoparticles have been limited by the price of the material and by a low yield of about 20 % in making high quality products from precursors[21]. Moreover, exploiting new properties and activities of noble metal alloy nanowires has been challenging for several reasons: the non-uniformity of nanowires, inhomogeneous

nanowires with by-products, and uncontrollable variations in composition. Here we report a facile synthetic method in aqueous phase at room temperature for preparing high aspect ratio Au nanowires with various diameters. Uniform Au nanowire diameters can be controlled by surfactant-mediated bio-mineralization of genetically engineered M13 bacteriophage. This method has the following advantages: (i) a genetically selected M13 phage virus acts as a template in a process that produces homogeneous nanowires; (ii) the specific interaction between the Au-binding M13 phage and the Au precursor yields an unprecedented conversion efficiency of Au ions to Au nanowires at room temperature; (iii) the incorporation of surfactant molecules into this bioinorganic hybrid system tunes the control of diameters and morphologies of the nanowires that makes it possible to prepare nanowires with well-controlled properties. Here, we report a generalized synthetic route to prepare Au nanowires with finely tuned diameters.

M13 phage has been shown to be a functional template for fabrication of nanowires due to a filamentous structure that is composed of an identical pattern of amino acids displayed along the length of its major coat protein[22,23,24]. An insertion of additional DNA sequences into specific virus genes enables the expression of a peptide sequence on the virus that has specific affinity to select inorganic materials[25]. Here, a sequence previously selected by our group with high affinity to bind Au is displayed on 100 % of the copies of the p8 major coat protein.

3-2. Synthesis of Au nanowires from M13 phage with specific gold binding peptides

Our group previously reported specific gold binding M13 phage with peptide sequence on the major protein coat of M13 body and named it as p8#9[26]. The resultant M13 phage clone, named p8#9, displays the peptide sequence Val-Ser-Gly-Ser-Ser-Pro-Asp-Ser (VSGSSPDS) on the N-terminus of the p8 protein and thus provides strong adsorption sites along the dimensions of the phage. Each p8#9 has 2,700 copies of gold binding peptides that serve as adsorption sites both for gold ions and gold metals. The synthesis of Au nanowires with p8#9 through the direct reduction of Au^{3+} ions from sodium borohydride ($NaBH_4$) in an aqueous system was reported previously. The introduction of gold nanoparticles to the dispersion of p8#9 phage resulted gold nanowires decorated with gold nanoparticles along the M13 phage, and also the addition of gold ions followed by the reducing agent, sodium borohydride, also results gold nanowires with gold nanoparticles nucleated on the surface of M13 phage. The Au nanowires were composed of 5-7 nm Au nanoparticles that had been nucleated onto p8#9 Au binding sites (Fig. 3.1)[26]. The results demonstrated the specificity of the p8#9 phage as an excellent gold binder, but some limitations to make continuous and homogeneous gold nanowires still remained: the gold nanowires from this methods end up with nanowires composed of discrete gold nanoparticles along the phage, which is a collection of gold nanoparticles along one-dimensional biological template, and due to the fast reduction from the strong reducing agent, there were significant population of free gold nanoparticles outside of the p8#9 phage.

In this study, in order to make continuous nanowires and increase the yield of nanowires formed while decreasing the amount of extraneous nanoparticles, a mild reducing agent (ascorbic acid) was selected to suppress the fast reduction of Au^{3+} ions to Au nanoparticles and the precursors were incubated with the phage solution before the reduction. P8#9 phage does not only attract Au^{3+} ions, but also partially reduce Au^{3+} ions (yellow) to Au^{+} ions (colorless) as occurs in amine group supported Au reduction systems. The partial reduction of Au^{3+} ions via templating onto the p8#9 phage minimized the population of free Au^{3+}or Au^{+} ions in solution, and then subsequent introduction of ascorbic acid completed the formation of continuous Au nanowires shown in Fig. 3.2(a). These nanowires exhibit a continuous structure with a very rough surface that can be smoothened (Fig. 3.2(b)) by adding Ag^{+} ions immediately after introducing the reducing agent. The addition of Ag^{+} ions not only resulted in well-defined nanowire structure with less branched connection but also reduced the time for the preparation of Au nanowires, so we concluded that the Ag ions catalyzed the formation of Au nanowires. Using this sequential reduction of Au^{3+} ions with a mild reducing agent, the population of free Au nanoparticles was significantly decreased, however, the nanowires could not be easily separated and showed non-uniform structures locally.

Materials: p8#9 phage (4 x 10^9 pfu/mL) in TBS buffer, Hydrogen tetrachloroaurate (III) trihydrate ($HAuCl_4 \cdot 3H_2O$), Alfa Aesar, Au 49.5%, L- (+) Ascorbic Acid Powder, J.T. Baker, Silver nitrate ($AgNO_3$), Alfa Aesar Ag 63%

Experimental procedures

Au nanowires: 1 mL of 10 mM aqueous Au^{3+} ions were introduced to the mixture of 20 mL of p8#9 phage and 50 mL of de-ionized water and gently mixed in a horizontal shaker at room temperature for 30 minutes. Solution was shaken for another five minutes after the addition of 0.6 mL of 0.1 M L-ascorbic acid and then kept in static condition at 50 °C oven for overnight.

Au nanowires from Ag assisted growth: nanowires prepared with the same incubation and growth step from that of Au nanowires except that 0.2 mL of 10 mM aqueous Ag^+ ions introduced right after the ascorbic acid.

3-3. Synthesis of Au nanowires from a surfactant-mediated biomineralization

The introduction of CTAB (Cetyl trimethylammonium bromide), a widely used surfactant for the synthesis of Au nanoparticles, to our p8#9 phage synthesis improved the surface uniformity of Au nanowires. CTAB is water-soluble and is also compatible with p8#9 phage, which is not easily stabilized in organic and alcohol solvents. A simplified schematic diagram over the reaction time frame from 0 to 9 hours is available in Fig. 3.3. Using a surfactant-mediated synthesis technique, p8#9 phage was dispersed in CTAB solution, and Au^{3+} ions were then added to the mixture. Because the interaction between the Au^{3+} ions and p8#9 is sufficiently strong, the ions can penetrate the surfactant layer surrounding the phage and bind to its surface to make a solid nanowire. During the incubation of Au^{3+} ions, the partial reduction from Au^{3+} ions to Au^{+} ions also occurred with time and was confirmed both by the solution color change and UV-Vis absorption peak. The templated Au^{+} ions were then further reduced by ascorbic acid and Ag^{+} ions subsequently at static condition. After within thirty minutes, the nucleation of Au nanoparticles initiated and the solution color started to turn pale pink from colorless. The progress of nanowire growth was easy to observe via color changes in the solutions that arise due to changes in the oxidation states (Au^{3+} to Au^{+}) during the incubation stage, followed by the surface plasmon resonance peak of the Au colloid solution from the Au nanoparticles forming Au nanowires during the growth stage (Fig. 3.4).

The color change observed was also confirmed by UV-Vis absorption spectra in Fig. 3.5. Each curve is labeled with yellow solution, after incubation, Au nanoparticles, and Au nanowires respectively. As shown in Fig. 3.5(a), the yellow solution after the addition of Au^{3+} ions into the phage solution dispersed in CTAB showed strong

absorption around 400 nm, and after the three-hour incubation, any obvious absorption from the colorless solution was not detected. With the addition of ascorbic acid with Ag^+ ions, strong absorption from the spherical Au nanoparticles around 520 nm appeared and the peak became weakened and broadened with the formation of Au nanowires. The Au nanowires absorbed light with wavelength larger than 600 nm and the absorbance increases to longer wavelength until 1100 nm, which is the limitation of the instrument of initial UV-Vis spectrometer. Further measurements also show continuous increase of light absorption up to 1800 nm in solution phase (3.5(b)). The gradual increase of light absorption from inorganic nanowires distinguishes from any chemical infrared absorption exhibiting sharp absorption peaks. The average length of Au nanowires is about 5 micrometers, and the aspect ratios are at least 20, so based on the formula calculated for one-dimensional structure with increased aspect ratio, the existence of characteristic absorption peak at longer wavelength is expected even though these Au nanowires are not as straight as nanorods.

The advantage of using p8#9 soft templates for the preparation of Au nanowires is the production of homogeneous Au nanowires obviating the need for size selection or separation of other products such as short rods and particles. For the preparation of Scanning Electron Microscopy (SEM) image, as-prepare Au nanowires were collected after centrifugation at 7,000 rpm for ten minutes. Au nanowires, obtained as a thin film inside of the centrifuge cell were dried at ambient condition and transferred to carbon coating on SEM sample holder. The Au nanowires then further treated with thin Pt coating to prevent charging problems during the imaging. The meshwork of nanowires (Fig. 3.6(a) and (b)) has an undulating structure with well-developed pores between them.

To check the nanowire morphologies in detail, as-prepared Au nanowires without any purification step were imaged with Transmission Electron Microscopy (TEM). Due to the existence of surfactant molecules on the surface of Au nanowires, the precipitated Au nanowires were easily dispersed into the solution after vortexing (Fig. 3.4). For TEM images, samples were taken from the solution and casted to carbon-coated copper grids before and after vortex. Figure 3.6(c) is a TEM image from the nanowire precipitates showing entangled Au nanowires. Figure 3.6(d) is the TEM image from the homogeneous solution after vortexing showing discrete Au nanowire with a uniform diameter and dimensions of approximately 30 nm in diameter and 5 micrometer in length. The length is about five times the length of the M13 phage, which we believe resulted from the interaction between M13 phage and the surfactant during the mineralization. The high-resolution TEM analysis confirmed the crystalline structure of the nanowires: single crystalline (Fig. 3.6(e)) and polycrystalline (Fig. 3.6(f)) domains alternate within a nanowire. This rippled structure suggests the formation of Au nanowires that arose from the smoothening of Au nanoparticles along the phage. This growth mechanism is substantiated by the early TEM images (Fig. 3.3 lower) taken at different reaction times during nanowire growth with 40 nm in diameter. Furthermore, the pale pink color of the solution (Fig. 3.4) during the first step of growth, the nucleation of nanoparticles and the UV-Vis absorption peak around 520 nm (Fig. 3.5) all changed with the formation of continuous nanowires.

Materials: p8#9 phage (3.5×10^{10} pfu/mL) in TBS buffer, 10 mM hydrated hydrogen tetrachloroaurate ($HAuCl_4 \cdot 3H_2O$), 0.1 M L-ascorbic acid, 10 mM silver

nitrate ($AgNO_3$), and 0.1 M CTAB (Cetyl trimethylammonium bromide, Molecular Biology Grade, Calbiochem)

Experimental procedures

This is the protocol for the preparation of Au nanowires with 40 nm diameter sizes. Firstly, 0.1 M of CTAB solution is prepared by heating the solution around 30 °C with stirring. In a 50 mL plastic falcon tube, 15 mL of 0.1 M CTAB, 10 mL of de-ionized water, and with 10 mL of p8#9 dispersed in TBS buffer were added sequentially. The whole solution was mixed with a short vortex for 5 to 10 seconds. For starting the incubation and templating, 1 mL of 10 mM of Au^{3+} aqueous solution was injected to the resultant mixture of phage and CTAB and the whole solution was gently shaken for three hours at room temperature. During the incubation, the initial yellow color became paler with incubation and finally a colorless solution was prepared. The solution was then further reduced by the addition of 0.3 mL of 0.1 M ascorbic acid and 0.15 mL of 10 mM Ag^{+} solution, and kept in room temperature for another six hours or more without agitation.

After the formation of Au nanowires, the solution is stable at room temperature without any purification, but for collecting nanowires as powder, solution was spun at 3200 rpm for 15 minutes with centrifugation.

Due to the concentration errors for counting the M13 plaques from titer plates, there exists some shift in diameter sizes, but the uniformity of nanowires is maintained.

3-4. Control of diameter size of Au nanowires

To exploit the unique properties of nanowires, which is strongly dependent upon the dimensions (the size and the aspect ratio), the uniformity of nanowires is firstly required. The uniformity of as-prepared Au nanowires was confirmed from the low magnification TEM and SEM analysis. To further investigate the size-dependent properties of nanowires, Au nanowires with different diameter size and with narrow size distribution were successfully prepared by changing the concentration of phage, CTAB, and Au^{3+} precursors. The average diameter sizes of Au nanowires were controlled from 10 nm to 50 nm (Fig. 3.7) in increments of 5 and 10 nm throughout the range. The experimental procedure is almost the same with that of 40 nm Au nanowires described later this section, and the detailed information is summarized in Table 3-1. The reproducibility of Au nanowires here is affected by the concentration of p8#9, which is usually determined by counting the active colonies from the power dilution of original phage solution after each amplification, so it is possible to see a shift in mean-diameter-sizes in the synthesis from different p8#9 phage solution, but the homogeneity and the distribution of diameter size are maintained with on a phage solution. The TEM images shown in Fig. 3.7 were prepared from six different reactions to control the diameter sizes, and the average diameter obtained from the statistical calculation deviated slightly from the protocol. The average diameters of each sample in Fig. 3.7 are 9, 18, 24, 31, 38, and 50 nm from the protocol for the preparation methods of 10, 20, 25, 30, 40, and 50 nm, respectively. The histograms for the size distribution of diameter of Au nanowires are also available in Fig. 3.7. The diameter sizes of synthesized Au nanowires from the change in reactant solution shown in Table 3.1 usually results in a shift less than 3 nm in

average diameter size with similar size distribution due to the errors in phage concentration from the colony counting after each amplification step. The average diameter of each sample was determined using statistical methods after measuring the diameter of Au nanowires at more than 500 positions, where the zone axis can be defined.

The diameter of Au nanowires was thickened from 10 nm to 30 nm by changing the concentration of Au, CTAB and ascorbic acid, but there was a limitation to increase the diameter size over 30 nm. In this surfactant mediated bio-mineralization, decreasing the number of templates does not increase the diameter sizes as in general synthesis with templates. Moreover, as seen in Fig. 3.8(a), reducing the phage concentration to 10% of the original protocol resulted in small nanoparticles along the phage structure instead of continuous nanowires. The Au nanowires of larger than 35 nm diameters were formed when we doubled the concentration of phage solution while keeping the other reactants almost unchanged. We therefore concluded that a single M13 phage does not become a nanowire with larger diameter, but rather more than one M13 phage layered and conglomerated with Au^{3+} ions to produce a larger Au nanowire in this surfactant mediated system.

3-5. Control experiments from different M13 phages and different reaction conditions

As explained in previous chapter, the Au-binding M13 phage, the p8#9, resulted very homogeneous Au nanowires without size selection or separation. The p8#9 template also resulted in long-term stability of as-synthesized nanowires, which distinguishes these Au nanowires from unstable intermediate nanowires or network structures observed during the Au nanoparticle synthesis. Au nano-chains and networks can be prepared when the ions were reduced in citrate solution, but the structures are susceptible to break down to Au nanoparticles with time. Au nanorods after each synthesis is washed and collected before any un-reacted ions disrupt the structure or the uniformity. The particle size distribution of Au nanorods, prepared in the lab as a preliminary experiment for the Au nanowires, actually became worse with time when they were not washed after the synthesis and stored at room temperature. After a month, there were more nanoparticles with an ellipsoidal structure than nanorods. However, as-prepared Au nanowires in solution were stable in morphology and homogeneity more than six months at room temperature.

The advantage of p8#9 phage as a selective template for the preparation of Au nanowires over other genetically engineered M13 bacteriophage was confirmed with control experiments. There is a report for the preparation of nanowire structure from wild type M13 phage due to the various amino acids already exited on the surface of M13 coat. Moreover, both Au ions and metals have good affinity toward amine and thiol (~SH) groups, it is necessary to compare with other M13 bacteriophage as a possible

template for Au nanowires. The same experimental procedure was done with two different M13 bacteriophages, one with pure filamentous structure without extra DNA insertion for specificity (wild type, M13 KE), and the other with more negative charges (E4 phage, four glutamates on N terminus of p8). 1X TBS (Tris-Buffered Saline) was also tested in the same reaction condition because it was the dispersion medium for the p8#9, M13KE, and E4 phage used above. M13 phage without Au binding peptides (M13KE and E4 phage) were found to nucleate Au nanoparticles (Fig. 3.8(b) and (c)), but the structures were random in size and shape, and distribution of nanoparticles also varied due to the lack of specificity to bind Au^{3+} ions. The nanoparticles associated with M13KE and E4 assisted growth were smaller in size than in TBS because of the presence of nucleation sites on the M13 phage. The TEM images of Au nanoparticles prepared from E4, M13KE, and buffer solution are presented in Fig. 3.8.

3-6. Conversion efficiency of Au ions to Au nanowires

The conversion efficiency, so-called yield of the synthesis is very important for the synthesis of Au or other noble metal nano-materials, because the materials are expensive and supply-limited. Achieving the highest yields could facilitate the application of noble metal nano-materials in real devices. For the nanorods, the yield of Au nanorods from the silver-ion assisted growth was about 20 % in Murphy's synthesis using the weak reducing agent, ascorbic acid[21]. Nikoobakht and El-Sayed's approached of 99% of Au nanorods by modifying the seed capping agent from citrate to CTAB, but the aspect ratios in their synthesis were up to 5 in CTAB surfactant and up to 8 in a binary surfactant mixture with benzyldimethylammoniumchloride (BDAC), which is more hydrophobic than CTAB[27]. For the nanowires from chemical synthetic methods, yield has not been addressed much yet, but Xia and coworkers reported that the introduction of Ag nanoparticles increased the yield from 20% to about 70% in the synthesis of Au nanowires from elevated temperature in organic solvent[18].

The specific binding affinity of p8#9 clone enabled us not only to synthesize homogeneous nanowires through a straightforward technique, but also to increase the conversion efficiency of Au^{3+} ions to micron length Au nanowires to an unprecedented degree. UV-Vis spectroscopy and Inductively Coupled Plasma Optical Emission Spectroscopy (ICP-OES) were used to quantify the amount of Au^{3+} ions converted into nanowires in the synthesis using p8#9 phage and nanoparticles using other templates such as E4 phage, wild type M13 phage, and TBS buffer.

The final solutions of Au nanowires (p8#9) and nanoparticles (other genes and TBS) from each experimental set were separated after centrifugation at 5,000 rpm for 7

minutes, and each of the supernatant solution was transferred to another clean tube. Un-reacted Au ions remaining in the supernatant solution were reduced to Au by adding 1 M sodium borohydride solution. A pink to violet color, which suggests the presence of Au ions, appeared within a minute in all solutions except the supernatant solution associated with the p8#9 phage, which showed no significant absorption over the entire UV-Vis spectrum. The as-prepared Au nanowires and Au nanoparticles were collected from each experimental set and were digested with aqua regia (a mixture of hydrochloric acid and nitric acid) for two days. The amount of Au products in each sample was analyzed with inductively coupled plasma optical emission spectroscopy (ICP-OES) and the results are summarized in Table 3-2. The conversion efficiency of Au^{3+} ions to Au nanowires using p8#9 phage template assisted synthesis was found to be greater than 98%, and 44%, 31%, and 27% for E4 phage, wild type phage, and TBS buffer solution, respectively.

3-7. Confirmation of Au nanowire structure

As-prepared Au nanowires can be transferred as a thin film onto various substrates using polymeric membrane filter, which is soluble in acetone. As seen in Figure 3.9, the Au nanowire solution after the synthesis was transferred to the filtration funnel with de-ionized water (Fig. 3.9(b)). Because the solution contains extra salts from precursor and buffer solution, nanowires were washed with excess water before stamping onto a substrate. The Au nanowires collected on the white membrane filter (Fig. 3.9(c)) can be transferred to various substrates such as polycrystalline Au (Fig. 3.9(d)) and ITO (Indium Tin Oxide) glass (Fig. 3.9(e)) by stamping the nanowire film followed by removal of polymer membrane with excess acetone in static condition.

To confirm the structure of Au nanowires from X-ray Diffraction (XRD), the Au nanowire film was transferred onto an amorphous glass substrate. Figure 3.10(a) represents the XRD data matches the JCPDS data of pure Au, but the Energy Dispersive X-ray spectroscopy (EDX) revealed the existence of Ag atoms in the Au nanowires as seen in Fig. 3.10(b). The Ag atoms showed a similar pattern with Au atoms, so where the Au is highly concentrated, the Ag is also highly concentrated. Because both Au and Ag have face centered cubic structure and the lattice parameters of them are fairly similar, it is not easy to distinguish them from XRD analysis. Ag atoms, initially introduced to expedite the reaction, were found to be involved in nanowire structure, so the Au nanowires reported here are not pure Au nanowires but a mixture of Au-Ag with about 10% atomic content Ag[28]. Au-Ag nanoparticles with a core-shell structure usually exhibit two characteristic plasmon bands absorption with intensities corresponding the thickness of the shell, the nanowires here were found to be an alloy.

3-8. Role of Ag in the synthesis of Au nanowires

The role of Ag ions in the synthesis of Au nanorods both in electrochemical methods and seeded growths method is still not clear even though the synthetic methods are well established and easily reproducible. Nevertheless, the existence of Ag ions in the preparation of Au nanowires is an important factor in controlling the aspect ratio and the synthetic yields of Au nanorods. In the electrochemical synthesis, the length of the nanorods strongly depends on the concentration and the release rate of Ag ions into the system. In the seeded growth method for the preparation of Au nanorods, the addition of Ag ions in the form of $AgNO_3$ influences the yield, aspect ratio, and the crystal structure even though the mechanism is not yet elucidated. In a simple case, the increase in Ag concentration resulted Au nanorods with high aspect ratios until they reach the critical concentration limit to reduce the aspect ratio again. Murphy and coworkers could increase the yield of rods up to 50 % by adopting Ag ions in their initial procedure for the long nanorods[29].

The addition of Ag ions in these Au nanowires were initially for improving the surface structure of pure Au nanowires prepared without surfactant (Fig. 3.2), but it also reduced the reaction time to initiate changes in solution color implying the formation of Au nanoparticles. For the synthesis of Au nanowires (especially with CTAB stabilized ones), the existence of Ag is critical to obtain continuous nanowire structure, and moreover, the sequence of Ag solution introduction varied the final product as nanoparticles, nanorods, or nanowires. In a typical seed-mediated Au nanorod synthesis, CTAB, water, Au ions, Ag ions, ascorbic acids are mixed in order, and the addition of seed starts the reaction. However, in our Au nanowire synthesis, the sequence is slightly

different: in the incubation stage, CTAB, water, phage and Au ions were mixed with a short vortex and the resultant mixture was incubated for three hours. Ascorbic acid and Ag ions were introduced later to the solution in the growth stage one after another (ascorbic acid and the Ag).

The additional sequence of ascorbic acid and Ag ions to the incubated solution determines the final structure. When the Ag ions were introduced prior to the ascorbic acid like in the normal Au nanorod synthesis, short rods will agglomerate together on the surface of p8#9 phage as shown in Fig 3.11(a) and (b). The individual particle appeared to be uniform in size, but the secondary structure formed an entangled mat. Early TEM image (Fig. 3.11(c)) revealed the initial structure as discrete nanowires with aligned short rods, but free nanoparticles not templated on the phage were observed. When the sample was prepared without Ag ions, formation of spherical nanoparticles and ellipsoidal short rods dominated, and the uniformity of the final nanoparticle was greatly decreased (Fig 3.11(d)).

3-9. Preliminary experiment of Au nanowires for the electrocatalysis

For testing the activity of as prepare Au nanowires, the nanowire solution was cleaned with de-ionized water for three times to remove excess surfactant and salts in the solution. The concentrations of Au nanowires were confirmed with ICP-OES, and the concentration of final aqueous solutions were around 150 ppm (μg/mL). For the preparation of working electrodes, 20 μL solution of the Au nanowire suspension in Milli-Q water was applied onto a glassy carbon disk electrode (0.196 cm^2 geometrical surface area) substrate at an Au nanowire loading of a several μg (Table 3). After evaporating the solvent, the deposited Au nanowires thin film was covered with 15 μL of 0.05 wt% Nafion® solution to attach the Au nanowires to the glassy carbon disk. The electrode was then dried under air atmosphere with a cover glass and transferred to the electrochemical cell in Ar saturated 0.1 M KOH electrolyte.

The electrochemical studies were carried out in a three-electrode cell using a saturated calomel electrode (SCE) as the reference and a platinum wire as the counter electrode. The electrochemical measurements were conducted by using a voltamaster potentiostat (Radiometer analytical, France). All potentials, however, are referenced to the reversible hydrogen electrode potential, calibrated via the hydrogen oxidation/reduction reaction on a pure Pt rotating disk electrode in the same cell and electrolyte at the same temperature. For CO oxidation, cyclic voltammetry (CV) was conducted at a scan rate of 20 mV/s in Argon purged 0.1 M KOH electrolyte and the continuous oxidation of CO was measured in CO saturated 0.1 M KOH after bubbling CO for 25 min. In the rotating disk electrode (RDE) experiments, the working electrode was rotated in the range of 100

- 2500 rpm using a PINE Instruments AFMSRCE rotator. The electrode potential was maintained at -0.20 V [29] for 1 min prior to recording the positive potential sweep.

Au nanowires attached to a glassy carbon rotating disk electrode (RDE) without surface engineering were found to be very active for CO electro-oxidation in CO-saturated 0.1 M KOH solution (Fig. 3.12(a)). In the same condition, negligible current was detected for Au nanowire itself in Ar saturated 0.1 M KOH nor GCE alone.

To compare the activities of nanowires more quantitatively, the electrochemically active surface area was also calculated: Cyclic voltammograms of nanowires in Fig. 3.12(c) show that increasing potential in the Argon (Ar) saturated 0.1 M KOH solution in the positive sweep led to increasing current in the cyclic voltammogram, which is associated with adsorption of oxygenated species and the formation of oxides on the Au nanowires surfaces at potentials greater than ~0.85 V and ~1.25 V vs. RHE, respectively. In the negative sweep, surface oxides were reduced as indicated by a single reduction peak in the cathodic potential scan at ~1.05 V vs. RHE. The charges associated with oxide reduction on nanowires were obtained from integrating current in the CV data, where double layer current was subtracted, as shown in Fig. 3.12(c) 78 μC, 65 μC, and 45 μC for Au nanowires of 15, 30, and 40 nm, respectively. Based on 400 $\mu C/cm^2_{Au}$ for surface oxide reduction reported previously, the electrochemical surface areas (ESA) were calculated to be 0.2 cm^2, 0.16 cm^2, and 0.11 cm^2 for Au nanowires of 15, 30, and 40 nm, respectively. Cyclic voltammograms with current normalized to Au ESA are shown in Fig. 3.12(b).

For O_2 reduction reaction, all CV measurements were conducted in Ar saturated 0.1 M KOH solution with O_2 saturated reduction conditions.

3-10. Electrocatalytic activities of size controlled Au nanowires for CO oxidation reaction

To test the utility of these nanowires as electrocatalysts, for fuel cell applications, we measured the electro-catalytic activity of Au nanowires of 15, 30 and 40 nm diameter sizes for the electro-oxidation of CO molecules (Fig. 3.13). Intrinsic activity of Au nanowires with different diameters was compared in RDE measurements, where the current density (normalized to RDE geometric area) for bulk CO electro-oxidation at different rotation rates are shown in Fig. 3.13(a)-(c), displaying a mixed kinetic-diffusion controlled current from ~ 0.4 V to 1.2 V vs. RHE. In the positive-going sweep, the CO oxidation current initiates at ~ 0.4 to 0.6 V, reaching a maximum at ~ 0.8 to 1.0 V; at higher potentials, the increasing coverage with surface oxides/hydroxides (OH_{ad}) leads to a decrease in CO electro-oxidation activity, as was observed previously for Au (100) single crystal surfaces[30]. Subsequently, the gradual reduction of surface oxides in the negative-going potential scan leads to high CO oxidation currents, which are diffusion-controlled and thus strongly dependent on rotation rate[30,31].

The mass activity and specific activity are calculated from the Koutecky-Levich analysis (Fig. 3.14). Geometric RDE current density (mA/cm^2_{geo}) consists of kinetic and diffusion components, i_k and i_d, respectively. The Koutecky-Levich plots (i^{-1} vs $\omega^{-1/2}$) at four different potentials 1.02, 1.20 V vs. RHE in the positive sweep and 0.80 and 0.60 V vs. RHE in the negative sweep are shown in Fig. 3.13(d)-(f), where the simplified equation is as followed.

$$\frac{1}{i} = \frac{1}{i_k} + \frac{1}{Bc_0\omega^{1/2}}$$

The intrinsic activity of Au nanowires for bulk CO electro-oxidation in terms of kinetic current per electrochemically active surface area (ESA) of Au in the positive-going sweep is shown in Fig. 3.14(c), where kinetic currents were extracted from the RDE data by means of a Koutecky-Levich analysis and the ESA of Au nanowires was obtained from cyclic voltammetry[32]. The intrinsic activity, i.e., the activity normalized to the electrochemically active Au surface area, for CO oxidation on Au nanowires of 40 nm is much greater than those of Au nanowires with diameters of 15 nm and 30 nm as indicated by their much higher kinetic current density at voltages lower than 1.1 V vs. RHE (Fig. 3.14(c)). For example, at 0.6 V vs. RHE, a CO electro-oxidation current of 1.20 mA/cm^2_{Au} was observed for 40 nm Au nanowires, while much lower values of ~ 0.08 mA/cm^2_{Au} were found for Au nanowires of 15 and 30 nm.

Gold bulk surfaces are very active for CO electro-oxidation, and it is of particular interest to examine and compare the activity of Au nanowires to that of bulk Au[31,33,34]. The intrinsic activity for CO electro-oxidation on Au nanowires of 40 nm is comparable to that of low-index single-crystal Au surfaces under similar conditions; for example, at 0.5 V, the 40 nm diameter Au nanowires yield ~0.3 mA/cm^2_{Au} (Fig. 5d), while current densities of ~0.1, ~0.3, and ~0.7 mA/cm^2_{Au} are obtained for Au (110), Au (100), and Au (111), respectively[31]. The CO electro-oxidation activity of Au nanowires may be compared to the heterogeneously catalyzed gas-phase oxidation of CO with O_2 on Au-based catalysts dispersed in a CO and O_2 saturated water at room temperature. There, the maximum observed CO oxidation TOF (turnover frequency) was reported to be 5.4 s^{-1}, which is significantly smaller than the highest TOFs of 11 to 14 s^{-1} obtained for the electro-oxidation of CO on the most active 40 nm Au nanowires in the potential range

between 0.85 and 1.15 RHE[35]. The synthesized Au nanowires could be applied to the development of anode catalysts for the electro-oxidation of methanol in direct methanol fuel cells, for fuel cells running on CO contaminated industrial hydrogen, where CO removal via electro-oxidation is desired, or for fuel cells running on pure CO as suggested before[10].

The activities and specific value of electrochemical study are available in Table 3-3.

3-11. Electrocatalytic activities of size-controlled Au nanowires for O_2 reduction reaction (ORR)

After confirming the activities of Au nanowires in CO oxidation, we also measured the electro-catalytic activity of Au nanowires of 15, 30 and 40 nm diameter sizes for the electro-reduction of O_2 molecules. There are two different reaction pathways for reducing O_2 molecules in fuel cells. Direct pathway results water molecule without making hydrogen peroxide (H_2O_2), the intermediate species, and is known to as 4-e^- process[36]. The other pathway is interactive serial reaction of O_2 molecules to hydrogen peroxide followed by further oxidation of hydrogen peroxide to water molecules. This process is considered a less efficient way of reduction due to the possible contamination of catalysts from the adsorbed hydrogen peroxide and retarded kinetics that went through the multi-step 2-e^- process. Au is generally known to be involved in 2-e^- process and Pt is the most efficient 4-e^- process catalyst for the direct reduction of O_2. Here we tested three Au nanowires with three different diameter sizes, 15, 30, and 40 nm to investigate the size effect of catalysts that could propose any possible applications of Au nanowires as for fuel cell cathodes. Figure 3.15 shows the onset potentials of Au nanowires for ORR at rotating speed 1600 rpm in alkaline solution. Currents were not normalized to the surface area or the mass of Au nanowires, but the potential shifts toward favorable direction (0.9V vs. RHE) when the nanowire size decreases. However, the potential value is not in the working potential of commercial fuel cells, so the Au nanowires are not suitable for feasible applications so far.

3-12. Conclusion

M13 phage with specific Au binding sequences on the p8 body, p8#9 phage, was utilized as a template for the preparation of Au nanowires in a facile way. The specific interaction between the Au ions and the p8#9 resulted in homogeneous Au nanowires in CTAB solution. This surfactant mediated bio-mineralization of M13 phage enabled us to prepare Au nanowires with uniform diameter, which is tuned from 10 nm to 50 nm with 5 to 10 nm differences. Another virtue of this template is the production of very high yield of Au nanowires from precursor ions at low temperature. These micron-length Au nanowires are expected to have NIR absorption, which makes the materials a promising optical component, and we also confirmed one possible application of the Au nanowires for CO oxidation in low temperature fuel cells.

3-13. References

[1] Haruta, M., Kobayashi, T., Sano, H. & Yamada, N. Novel gold catalysts for the oxidation of carbon-monoixde at a temperature far below 0-degrees-C. *Chem. Lett.*, 405-408 (1987).

[2] Hammer, B. & Norskov, J. K. Why gold is the Noblest of all the Metals *Nature* **376**, 238-240 (1995).

[3] Valden, M., Lai, X. & Goodman, D. W. Onset of catalytic activity of gold clusters on titania with the appearance of nonmetallic properties. *Science* **281**, 1647-1650 (1998).

[4] Chen, M. S. & Goodman, D. W. The structure of catalytically active gold on titania. *Science* **306**, 252-255 (2004).

[5] Haruta, M. Size- and support-dependency in the catalysis of gold. *Catal. Today* **36**, 153-166 (1997).

[6] Kohno, H. *et al.* Role of metal impurities in the growth of chains of crystalline-silicon nanospheres. *Physica B* **308**, 1097-1099 (2001).

[7] Zhang, J., Sasaki, K., Sutter, E. & Adzic, R. R. Stabilization of platinum oxygen-reduction electrocatalysts using gold clusters. *Science* **315**, 220-222 (2007).

[8] Wang, X. J. *et al.* Polymer-encapsulated gold-nanoparticle dimers: Facile preparation and catalytical application in guided growth of dimeric ZnO-nanowires. *Nano Lett.* **8**, 2643-2647 (2008).

[9] Bhaviripudi, S. *et al.* CVD synthesis of single-walled carbon nanotubes from gold nanoparticle catalysts. *J. Am. Chem. Soc.* **129**, 1516-1517 (2007).

[10] Kim, W. B., Voitl, T., Rodriguez-Rivera, G. J. & Dumesic, J. A. Powering fuel cells with CO via aqueous polyoxometalates and gold catalysts. *Science* **305**, 1280-1283 (2004).

[11] Corma, A. & Serna, P. Chemoselective hydrogenation of nitro compounds with supported gold catalysts. *Science* **313**, 332-334 (2006).

[12] Ilieva-Gencheva, L. *et al.* Nano-structured gold catalysts supported on CeO2 and CeO2-Al2O3 for NOx reduction by CO: Effect of catalyst pretreatment and feed composition. *J. Nanosci. Nanotechnol.* **8**, 867-873 (2008).

[13] Link, S. & El-Sayed, M. A. Size and temperature dependence of the plasmon absorption of colloidal gold nanoparticles. *J. Phys. Chem. B* **103**, 4212-4217 (1999).

[14] Kim, F., Song, J. H. & Yang, P. D. Photochemical synthesis of gold nanorods. *J. Am. Chem. Soc.* **124**, 14316-14317 (2002).

[15] Sau, T. K. & Murphy, C. J. Seeded high yield synthesis of short Au nanorods in aqueous solution. *Langmuir* **20**, 6414-6420 (2004).

[16] John Turkevich, P. C. S., James Hiller. A study of the nucleation and growth proess in the synthessis of colloidal gold. *Discuss. Faraday Soc.* **11**, 55-75 (1951).

[17] Chen, H. M. *et al.* Controlling the length and shape of gold nanorods. *J. Phys. Che. B* **109**, 19553-19555 (2005).

[18] Lu, X. M., Yavuz, M. S., Tuan, H. Y., Korgel, B. A. & Xia, Y. N. Ultrathin gold nanowires can be obtained by reducing polymeric strands of oleylamine-AuCl

complexes formed via aurophilic interaction. *J. Am. Chem. Soc.* **130**, 8900-8901 (2008).

19 Wang, C., Hu, Y. J., Lieber, C. M. & Sun, S. H. Ultrathin Au nanowires and their transport properties. *J. Am. Chem. Soc.* **130**, 8902-8903 (2008).

20 Huo, Z. Y., Tsung, C. K., Huang, W. Y., Zhang, X. F. & Yang, P. D. Sub-two nanometer single crystal Au nanowires. *Nano Lett.* **8**, 2041-2044 (2008).

21 Orendorff, C. J. & Murphy, C. J. Quantitation of metal content in the silver-assisted growth of gold nanorods. *J. Phys. Chem. B* **110**, 3990-3994 (2006).

22 Nam, K. T. *et al.* Virus-enabled synthesis and assembly of nanowires for lithium ion battery electrodes. *Science* **312**, 885-888 (2006).

23 Mao, C. B. *et al.* Virus-based toolkit for the directed synthesis of magnetic and semiconducting nanowires. *Science* **303**, 213-217 (2004).

24 Lee, Y. J. *et al.* Fabricating Genetically Engineered High-Power Lithium-Ion Batteries Using Multiple Virus Genes. *Science* **324**, 1051-1055 (2009).

25 Whaley, S. R., English, D. S., Hu, E. L., Barbara, P. F. & Belcher, A. M. Selection of peptides with semiconductor binding specificity for directed nanocrystal assembly. *Nature* **405**, 665-668 (2000).

26 Huang, Y. *et al.* Programmable assembly of nanoarchitectures using genetically engineered viruses. *Nano Lett.* **5**, 1429-1434 (2005).

27 Nikoobakht, B. & El-Sayed, M. A. Preparation and Growth Mechanism of Gold Nanorods (NRs) Using Seed-Mediated Growth Method. *Chem. Mater.* **15**, 1957-1962 (2003).

28 Mallin, M. P., Murphy C.J. Solution-Phase Synthesis of Sub-10 nm Au-Ag Alloy Nanoparticles. *Nano Lett.* **2**, 1235-1237 (2002).

29 Jana, N. R., Gearheart, L. & Murphy, C. J. Seed-Mediated Growth Approach for Shape-Controlled Synthesis of Spheroidal and Rod-like Gold Nanoparticles Using a Surfactant Template. *Adv. Mater.* **13**, 1389-1393 (2001).

30 Blizanac, B. B. *et al.* Anion adsorption, CO oxidation, and oxygen reduction reaction on a Au(100) surface: The pH effect. *J. Phys. Chem. B* **108**, 625-634 (2004).

31 Blizanac, B. B., Arenz, M., Ross, P. N. & Markovic, N. M. Surface electrochemistry of CO on reconstructed gold single crystal surfaces studied by infrared reflection absorption spectroscopy and rotating disk electrode. *J. Am. Chem. Soc.* **126**, 10130-10141 (2004).

32 Bard, A. K., Faulkner, L.R. *Electrochemical Methods Fundamentals and Applications*. (Wiley).

33 Roberts Jr., J. L., Sawyer, D.T. *Electrochim. Acta* **10**, 989-1000 (1965).

34 Rodriguez, P., Fellu, J.M., Koper, T.M. Unusual adsorption state of carbon monoxide on single-crystalline gold electrodes in alkaline media. *Elcelctrochem. Commun.* **11**, 1105 (2009).

35 Ketchie, W. C., Murayama, M., Davis, R.J. Promotional effect of hydroxyl on the aqueous phase oxidation of carbon monoixde and glycerol over supported Au catalysts. *Top. Catal.* **44**, 307-317 (2007).

36 Winter, M. & Brodd, R. J. What Are Batteries, Fuel Cells, and Supercapacitors? *Chem. Rev.* **104**, 4245-4270 (2004).

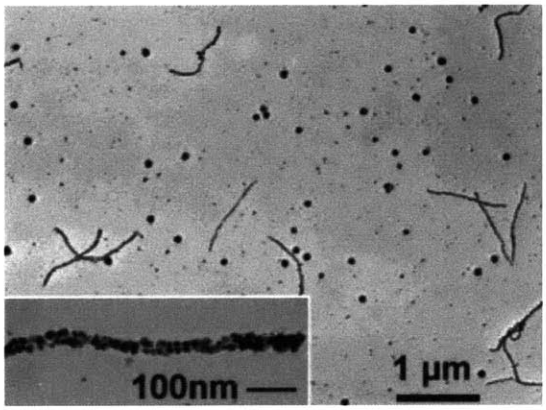

Figure 3.1 TEM images of Au nanowires[26]. M13 phage with specific Au binding sequence was utilized as a template for the preparation of Au nanowires. The nucleation of Au nanoparticles on the surface of M13 filamentous virus resulted in 1 micron-meter length nanowires at room temperature.

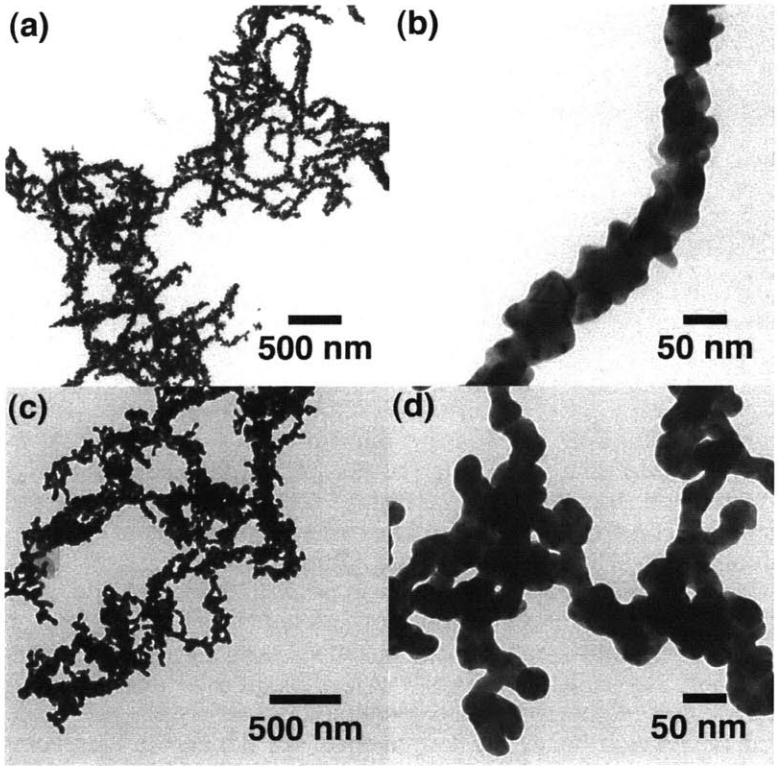

Figure 3.2 TEM images of Au nanowires with free surfaces. The incubation p8#9 and Au ions followed by the addition of mild reducing agent resulted in continuous Au nanowires. The as-prepared Au nanowires showed rough surfaces (a and b), but the addition of Ag ions during the reaction improved the surface roughness (c and d).

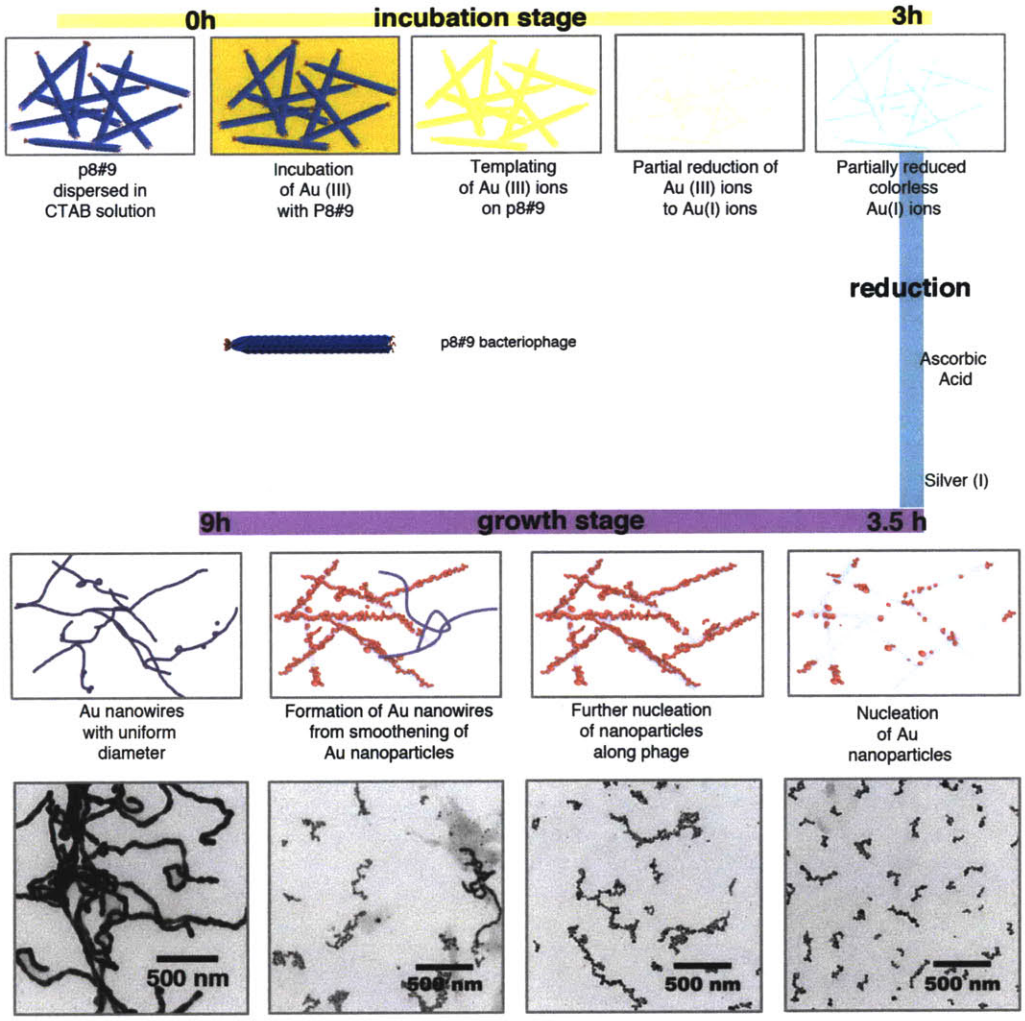

Figure 3.3 Schematic diagram for the preparation of Au nanowires from surfactant-mediated biomineralization. The preparation of Au nanowires is summarized as three different reaction stages: incubation, reduction, and growth. P8#9 phage was dispersed into the CTAB solution and Au precursors were introduced to the mixture. The resultant solution was then further incubated for three hours at room temperature. During the incubation, the Au^{3+} ions were gradually attached to the surface of p8#9 phage and partially reduced to Au^{+} ions simultaneously. Additional reduction was done by the addition of ascorbic acid and silver ions sequentially. After half hour, nucleation of spherical nanoparticle initiated, and the TEM analysis from this point showed small nanoparticles in a short chain. With time, the population of Au nanoparticles increased and the chain lengths were also increased. At a certain point, the continuous Au nanowires were observed and finally the formation of Au nanowires was completed within six hours.

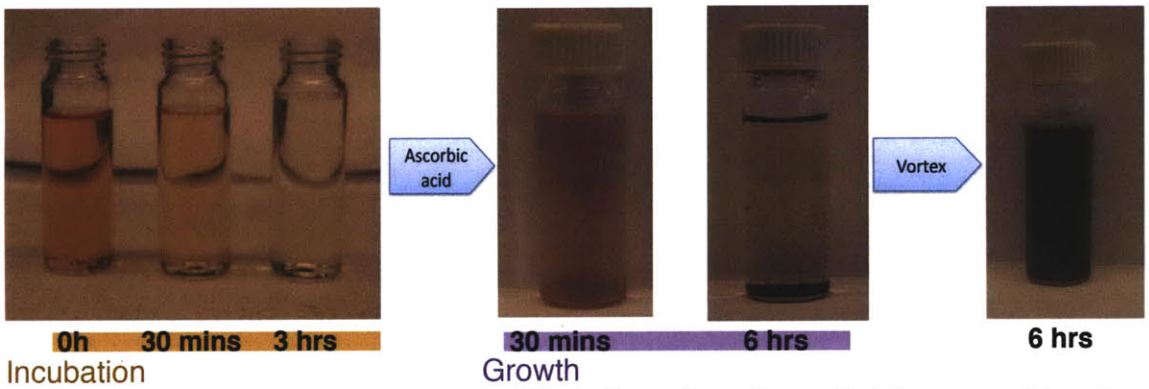

Figure 3.4 Pictures of solution taken at different reaction stages. Solutions were taken from the reaction medium to compare the color at various reaction time frames. During the incubation, the mixing of Au^{3+} ions with p8#9 dispersed in CTAB solution resulted in deep orange color (0h). The color gradually became pale yellow as Au^{3+} ions were templated to M13 phage and finally turned colorless (Au^{+} at 3 hours). When the solution was further reduced by ascorbic acids and silver ions, the growth of Au nanowires initiated with the nucleation of spherical Au nanoparticles (pink solution). The pale pink color got deeper with time, and finally the deep violet precipitates, the Au nanowires, were observed in the bottom of reaction tube. The precipitates are easily dispersed into a homogeneous solution with vortex due to the existence of CTAB layer on the surface of Au nanowires.

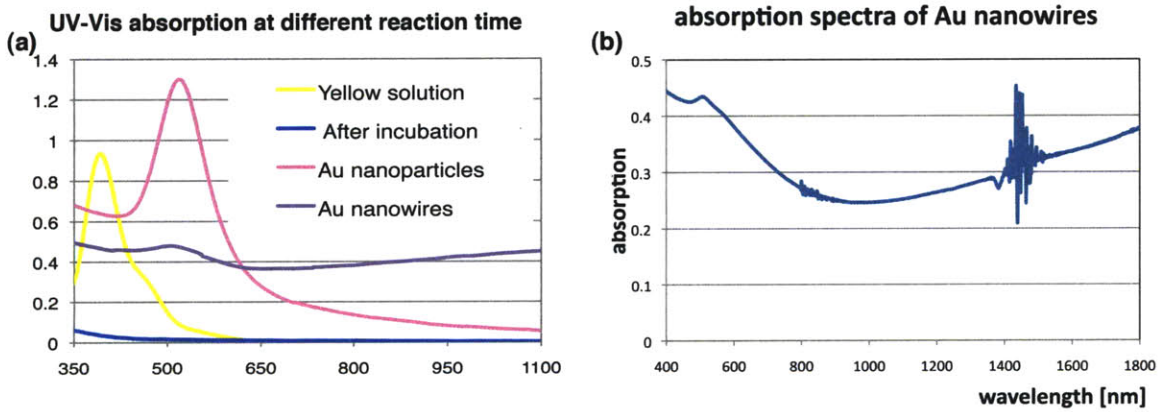

Figure 3.5 UV-Vis and NIR absorption data of Au nanowires. (a) UV-Vis absorption spectra were measured from the solutions shown in Fig. 3.4. After the addition of Au^{3+} precursor to the phage dispersion in CTAB, strong absorption peak around 400 nm appeared labeled as yellow solution. The solution color became paler with incubation, and any distinguishable absorption peak was observed from the colorless solution labeled as after incubation. With the addition of ascorbic acid and Ag^{+} ions, strong plasmon absorption peak appeared around 520 nm indicating the formation of spherical Au nanoparticles. The peak from the Au nanoparticles decreased and broadened, and new absorption phenomena appeared with the formation of continuous Au nanowires. As shown both in (a) and (b), the Au nanowires absorb light with wavelength longer than 600 nm and the absorbance increases to 1800 nm. The noise around 1400 nm came from the device setting.

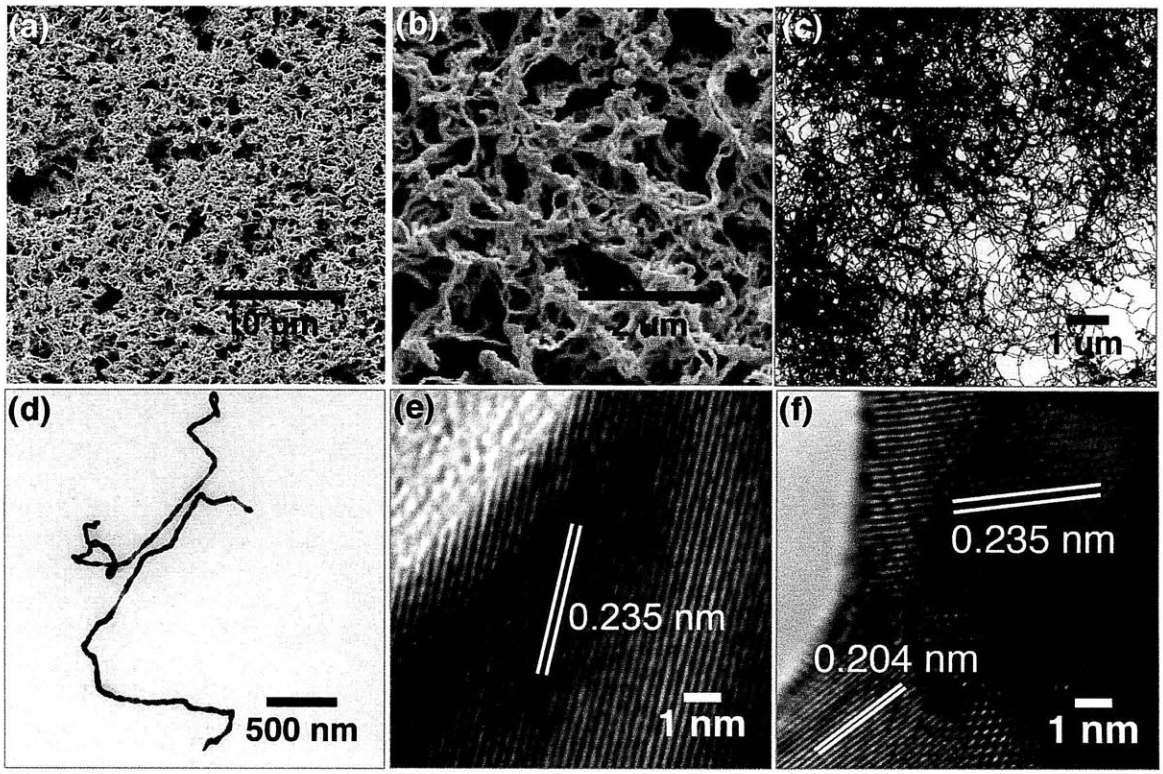

Figure 3.6 SEM and TEM images of Au nanowires. As-dried Au nanowires were uniform without any big particles in the images taken by SEM (a and b) and low-resolution TEM (c). The aggregated Au nanowires shown in (c) were imaged after casting the nanowires from the precipitates in static condition. (d) The discrete Au nanowires were imaged from the Au nanowire solution after vortex. Au nanowires showed crystalline structure with alternating single crystalline (e) and poly crystalline (f) domains.

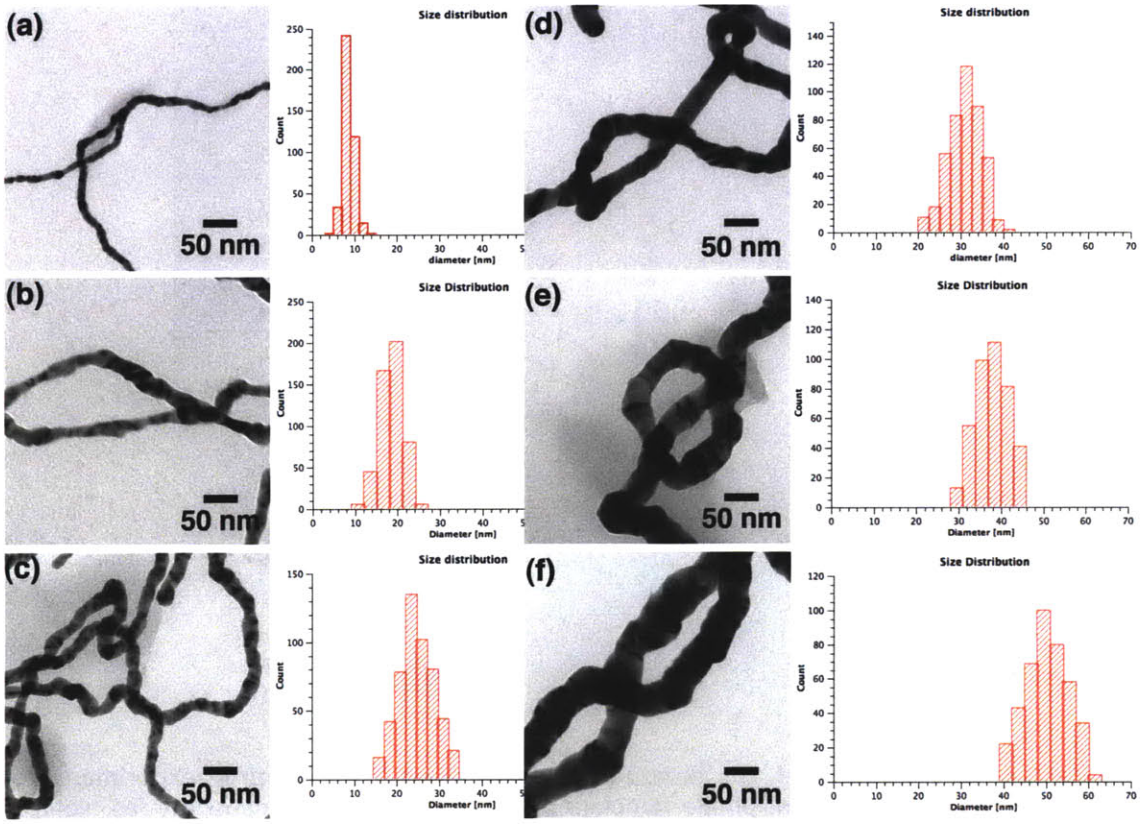

Figure 3.7 TEM images and the size distributions of Au nanowires with different diameters. Au nanowires with various diameter sizes were prepared by changing the concentration of phage, CTAB, and precursors. The TEM images were taken at a same magnification at 41,000X to compare the sizes. Due to the surface roughness between smaller crystalline domains in the nanowires, the nanowires show deviations. The average diameter sizes with the standard deviations are (a) 9±1.3 nm, (b) 18±2.7 nm, (c) 24±4.1 nm, (d) 31±3.8 nm, (e) 38±4.0 nm, and (f) 50±4.8 nm.

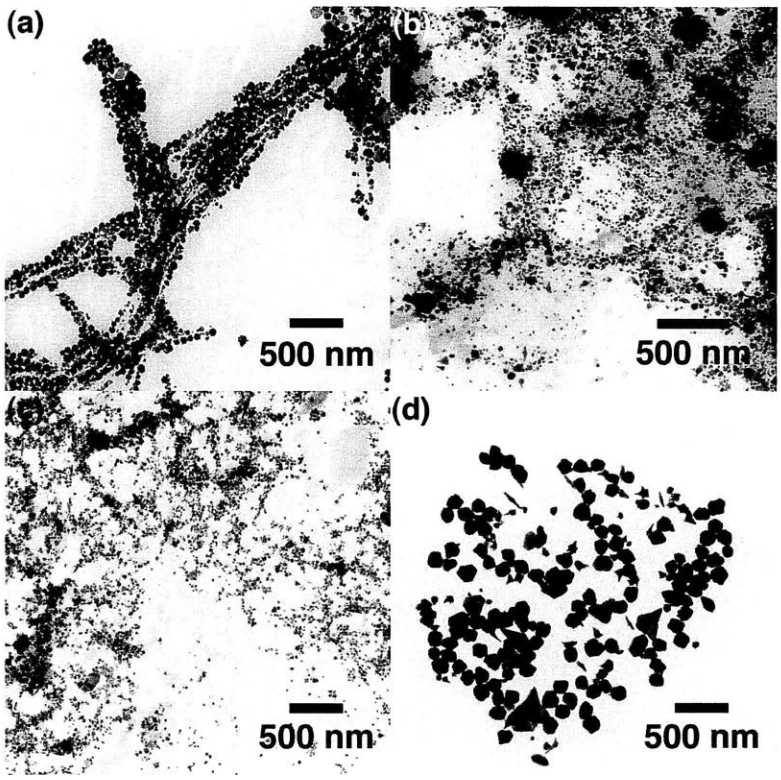

Figure 3.8 TEM images of Au nanoparticles prepared from control experiments. (a) Reducing the concentration of phage template to 10% resulted in Au nanoparticles along the phage structure instead of nanowires. (b) E4 phage of four-glutamate functionality produced random nanoparticles in sizes and distributions. (c) The wild type M13 phage (M13KE) also produced Au nanoparticles, which are smaller than other cases, but filamentous structure from the phage was not observed. (d) Due to the absence of nucleation sites from M13 phage, the Au nanoparticles prepared from the TBS buffer were much bigger than other particles.

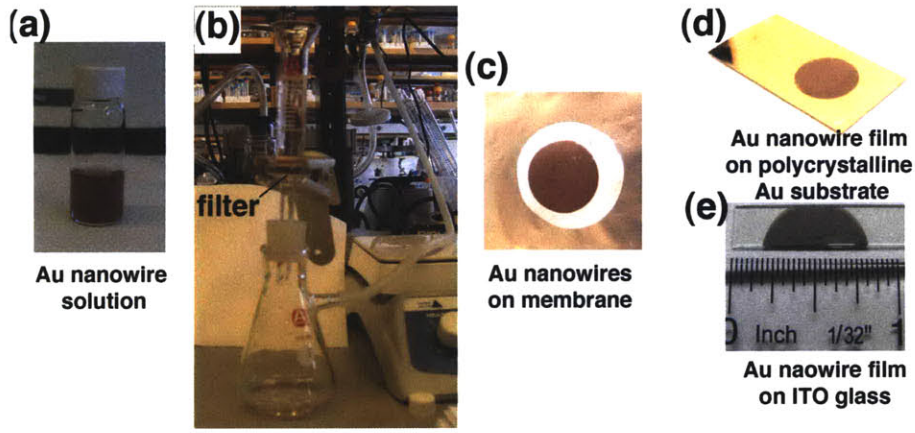

Figure 3.9 Preparation of Au nanowire film on a substrate. The as-prepared Au nanowires dispersed in water can be transferred to a thin film on various substrates. (a) Au nanowire solution after the vortex was diluted with additional de-ionized water. (b) Nanowire solution was transferred to filtration unit with membrane filter between the glass funnel and the adaptor, and the aspirator slowly pulled down the nanowire solution and the nanowires remained on top of the membrane filter. (c) Au nanowires were collected as a circle on white membrane filter. Au nanowires attached to membrane filter was transferred to (d) polycrystalline Au substrate or (e) ITO glass by dissolving the polymer membrane filter with excess acetone.

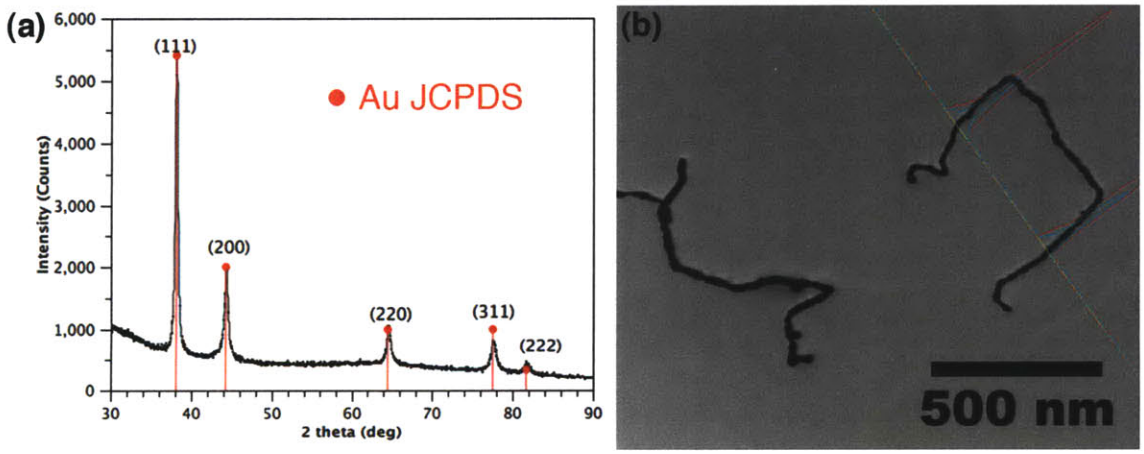

Figure 3.10 XRD and EDX result of Au nanowires. (a) The X-ray Diffraction result was matched with pure Au in JCPDS data with FCC (face-centered-cubic) structure. (b) Energy dispersive X-ray spectroscopy exhibited the existence of Ag atoms in nanowires. The distribution of Ag atoms in the nanowire structure was uniform and from the point analysis, the concentration was found to be similar with the amount of Ag added during the synthesis of nanowires.

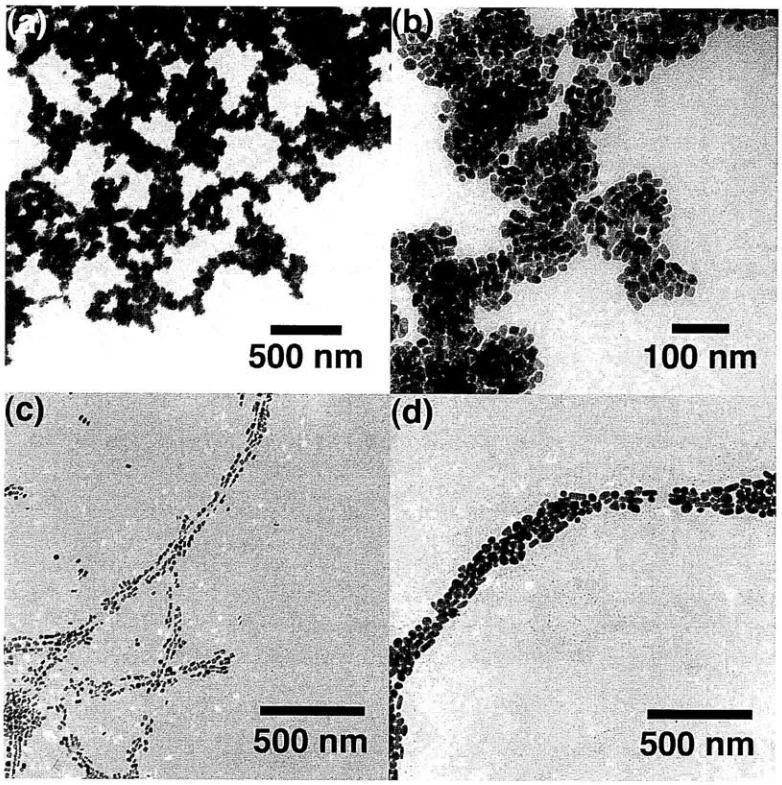

Figure 3.11 TEM images from controlled Ag experiments. When the Ag ions were introduced to the incubated solution before the addition of ascorbic acid, different structure was obtained: (a) Low-resolution TEM image shows entangled bundle structure of Au nanoparticles along phage length, (b) the individual particle looked similar in size and shape. At very early stage of particle growth, the templated structure of Au nanoparticles along the phage length was more precisely imaged (c). (d) When the sample was prepared without Ag ions, the structure looked very similar with the others.

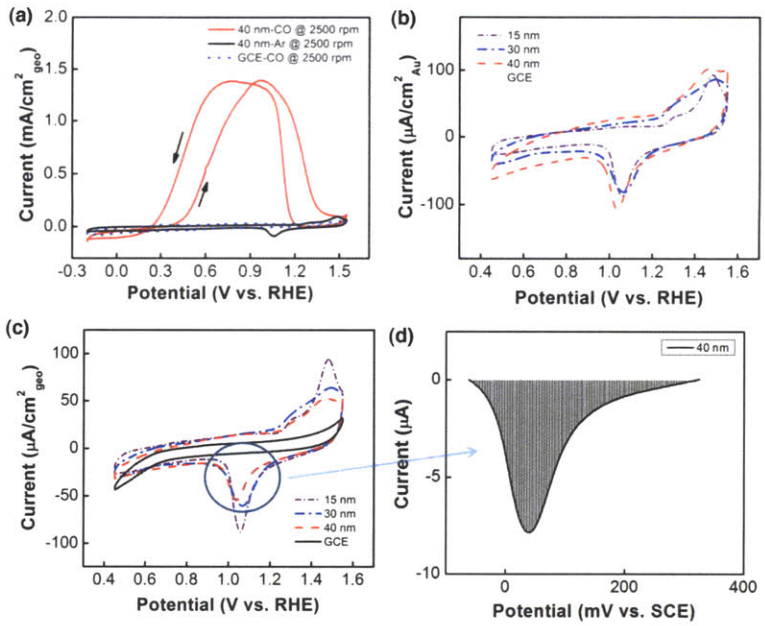

Figure 3.12 CV result of Au nanowires as preliminary experiment. (a) Cyclic voltammograms of CO oxidation with 40 nm Au nanowires/GCE in the absence (black solid) of CO and with saturated CO (red solid) in 0.1 M KOH solution with a sweep rate of 20 mV/s at a rotational speed of 2500 rpm. The cyclic voltammogram of GCE alone in saturated CO is shown for comparison (blue dot). (b) Cyclic voltammograms of Au nanowires/GCE with diameters of 15 nm, 30 nm and 40 nm in Ar purged 0.1 M KOH electrolyte at a scan rate of 20 mV/s after normalized to Au Electrochemical surface area (ESA) calculated from (c) and (d). (c) Cyclic voltammograms of Au nanowires/GCE with diameters of 15 nm, 30 nm and 40 nm and GCE alone in Ar purged 0.1 M KOH electrolyte at a scan rate of 20 mV/s, (d) integration of 40 nm Au nanowire reduction peak.

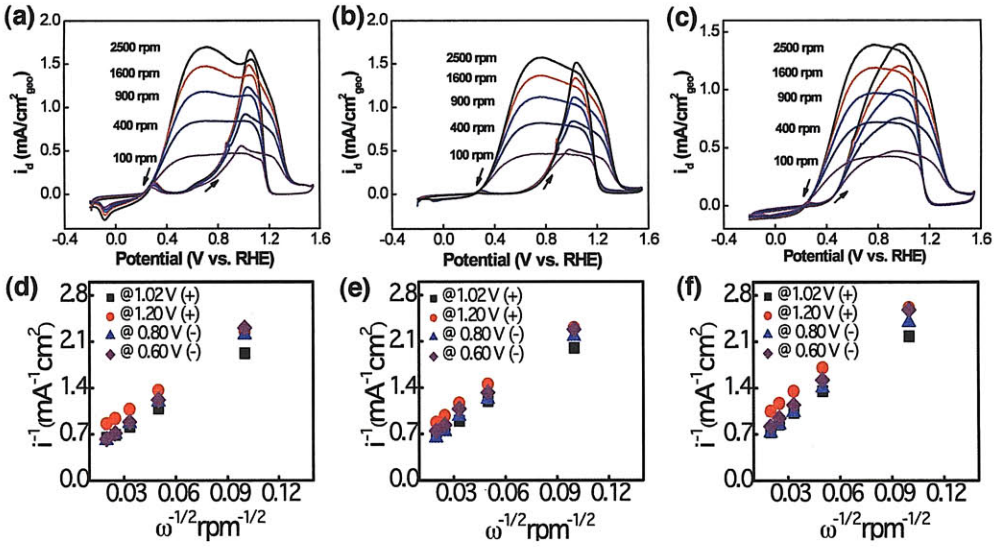

Figure 3.13 Geometric RDE current density of CO oxidation on Au nanowires with different diameter sizes. Au nanowires with different average diameters (15 nm, 30 nm, and 40 nm) were prepared and tested for CO oxidation. Geometric RDE current density of CO oxidation on Au nanowires/GC with (a) 15 nm, (b) 30 nm, and (c) 40 nm diameter in CO saturated 0.1 M KOH collected at 20 mV/s. Rotating rates are indicated in figures. Koutecky-Levich plots of (d) 15 nm, (e) 30 nm and (f) 40 nm Au nanowires from RDE measurements (a-c). Insets: (+) and (-) denote positive and negative potential sweep directions, respectively.

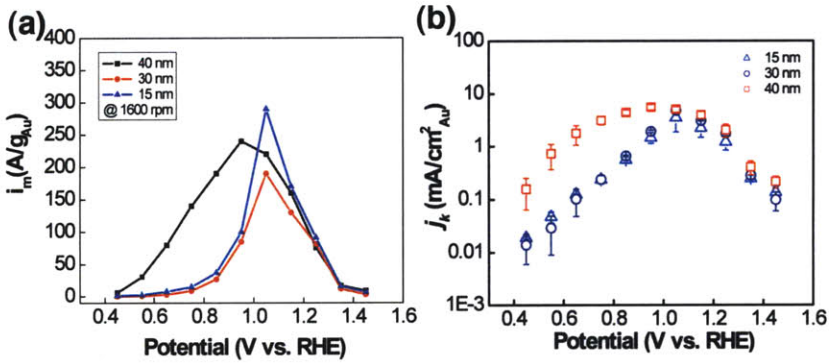

Figure 3.14 Activities of Au nanowires for CO oxidation with different diameter sizes. (a) Mass activities of Au nanowires normalized with Au mass loaded onto the electrode. (b) Specific activities of Au nanowires with deviation bar. The specific activities were normalized by the electrochemical surface area (ESA) calculated from Fig. 3.12.

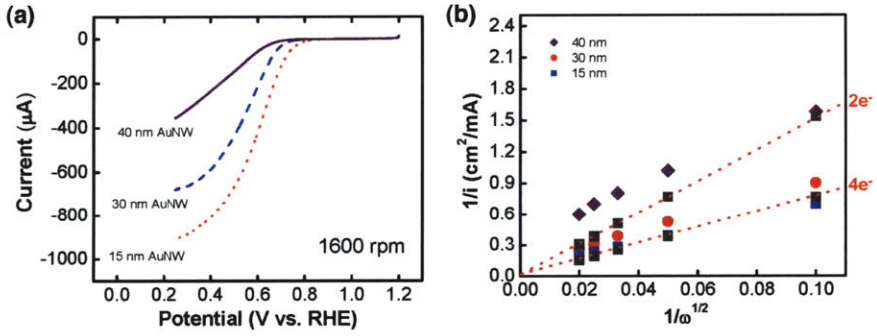

Figure 3.15 Geometric RDE current for the oxygen reduction reaction on Au nanowires with different diameter sizes. (a) The onset potential of Au nanowires shifted from 0.6 to 0.8 V vs. RHE with decreasing diameter sizes at rotation speed 1600 rpm. The Koutecky-Levich plots suggested that the three Au nanowires underwent oxygen reduction between 2 and 4 electron process.

Average diameter	CTAB [M]	P8#9 [pfu/mL]	Au^{3+} [M]	Ascorbic acid [M]	Ag^{+}[M]
50 nm	0.41	9.45×10^{9}	4.1×10^{-4}	8.1×10^{-4}	6.1×10^{-5}
40 nm	0.41	9.60×10^{9}	2.7×10^{-4}	8.2×10^{-4}	4.1×10^{-5}
30 nm	0.41	4.80×10^{9}	2.7×10^{-4}	8.2×10^{-4}	4.1×10^{-5}
25 nm	0.48	5.59×10^{9}	3.2×10^{-4}	4.8×10^{-4}	4.8×10^{-5}
20 nm	0.80	5.59×10^{9}	3.2×10^{-4}	4.8×10^{-4}	4.8×10^{-5}
10 nm	0.82	5.71×10^{9}	1.6×10^{-4}	2.4×10^{-4}	2.4×10^{-5}

Table 3-1. Table of concentrations for the preparation of Au nanowires with different diameter sizes. All the concentration except phage is in M [mol/Liter]. The unit for the phage concentration, pfu, means plaque-forming unit of M13 phages. The total volume of each synthesis varied from 30 mL to 38 mL.

Template	Product	Concentration [ppm]		Conversion efficiency [%]
		Au^{3+}	Au product	
P8#9	15 nm x 5 um	55	53.9	98
	30 nm x 5 um	55	54.3	99
	40 nm x 5 um	55	54.1	98
E4	Nanoparticles	55	24	44
Wild type	Nanoparticles	55	17	31
TBS buffer	Nanoparticles	55	15	27

Table 3-2. Conversion efficiency of Au^{3+} ions to Au nano-structures. P8#9 template converts more than 98 % of Au ions to Au in Au nanowires. The top three results come from the diameter controlled nanowires, and the conversion efficiencies from M13 phage with different genes yield values that are lower than 50 %.

AuNW (nm)	AuNW/ GCE (μg)	Oxide reduction charge (μC)	ESA of Au (cm^2_{AU})	CO oxidation onset potential[1)]	Activity[1)] @ 0.6 V		Activity[1)] @ 0.85 V	
					$i_{specific}$ (mA/cm^2_{Au})	TOF[2)]	$i_{specific}$ (mA/cm^2_{Au})	TOF[2)]
15	3.2	78	0.20	0.64	0.08	0.2	0.62	1.6
30	3.4	65	0.16	0.70	0.08	0.2	0.58	1.5
40	2.4	45	0.11	0.40	1.20	3.1	4.15	10.8

Table 3-3. Summary of the electrocatalytic activities on CO oxidation from Au nanowires of different diameter sizes. (in CO saturated 0.1 M KOH solution)

[1)] Potential (V) vs. RHE and positive scan, 1600 rpm, 20 mV/s

[2)] Turnover frequencies, TOFs (in units of s^{-1}), are calculated from the measured specific current density (A/cm^2_{Au}) divided by [2.0 × Faraday constant (96485 A·s/mol) × mole of Au surface atoms per unit area (2 $nmol_{Au}/cm^2_{Au}$)].

Chapter 4. Synthesis of Au-Ag alloy nanowires and the applications as Li-ion battery anodes

4-1. Introduction

The amount of energy stored in the lithium ion battery clearly depends on the cell's output potential and capacity, which are determined by the thermodynamics and chemistry of the system[1]. To minimize the reduction of cell voltage and thereby maximize the energy density, anode materials with very negative potential and high capacity have been searched for and studied. Metals or inter-metallic compounds that can be alloyed with lithium are promising candidates due to the high theoretical capacity[2,3]. Major challenges in these materials lie in the mechanical stress related to large volume changes and structural changes accompanied by lithium uptake and release. This mechanical stress results in pulverization and rapid capacity fading[4], which render these materials not very practical for prolonged usage. Among those materials capable of alloying with lithium, silver (Ag) and gold (Au) react with lithium at low voltage[5]. Ag and Au form several alloy phases with lithium and can alloy with a very high percentage of Li (up to $AgLi_9$ and Au_4Li_{15}) as shown in Fig. 4.1. However, little is known about the electrochemical response of Ag and Au with lithium. The available reports are mostly limited to thin film materials mainly due to the challenges in mechanical stress during the formation of alloy with Li[5,6,7,8]. When test electrodes were prepared by a normal fabrication process from powder, the capacity of Ag electrodes rapidly decays below 100 mAh/g within 10 cycles[2]. Although a thin film material can mitigate the stress related problems, the total energy stored in a thin film battery is not high enough for practical application due to the limited amount of materials in the thin film.

There is already prevailing evidence that nanostructured materials can improve the electrochemical properties of electrode materials compared to the bulk counterparts.

One-dimensionally structured nanomaterials such as SnO_2 and Si have shown improved performance as anodes for lithium ion batteries[4,9]. In addition to excellent surface activity provided by the high surface-to-volume ratio, nanowires with small diameter can relieve mechanical stress associated with the large volume change upon lithiation, as well as reduce the distance over which Li needs to diffuse.

In this work, we have synthesized nanowires of pure Ag and Au noble metals and their alloys with control over diameter, morphology and composition using two independent M13 clones, one each for specificity (p8#9) and versatility (E4). The virus-enabled synthesis of noble metal nanowires was remarkably facile resulted in high-yield compared to the traditional methods for making noble metal nanomaterials[10].

4-2. M13 phage as nanowire template of specificity and versatility

The inherent structural characteristic of the M13 virus makes this biological building block an excellent template for the synthesis of various functional nanowires with small diameter. The wild type filamentous M13 virus has a high aspect ratio with, approximately, a 6.5-nm diameter and an 880-nm length[11]. Roughly 2700 copies of p8 coat protein self-assemble into the capsid of the wild-type virus, resulting in 5 fold symmetry along the length of virus. Computational simulation of M13 virus shows that the closest distance of p8 protein neighbors is around 3 nm[12]. In addition to these structural advantages, the functionality of subunit proteins of the M13 virus can be altered through genetic engineering. Previously, the virus has been engineered to display peptides which have affinity to specific target materials and used to bind, organize and further nucleate those specific materials[12,13,14]. For example, a gold-binding virus was selected through an evolutionary screening process called biopanning. The M13 virus with a gold-binding peptide motif (VSGSSPDS) on the p8 major coat protein was named p8#9 and used for assembling gold nanoparticles[13]. In addition to the biomolecular recognition of specific materials identified through biopanning, the surface functionality of M13 virus can be modified independently through genetic engineering. The E4 virus is a modified M13 virus that has tetraglutamate (EEEE) fused to the amino terminus of each copy of the p8 major coat protein. Due to the presence of extra carboxylic acid groups compared with wild type M13 virus (M13KE), the E4 virus exhibited increased ionic interactions with cations and can serve as a template for materials growth. With this E4 virus, materials specificity was diminished, but versatility was enhanced. Our group reported successful nanowire synthesis of several functional materials such as Co_3O_4,

amorphous $FePO_4$ and single crystalline Ag nanowires on the E4 templates[15,16,17]. Here, we report the facile synthesis and improved electrochemical activity of noble metal and metal alloy nanowires using multiple virus clones for lithium ion battery anode materials. The fabrication of nanowires was done on the M13 phage modified with different p8 peptide sequences as shown in Fig. 4.2. The Ag nanowires were prepared from E3/E4 phage with three/four glutamate and all other nanowires with Au and Au-Ag alloy nanowires were grown on p8#9 phage.

4-3. Ag viral nanowires as anode

Synthesis of pure Ag nanowires was demonstrated in our previous work with E4 virus using spontaneous photo-reduction[17]. The spontaneous reduction produced straight single crystalline nanowires along the length of the virus, but the product yield was not high enough for practical application in bulk devices such as battery electrodes. To increase Ag nanowire yield, a reducing agent, sodium borohydride ($NaBH_4$), was introduced. The detailed information about the synthesis of viral Ag nanowires is available at the end of this chapter and detailed information is available in Dr. Yun Jung Lee's thesis. The clone we used was termed E4. However, upon repeated rounds of amplification and followed by sequencing, the population of virus was determined to consist of mixture of three glutamate and four glutamate residues, so it is termed E3/E4. The From the Transmission Electron Microscopy (TEM) image shown in Fig. 4.3(a), wavy polycrystalline Ag nanowires with rough surfaces were generated with the reduction with $NaBH_4$. The nanowire size was estimated to be 15 nm in diameter. The different morphology could be associated with the increased nucleation sites from the $NaBH_4$ reduction, in contrast to the limited nucleation and specific growth on the seeds already formed in a self-catalyzed spontaneous reduction. The electrochemical properties of viral Ag nanowires were tested in the voltage window of 0~2.0 V against lithium foil in Fig 4.3(b), which shows the first two discharge/charge curves. The viral Ag nanowires show pseudo-plateaus at 0.08 V and 0.02 V during the lithiation process while the removal of lithium from the alloy occurred in two steps at 0.14 and 0.3 V, in fairly good agreement with the previously reported values[6,7]. The plateaus in the potential profile stem from the two-phase coexistence regions in the phase diagrams. For a two-

component system such as Ag-Li and Au-Li, Gibbs Phase Rule determines the degree of freedom in a two-phase equilibrium regime as zero which renders the electrode potential independent of composition. While in principle all two-phase regions in the binary phase diagram should appear as plateaus, only two alloy phases have been reported to occur reversibly in the reaction with lithium[6,18]. One unknown phase (designated as phase I) appeared during the first lithiation, however, this phase was still present at the end of the de-alloying process and hence is considered irreversible[6]. Unknown phase II was related to the plateaus at 0.08 V (alloying) and at 0.3 V (de-alloying) and the AgLi β phase was associated with the 0.02 V (alloying) and 0.14 V (de-alloying) plateaus[6]. In Fig. 4.3(b), a large irreversible capacity from 0.7 V down to the first alloying plateau appeared during the first discharge. The irreversible capacity in this voltage range was partly attributed to the formation of solid electrolyte interface (SEI) formation on the electrode surface with the decomposition of electrolyte[19,20,21,22]. The irreversible capacity also arises from the Super P® carbon in the electrode. The irreversible capacity from Super P®carbon was previously reported as ~600 mAh/g[23]. This capacity from Super P® carbon was very irreversible and negligible in the following cycles. The viral Ag nanowires delivered 534 mAh/g discharge capacity in the second cycle, which corresponds to the alloy composition of $AgLi_{2.15}$.

Method

Preparation of Ag nanowires

For the viral Ag nanowires synthesis, 50 µl E3/E4 virus solution in 0.1 M TBS buffer ($2x10^{11}$ PFU/mL) was dialyzed against pH=9.5 water overnight, followed by

incubation with 2 mM, 1 mL silver acetate ($AgOOCCH_3$) solution for 12 hours in the dark at 37 °C. All solutions were aqueous after the virus dialysis. The Ag nanowires were reduced from 1 mL of 10 mM sodium borohydride ($NaBH_4$) after 4 hours at room temperature. The resulting viral nanowires were collected through filtration and washed with water several times. The collected powder was dried in a 50 °C vacuum oven overnight.

4-4. Au viral nanowires as anode

For the synthesis of pure Au nanowires, the p8#9 virus was selected for having a peptide motif expressed on the major coat protein with specific affinity to both Au ions and Au[13]. The specific Au binding sites on p8#9 not only attract the Au ions in the solution but also initiate the nucleation of spherical Au nanoparticles on the virus, so the final product was a collection of 5-7 nm Au nanoparticles along the M13 virus, rather than continuous nanowires. Therefore, we were not able to address the specific properties of Au with high aspect ratio from the previous method. To exploit the unique property of one-dimensional Au nanowires, several criteria are required: homogeneous nanowires without small particles, uniform diameter along the length, and high nanowire yield from precursors. A stepwise reduction of Au^{3+} ions from the first partial reduction during the incubation for templating to the final reduction of Au^{+} ions with mild reducing agent (ascorbic acid) resulted in Au nanowires with increasing the yield of continuous nanowires while decreasing the amount of extraneous free nanoparticles. Au^{3+} ions were introduced to the dilute aqueous p8#9 virus solution and the resultant mixture was incubated for half hour. During the incubation, the p8#9 virus attracts Au^{3+} ions in the solution and also partially reduces Au^{3+} ions to Au^{+} simultaneously. The growth of Au nanowires was completed by the addition of reducing agent at an elevated temperature to get continuous nanowire structures. Methods are available in chapter 3-2. In Fig. 4.4(a), pure Au nanowires with diameter around 40 nm demonstrated rough surfaces, which can be smoothened either by the addition of Ag ions and surfactants.

The electrochemical response of viral Au nanowires with lithium was examined in the voltage range of 0~2.0 V (measured against metallic Li) (Fig. 4.4(b)). Well-defined

plateaus were observed at 0.2 V and 0.1 V during alloying with lithium, and at 0.2 V and 0.45 V during the de-alloying process. These values are in good agreement with the limited number of reported values[3,5,8]. A large irreversible capacity was also observed between 0.7 V and 0.2 V. The specific discharge capacity was 501 mAh/g at the second cycle, which corresponds to the alloy composition of $AuLi_{3.69}$.

4-5. Synthesis of Au-Ag alloy nanowires stabilized with CTAB

To investigate the effect of noble metal alloying on the lithiation behavior, Au-Ag alloy nanowires with controlled composition were produced on p8#9. Due to the Au-specificity in the p8#9 virus, preparation of Au-Ag alloy nanowires with homogeneous composition without any segregation of single atom was done without difficulty. However, the addition of Ag atoms not only increased the Ag contents in the alloy nanowires but also reduced the roughness of the nanowires by reducing the branched structures observed in pure viral Au nanowires. To create a well-developed surfaces regardless of the Ag contents in the alloy nanowires, CTAB (cetyl trimethylammonuium bromide), a water-soluble and M13 compatible surfactant molecule was required. As we confirmed in previous chapter about the synthesis of Au nanowires (Ch. 3), the Au nanowire prepared from the surfactant-mediated bio-mineralization is strictly an alloy of Au and Ag, with Ag atoms uniformly distributed over the nanowire structure. When the concentration of Ag^{+} ions was increased, the composition of Ag atoms in nanowires increased systematically and resulted Au-Ag alloy nanowires. The compositions were confirmed both by EDX and ICP-OES, and Au-Ag alloy nanowires with 20, 33, 50, and 67 atomic % Ag content with less than 2% deviation of alloy composition were successfully prepared. Table 4.1 summarized the various compositions of Au-Ag alloy nanowires from Au and Ag precursors reproducibly prepared from p8#9 phage. The detailed synthetic methods both for the preparation of Au-Ag alloy nanowires with various compositions is as followed.

Figure 4.5(a) is the UV-Vis absorption data from nanowire with different Ag compositions, the peaks with various Ag ratios was also plotted (Fig. 4.5(b)). The fact

that the transversal band absorption in UV-Vis spectra shifted to a lower wavelength as the concentration of Ag^+ ions increased suggests that the synthesized material is not a core-shell structure but an alloy of Au and Ag atoms[24]. We therefore suggested the role of Ag atoms in this bio-mineralization from the p8#9 phage is different from the preferential adsorption of Ag-Br on a specific crystal facet and also dissimilar from the role in the synthesis of Au nanorods to control the aspect ratios or the yields[25,26,27,28].

Methods

For the synthesis of CTAB-stabilized alloy nanowires, 40 mL of p8#9 virus (1.75 x 10^{10} PFU/mL for $Au_{0.9}Ag_{0.1}$, 3.5 x 10^{10} PFU/mL for $Au_{0.67}Ag_{0.33}$, $Au_{0.33}Ag_{0.67}$, and $Au_{0.5}Ag_{0.5}$) was dispersed in 100 mL of 0.6 M CTAB solution with simple vortex. 4 mL of 10 mM Au^{3+} ions was mixed to the phage solution by inverting the solution tube. The mixture of Au^{3+} ions, p8#9, and CTAB was incubated for three hours until the yellow color completely disappeared. To complete the formation of alloy nanowires, 0.1 M ascorbic acid and 10 mM aqueous $AgNO_3$ solution were used.

For $Au_{0.9}Ag_{0.1}$ alloy nanowires, 1.2 mL ascorbic acid and 0.6 mL $AgNO_3$ solution were added and the reaction was completed at room temperature in static condition. For $Au_{0.67}Ag_{0.33}$ alloy nanowires, 0.6 mL of 0.1 M ascorbic acid and 2 mL of Ag, and for $Au_{0.5}Ag_{0.5}$ alloy nanowires, 0.6 mL of 0.1 M ascorbic acid and 4 mL of Ag were added to the solution and kept at room temperature in static condition. In case of alloy nanowires with $Au_{0.33}Ag_{0.67}$, initial volume of Au^{3+} ions was reduced to 3 mL and 6 mL of Ag was added. For all alloy materials, composition was determined in EDX quantitative point analysis and also confirmed with DCP-AES. The composition from EDX showed less

than 3% deviation from the composition, and the overall concentration measured by ICP-OES were 35:65 $Au_{0.33}Ag_{0.67}$, for 52:48 for $Au_{0.5}Ag_{0.5}$, 66:34 for $Au_{0.67}Ag_{0.33}$, and 89:11 for $Au_{0.9}Ag_{0.1}$ alloy nanowires. The diameter of alloy nanowires from each experimental set changed slightly due to the error for determining the concentration of M13 virus after each amplification step, but still maintains narrow distribution of diameter size.

4-6. Analysis of Au-Ag alloy nanowires

The representative SEM image of Au-Ag alloy nanowires prepared from p8#9 shown in Fig. 4.6(a) reveals uniform diameter along the nanowire length, and the EDX line scanning result (Fig. 4.6(b)) shows consistent tendency of the two Au and Ag atoms at different positions. The point analysis gives better numbers for indexing the nanowires (Fig. 4.9(a)). TEM image from alloy nanowires without purification step in Fig. 4.7(a) also showed homogeneous nanowires of uniform diameter without side product. The entangled nanowires can be separated after short sonication of the solution as imaged in Fig. 4.7(b). Compared with the nanowires with free surfaces shown in Fig. 4.3 and 4.4, the nanowires prepared from the surfactant-mediated method have the advantage of having more uniform diameter and reduced aggregation between nanowires. We assume that these morphological changes are related to the addition of CTAB surfactant, which serves as a surface stabilizer reducing surface energies, thus can enhance the uniformity of surface morphology. Even though the addition of CTAB diminished the surface roughness, the high-resolution TEM imaging in Fig. 4.7 (c) and (d) revealed the uneven contrast domains in a single nanowire, implying different ability to transmit electronic beam exposed to nanowires. The irregular pattern of darker and brighter contrast of nanowire was found to be alternating crystalline domains with different crystallographic domains perpendicular to the beam as shown in Fig. 4.7 (e) and (f).

These experiments uncovered a maximum limit to the Ag atom content in the Au-Ag alloy nanowires from p8#9 phage template. When the Ag^{+} precursor concentration became more than twice that of Au^{3+}, the composition of the alloy nanowires did not change, meaning that the excess Ag atoms were not incorporated into the nanowires. The

highest Ag content with the p8#9 phage template was found to be 67 atomic%. The homogeneity of alloy nanowires from the p8#9 phage was significantly disrupted when the addition of Ag^{+} became more than twice that of Au^{3+} (67% atomic Ag). As shown in Fig. 4.9(a), where four times concentration of Ag to Au was added into the phage solution, the nanowire structure appeared to be discontinuous with more Au content than Ag.

The homogeneity of the Au-Ag alloy nanowires is a critical property that depends on either the strong tendency for Au and Ag atoms to mix or the template's specific affinity to Au and Ag, or a combination of these two factors. In order to investigate the origin of the homogeneity, wild type M13 phage was tested for the growth of the Au-Ag alloys. While similar Au-Ag nanowire structures could be obtained using the wild type M13 phage as templates (Fig. 4.9(b)), the composition of Ag atoms as determined by EDX point analysis was random and differed up to five times in atomic composition within a single nanowire. The atomic composition from point analysis on Au-Ag alloy nanowires prepared from p8#9 and wild type M13 is available in Fig. 4.10. Because both Au and Ag nanomaterials were successfully prepared with CTAB surfactant, the phase separation of the two atoms is most likely due to the difference in interaction between the metals and the phage template not the surfactant molecule[29]. The versatility of E4 phage cannot uptake both Au and Ag in a consistent way resulting homogeneous alloy nanowires, therefore, the p8#9 template is found to be crucial for the preparation of alloy nanowires with well-defined structures and compositions. Therefore, to make Au-Ag alloy nanowires with excess Ag content, M13 phage with specific Ag binding peptide sequence is considered as better template.

4-7. Electrochemical study of Au-Ag alloy nanowires as Li-ion battery anodes

To explore how the degree of alloying (composition) affects the lithiation process, alloy nanowires with three different compositions were prepared and tested in a Li cell: $Au_{0.9}Ag_{0.1}$, $Au_{0.67}Ag_{0.33}$ and $Au_{0.5}Ag_{0.5}$. Compositions were determined from quantitative TEM-EDX analysis and ICP-OES. The diameters of the nanowires tested are: 30 nm for $Au_{0.9}Ag_{0.1}$, 20 nm for $Au_{0.67}Ag_{0.33}$ and 25 nm for $Au_{0.5}Ag_{0.5}$ (Fig. 4.11 (a), (c), and (e)). The galvanostatic response of the Au_xAg_{1-x} alloy nanowires did not show discrete plateaus but gradual changes in potential from 0.2 V to 0 V during discharge, and from 0 V to 0.5 V during charge, indicative of a single-phase evolution (Fig. 4.11 (b), (d), and (f)). However, as the Au composition increases close to 1, the potential profile starts to resemble that of pure Au.

To find out the alloy phases that form in the electrochemical lithiation process, XRD patterns were obtained at different stages of Li-alloying for pure Au and $Au_{0.5}Ag_{0.5}$ nanowires (Fig. 4.12). Since the potential profile of Au with Li is strikingly similar to the one for Ag-Li (except for the absolute values of the plateau potentials), and Au and Ag have the same crystal structure, we consider that similar alloy structures may form, including phase II and the β phase (AuLi, in this case) during the lithiation process. The B2-structured β phase is common to both the Au-Li and Ag-Li phase diagram. In Fig. 4.12(a), Au and ordered Au_3Li α_1 phases were identified at stage #1 of the 0.2 V discharge plateau. (Refer to Fig. 4.4(b) for the position of stage #1 and #2) At stage #2 of the 0.1 V plateau, peak intensities from Au_3Li α_1 phase were increased while the intensity of peaks from Au was decreased. No obvious formation of AuLi β phase was observed. For the $Au_{0.5}Ag_{0.5}$ alloy nanowires, only a single peak can be observed at stage #1

indicating that lithium was incorporated into a single phase of $Au_{0.5}Ag_{0.5}$. (Refer to Fig. 4.11(f) for the position of stage #1 and #2) The peaks at stage #2 were indexed as an Au_3Li-like α_1 phase with a small amount of the initial-$Au_{0.5}Ag_{0.5}$-like phase. Since the $(Au_{0.5}Ag_{0.5})_3Li$ α_1 phase has not been previously reported, further chemical composition analysis is required to identify the exact phase.

The electrochemical responses of Au_xAg_{1-x} alloy nanowires for different x are compared in Fig. 4.13. This comparison clearly shows that while Ag and Au react with significant voltage plateaus, the alloys present gradual changes in the potential profile with lithiation. In particular the $Au_{0.5}Ag_{0.5}$ material shows pseudo-single phase behavior with lithium. The single-phase like potential profile can arise for several reasons. If Ag and Au cannot separate on the time-scale of the lithiation, the starting material essentially acts like a single component material with substantial disorder. The substitutional disorder of Au and Ag creates locally varying site energies for lithium resulting in a changing potential as lithiation proceeds. Hence, such a "disordered" system acts as a single phase when lithiated with no discrete phase transitions. However, even the formation of two phases upon lithiation does not necessarily imply that the potential should be constant. If Au and Ag are mobile enough to partition between the two phases, the system can be considered a ternary with respect to the Gibbs Phase Rule and coexistence of two phases (host Au_xAg_{1-x} and ternary alloys of Au-Ag-Li) leaves one degree of freedom (Gibbs Phase Rule, F=C-P=3-2=1). Therefore the potential can be dependent on the Li content. Note that this argument becomes invalid if the kinetics of Au and Ag is so slow that they would not be able to redistribute. In that case, no

equilibrium condition can be applied for the Au and Ag distribution and the system will act as a pseudo binary.

As the Au content increases in Au_xAg_{1-x} alloys, the discharge/charge potentials increase. The discharge/charge potentials were clearly dependent on the composition. Since the potential is determined by thermodynamics, the activity of Li in the materials could be changed in the homogeneous alloy structure having values dependent on the composition. The first discharge capacity of all the alloys were all similar with values 900 ~ 965 mAh/g, but due to the high first cycle irreversible capacity, the second discharge capacities dropped to 440 ~534 mAh/g depending on the alloy composition. For most Ag and Au thin film anodes, the discharge capacity was previously reported as 500~600 mAh/g at the first cycle and decreased to 100 ~200 mAh/g in 10 cycles[8,30]. The best reported Ag thin film maintained 520 mAh/g for 10 cycles[6,7]. When a Ag electrode was prepared from bulk powder forms, the discharge capacity faded rapidly and dropped below 50 mAh/g in 10 cycles[2]. In Fig. 4.13(c), the capacity retention of the viral pure Ag, Au and alloy nanowires for 10 cycles is shown. While the pure, surfactant-free Au and Ag nanowires show rapid capacity fading, the alloys display improved capacity retention. There have been several reports that some alloys that make an active/inactive composite structure with lithium can improve cycling performance due to the buffering effect of the inactive component[31]. Other alloys that have components both active with lithium displayed stable capacity retention when the components make inter-metallic compounds that have little/moderate volume changes when alloyed with lithium[2]. Since both Au and Ag are able to alloy with lithium and their alloys have the same structure as Au and Ag, the improvement in our Au-Ag alloy system cannot be explained with the reasons listed

above. Instead, we speculate that the improvement of capacity retention in our alloy system is associated with CTAB surface stabilization and/or the pseudo-single phase behavior in potential profiles.

4-8. Composition and surfactant effects on electrochemical properties

To demonstrate how the surface stabilization and alloy formation affect the electrochemical performance of noble metal alloys, $Au_{0.9}Ag_{0.1}$ and $Au_{0.5}Ag_{0.5}$ nanowires were synthesized without CTAB surfactants. As shown in Fig. 4.14(a) and (b), surfactant-free $Au_{0.9}Ag_{0.1}$ nanowires with an average 35 nm in diameter having rough surface were templated on the virus. For facile comparison, the TEM image of $Au_{0.9}Ag_{0.1}$ nanowires stabilized with CTAB is also available in Fig. 4.14(c). The electrochemical responses in the first three galvanostatic cycles from the two nanowires with different surfaces were almost identical with slightly different specific capacities (Fig. 4.14(d)). However, as shown in Fig. 4.14(e), capacity retention for 10 cycles shows a clear difference. The specific capacity of surfactant-free nanowires decreased rapidly within 10 cycles, while that of nanowires with CTAB-stabilized surface showed rather moderate fading. For the nanowires with CTAB-stabilized surface, particle-coalescence upon cycling could be suppressed due to presence of the surface adsorbed CTAB. In addition, nanowires grown without CTAB are more branched, thus could experience more homogenizing force by Oswald ripening which leads to poor cycling performance.

One might argue the different number of virus template is the reason for better cycling performance for the CTAB-stabilized alloys, since the virus to metal ratio is higher (about 5 times) for CTAB-stabilized alloys than for surfactant-free ones (Supporting information). When surfactant-free nanowires with the [virus]/[metal] ratios as high as CTAB-stabilized ones were synthesized and tested, there was no significant change in the cycling performance thereby ruling out the possible template effect in the experimental condition used here.

Although CTAB stabilization can improve cycling performances, there can be another explanation for the better capacity retention for the Au_xAg_{1-x} alloy nanowires. Strain in a material depends not on the overall volume change of the lithiation reaction, but on the inhomogeneity of that volume change. Two-phase reactions are inherently inhomogeneous with a reaction front separating both phases. Similarly, poor diffusion kinetics can lead to concentration gradients and hence inhomogeneous volume change. These inhomogeneities caused by direct lithium gradients in two-phase coexistence are believed to be one of the reasons for poor capacity retention[32]. In terms of reaction homogeneity, the pseudo-single phase behavior in the potential profile for Au_xAg_{1-x} alloys can therefore be beneficial. However, it is difficult to tell in this study if both homogeneity and surface stabilization are relevant or if only one of them is relevant for the better cycling performance.

In order to clearly check the importance of surface stabilization and reaction homogeneity, surfactant-free $Au_{0.5}Ag_{0.5}$ alloy nanowires were also investigated. The TEM images of both surfactant-free and surfactant-stabilized $Au_{0.5}Ag_{0.5}$ alloy nanowires are available in Fig. 4.15. The potential profiles of the two $Au_{0.5}Ag_{0.5}$ alloy nanowires with different surfaces were almost identical but the surfactant-free one displayed lower specific capacity (Fig. 4.15(d)). Contrary to the Au-rich $Au_{0.9}Ag_{0.1}$ alloy, the capacity retention for 10 cycles was similar for both CTAB-stabilized and surfactant free nanowires for $Au_{0.5}Ag_{0.5}$ alloy (Fig. 4.15(e)). The specific capacity was moderately stable for 10 cycles for both nanowires. This result implies that the capacity retention can be improved by forming alloys with composition close to Au: Ag = 1: 1 even without

surface stabilization. However, for an $Au_{0.9}Ag_{0.1}$ alloy that is less alloyed and more close to pure Au, surface characteristics dominate capacity retention.

The synthetic condition of surfactant free alloy nanowires is described below.

Methods

Synthesis of $Au_{0.9}Ag_{0.1}$ viral nanowires Au-Ag alloy nanowires with 10% Ag contents were prepared from the same incubation condition with Au viral nanowires described above, but the addition of 1.5 mL of 10 mM aqueous $AgNO_3$ solution, which was immediately followed after the addition of ascorbic acid, resulted in Au-Ag alloy nanowires with smoother surfaces when the solution was kept in static condition at 50 °C.

Synthesis of $Au_{0.5}Ag_{0.5}$ viral nanowires To make alloy nanowires with higher Ag content, the amount of Au^{3+} ions introduced to the phage solution was reduced. For the preparation of Au-Ag alloy nanowires with 50% Ag contents, 7.5 mL of 10 mM Au^{3+} ions were added to the mixture of 200 mL of p8#9 phage (4×10^9 PFU/mL) and 500 mL of de-ionized water. The resultant solution was incubated for 30 minutes at room temperature, and the sequential addition of 1.2 mL of 0.1 M L-ascorbic acid and 7.5 mL of 10 mM aqueous $AgNO_3$ solution resulted in Au-Ag nanowires with 1:1 atomic ratio.

Synthesis of CTAB-free Au_xAg_{1-x} alloy nanowires with higher virus concentration

As described in synthetic methods (also see the synthesis for CTAB-stabilized alloys), the ratios of virus templates to metal precursors varied in two cases: the surfactant free synthesis and the CTAB-stabilized ones. The ratios for both cases were

optimized from experiments. Since the [virus]/[metal] ratio is about five times lower in synthesis of CTAB-free than those with CTAB surfactant, surfactant-free nanowires with the [virus]/[metal] ratios as high as CTAB-stabilized ones were also synthesized and tested for $Au_{0.9}Ag_{0.1}$ and $Au_{0.5}Ag_{0.5}$ to rule out the concentration effect of M13 phage template. The performance improvement from the virus template was found to be saturated after the optimum point of [virus]/[metal] in surfactant-free synthesis, so retention property from increased number of [virus]/[metal] did not resulted in any significant improvement.

4-9. Conclusion

Reducing the material dimension proved to be effective in decreasing mechanical stress, however, other factors such as homogeneity and surface stabilization appeared more influencing for the nanowires with diameter below 50 nm in this study based on capacity retention of pure Ag nanowires. Surfactant-free pure Ag nanowires with rough surface showed poor cycling performance even with the smallest particle size among the tested nanowires (15~20 nm). To numerically show the importance of surface stabilization and alloy formation, the 2^{nd} and 10^{th} discharge capacities and diameters for various viral nanowires tested are summarized in Table 4-2. Although the alloy nanowires with diameters below 30 nm showed moderate improvement in cycling performance up to 10 cycles, all alloy nanowires eventually failed to maintain stable capacity when tested up to 20 cycles. Further designing alloy nanostructures on the virus template to suppress coalescence is under investigation for better cycling performance.

Biological systems offer capabilities for environmentally benign materials synthesis. The two M13 viruses, genetically engineered for specificity (p8#9 virus) and versatility (E4 virus), served as a template for the synthesis of noble metal nanowires with diameters below 50 nm. The inherent structural characteristic of the M13 virus enabled the synthesis of high aspect ratio nanowires. With the synergetic combination of biological building blocks and synthetic chemistry, this facile and high yield synthesis conferred controls over particle size, morphology and compositions. The biologically derived noble metal and alloy nanowires with diameter below 50 nm showed electrochemical activities toward lithium comparable to thin film electrodes. Improvement in capacity retention was achieved by tailoring particle size, alloy

formation and surface stabilization. Because Au and Ag react poorly with lithium at the micron scale, fundamental study on their electrochemical behavior has been limited so far. Although these materials are not as cost-effective as existing anode materials, these nanowires serve as a model system in identifying important parameters that can induce stable electrochemical transformation at the nanoscale. This study elucidated the importance of surface characteristics and reaction/phase homogeneity in maintaining structural stability and electrochemical performances at the nanoscale. The principles found in this model system can be applied to improve structural stability of other technologically important alloy material systems. With advantages of facile and environmentally benign synthesis, M13 biological platform proved itself as a useful toolkit for the study on the basic electrochemical property of materials.

4-10. References

[1] Armand, M. & Tarascon, J. M. Building better batteries. *Nature* **451**, 652-657 (2008).

[2] Yin, J. T. *et al.* New Ag-Sn alloy anode materials for lithium-ion batteries. *J. Electrochem. Soc.* **150**, A1129-A1135 (2003).

[3] Laik, B. *et al.* Silicon nanowires as negative electrode for lithium-ion microbatteries. *Electrochim. Acta* **53**, 5528-5532 (2008).

[4] Chan, C. K. *et al.* High-performance lithium battery anodes using silicon nanowires. *Nat. Nanotechnol.* **3**, 31-35 (2008).

[5] Taillades, G., Benjelloun, N., Sarradin, J. & Ribes, M. Metal-based very thin film anodes for lithium ion microbatteries. *Solid State Ionics* **152**, 119-124 (2002).

[6] Taillades, G. & Sarradin, J. Silver: high performance anode for thin film lithium ion batteries. *J.Power Sources* **125**, 199-205 (2004).

[7] Morales, J., Sanchez, L., Martin, F., Ramos-Barrado, J. R. & Sanchez, M. Synthesis, characterization, and electrochemical properties of nanocrystalline silver thin films obtained by spray pyrolysis. *J. Electrochem. Soc.* **151**, A151-A157 (2004).

[8] Yuan, L. *et al.* Mesoporous gold as anode material for lithium-ion cells. *J. New Mat.Electrochem. Syst.* **10**, 95-99 (2007).

[9] Park, M. S. *et al.* Preparation and electrochemical properties of SnO2 nanowires for application in lithium-ion batteries. *Angew. Chem.-Int. Edit.* **46**, 750-753 (2007).

[10] Lee, Y., Kim, J. H.,Yun, D.S., Nam, Y.S., Qi, J., Gasteiger H. A.,Yang, S.H. and Belcher, A.M. A Genetic Template for Facile Synthesis of Homogeneous Au-M (M: Ag, Pt, Pd) Alloy Nanowires. *submitted* (2010).

[11] Kay, B. K., Winter, J , McCafferty, J. *Phage Display of Peptides and Proteins: A Laboratory Manual* (1996).

[12] Mao, C. B. *et al.* Virus-based toolkit for the directed synthesis of magnetic and semiconducting nanowires. *Science* **303**, 213-217 (2004).

[13] Huang, Y. *et al.* Programmable assembly of nanoarchitectures using genetically engineered viruses. *Nano Lett.* **5**, 1429-1434 (2005).

[14] Lee, S. K., Yun, D. S. & Belcher, A. M. Cobalt ion mediated self-assembly of genetically engineered bacteriophage for biomimetic Co-Pt hybrid material. *Biomacromolecules* **7**, 14-17 (2006).

[15] Nam, K. T. *et al.* Virus-enabled synthesis and assembly of nanowires for lithium ion battery electrodes. *Science* **312**, 885-888 (2006).

[16] Lee, Y. J. *et al.* Fabricating Genetically Engineered High-Power Lithium-Ion Batteries Using Multiple Virus Genes. *Science* **324**, 1051-1055 (2009).

[17] Nam, K. T., Lee, Y. J., Krauland, E. M., Kottmann, S. T. & Belcher, A. M. Peptide-mediated reduction of silver ions on engineered biological scaffolds. *Acs Nano* **2**, 1480-1486 (2008).

[18] Huggins, R. A. Lithium alloy negative electrodes. *J. Power Sources* **81**, 13-19 (1999).

[19] Aurbach, D. *et al.* New insights into the interactions between electrode materials and electrolyte solutions for advanced nonaqueous batteries. *J. Power Sources* **81**, 95-111 (1999).

[20] Hassoun, J., Derrien, G., Panero, S. & Scrosati, B. A nanostructured Sn-C composite lithium battery electrode with unique stability and high electrochemical performance. *Adv. Mater.* **20**, 3169-3175 (2008).

[21] Kim, H. & Cho, J. Superior Lithium Electroactive Mesoporous Si@Carbon Core-Shell Nanowires for Lithium Battery Anode Material. *Nano Lett.* **8**, 3688-3691 (2008).

[22] Yang, X. L., Wen, Z. Y., Xu, X. X., Lin, B. & Lin, Z. X. High-performance silicon/carbon/graphite composites as anode materials for lithium ion batteries. *J. Electrochem. Soc.* **153**, A1341-A1344 (2006).

[23] Gómez Cámera, J. L. *et al.* Nanosized Si/cellulose fiber/carbon composites as high capacity anodes for lithium-ion batteries: A galvanostatic and dilatometric study. *Electrochim. Acta* **54**, 6713-6717 (2009).

[24] Link, S., Wang, Z. L. & El-Sayed, M. A. Alloy formation of gold-silver nanoparticles and the dependence of the plasmon absorption on their composition. *J. Phys. Chem. B* **103**, 3529-3533 (1999).

[25] Nikoobakht, B. & El-Sayed, M. A. Preparation and growth mechanism of gold nanorods (NRs) using seed-mediated growth method. *Chem. Mater.* **15**, 1957-1962 (2003).

[26] Liu, M., Guyot-Sionnest, P. Mechanism of Silver(I)-Assisted Growth of Gold Nanorods and Bipyramids. *J. Phys. Chem. B* **109**, 22192-22200 (2005).

[27] Jana, N. R., Gearheart, L. & Murphy, C. J. Seed-mediated growth approach for shape-controlled synthesis of spheroidal and rod-like gold nanoparticles using a surfactant template. *Adv. Mater.* **13**, 1389-1393 (2001).

[28] Sau, T. K. & Murphy, C. J. Seeded high yield synthesis of short Au nanorods in aqueous solution. *Langmuir* **20**, 6414-6420 (2004).

[29] Jana, N. R., Gearheart, L., Murphy, C.J. Wet chemical synthesis of silver nanorods and nanowires of controllable aspect ratio. *Chem. Commun.*, 617 (2001).

[30] Xue, M. Z., Cheng, S. C., Yao, J. & Fu, Z. W. Fabrication and lithium electrochemistry of Ag2Se thin film anode. *Electrochim. Acta* **51**, 3287-3291 (2006).

[31] Idota, Y., Kubota, T., Matsufuji, A., Maekawa, Y. & Miyasaka, T. Tin-based amorphous oxide: A high-capacity lithium-ion-storage material. *Science* **276**, 1395-1397 (1997).

[32] Kwon, Y., Kim, H., Doo, S. G. & Cho, J. H. Sn0.9Si0.1/carbon core-shell nanoparticles for high-density lithium storage materials. *Chem.Mater.* **19**, 982-986 (2007).

[33] Pelton, A. The Au–Li (Gold-Lithium) system. *Journal of Phase Equilib.* **7**, 228-231 (1986).

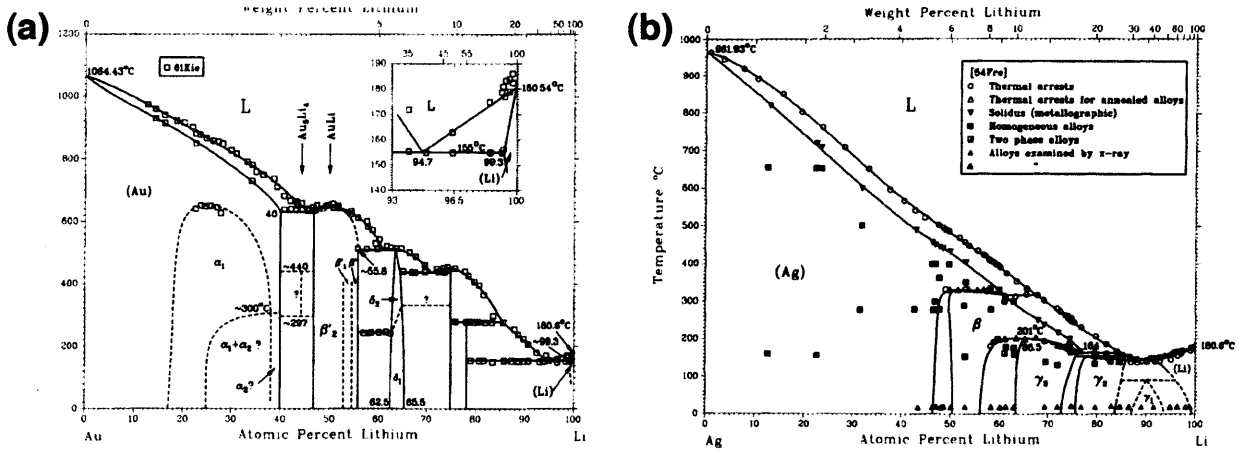

Figure 4.1 Binary alloy phase diagrams of Au and Ag with Li[33]. The binary phase diagram of Au-Li and Ag-Li show various alloy phases. From the phase diagram, each atom can uptake Lithium up to $AgLi_9$ and Au_4Li_{15}.

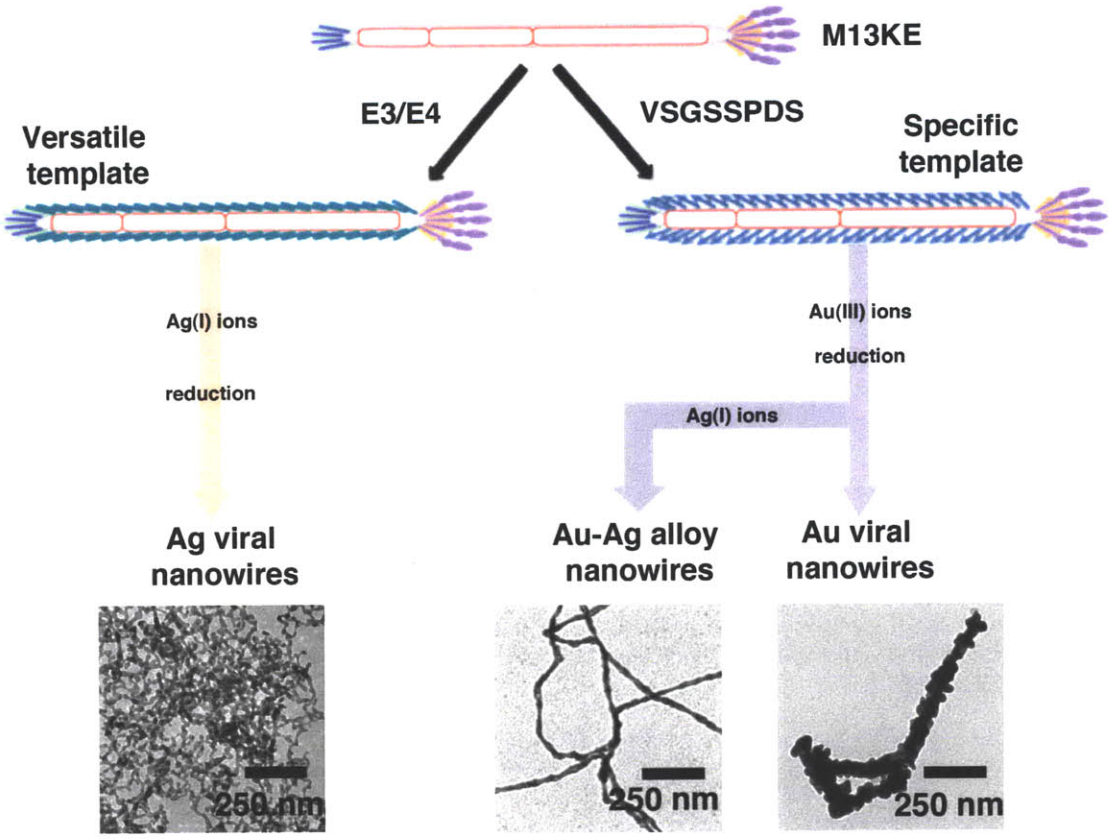

Figure 4.2 Schematic diagram for the preparation of Ag, Au, and Au-Ag alloy nanowires from different phage templates. Genetic modification of wild type M13 can express specific peptide sequences. The modification of p8 protein resulted in E4 and p8#9 with different functionality, thus served as templates for different inorganic structures. E4, the versatile template produced Ag viral nanowires whereas p8#9, the specific template for Au, formed pure Au nanowires and Au-based alloy nanowires with various compositions.

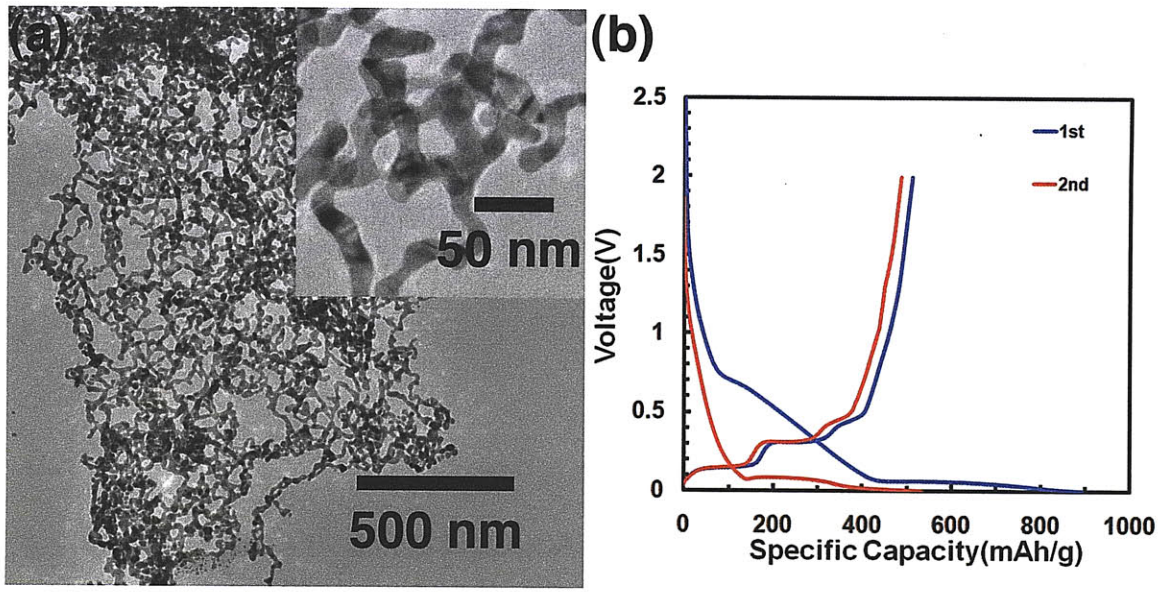

Figure 4.3 Ag viral nanowires as anode. (a) The wavy Ag viral nanowires were grown on the surface of E4 phage. (b) First two discharge/charge curves tested between 0 to 2.0 V with active mass of 4.28 mg/cm^2.

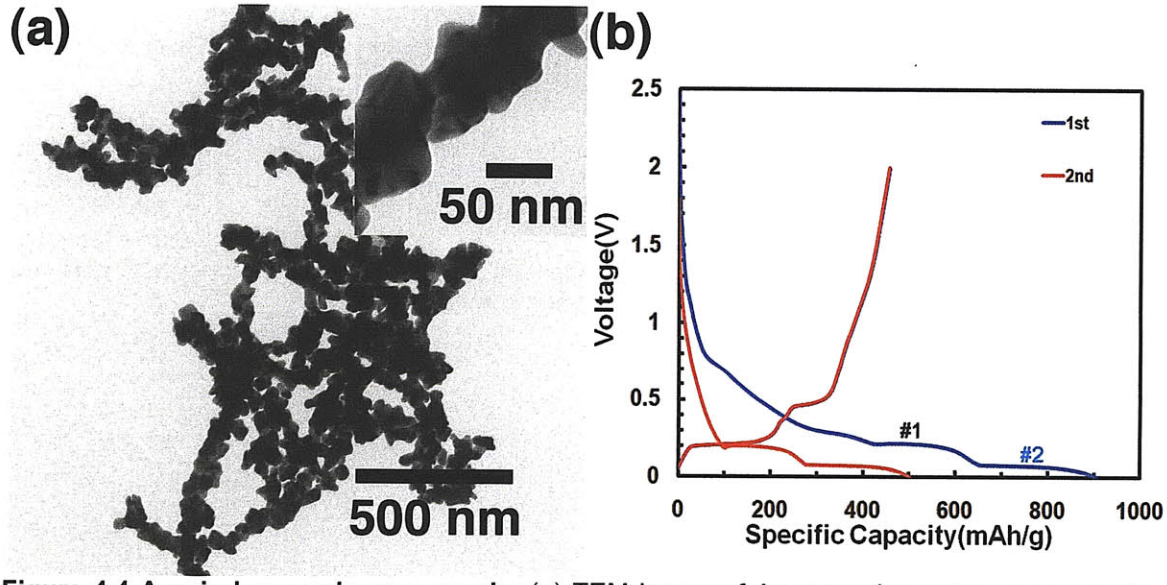

Figure 4.4 Au viral nanowires as anode. (a) TEM image of Au nanowires were grown on the surface of p8#9 phage with specific Au binding peptides. (b) Fist two discharge/charge curves tested between 0 and 2.0 V with active mass of 5.55 mg/cm^2 and current density of 50 mA/g. The notation #1 and #2 will be explained later about the thermodynamic phase formed between Au and Li.

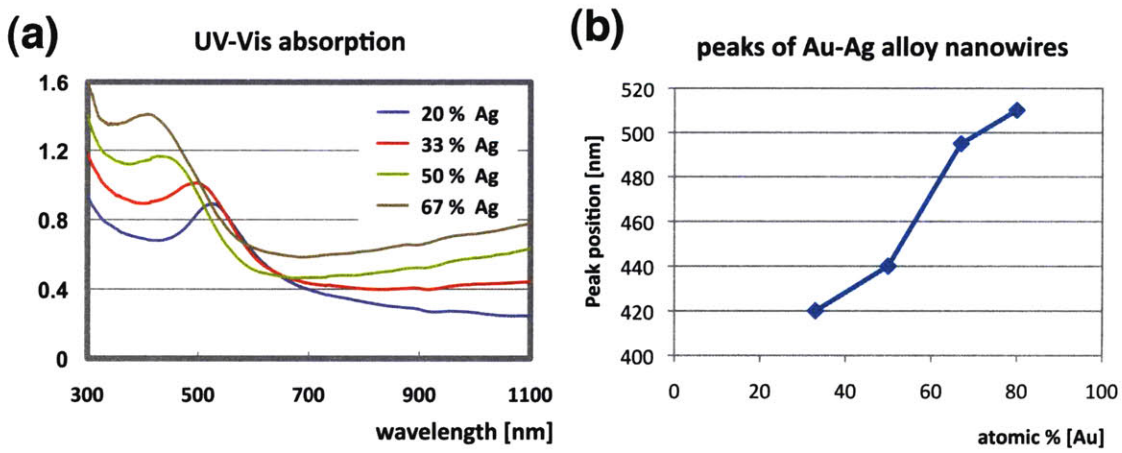

Figure 4.5 UV-Vis absorption of Au-Ag alloy nanowires of various compositions. (a) The transversal plasmon resonance absorption peak of Au-Ag alloy nanowires shifted to shorter wavelength as the composition of Ag increased. The atomic composition and the wavelength of peak were plotted in (b).

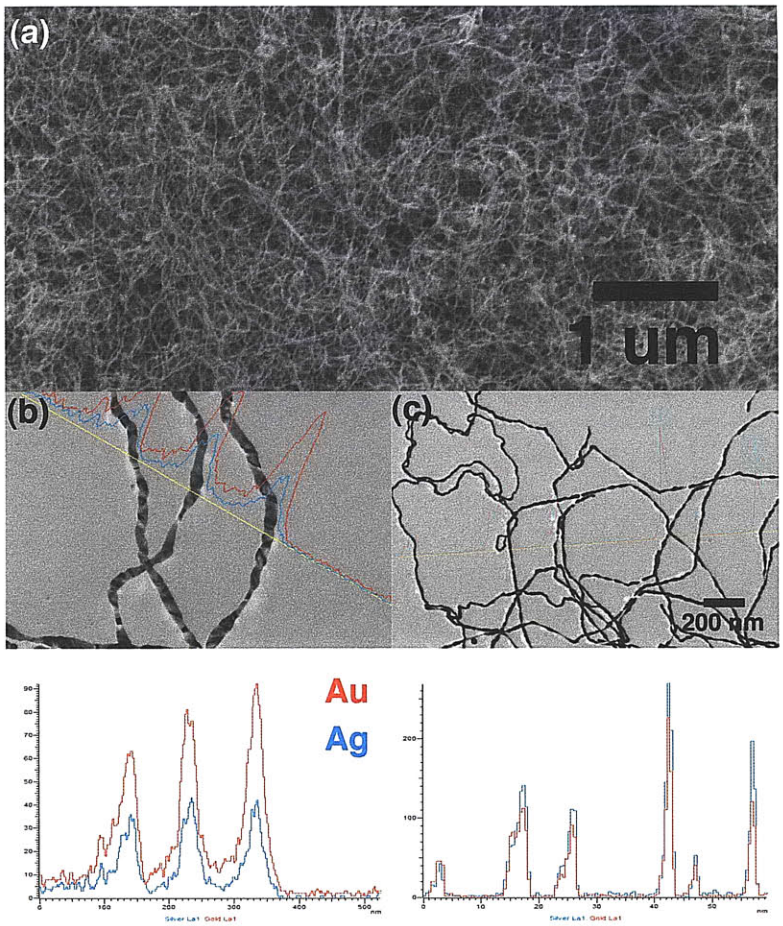

Figure 4.6 Au-Ag alloy nanowires prepared from modified synthetic route from Au nanowires. (a) SEM image of as-prepared nanowires (Au:Ag=2:1) showed pores between nanowires. The Au-Ag alloy nanowires are straighter than Au. The line scanning result of nanowires with different Au and Ag ratios confirmed the composition number from ICP-OES. (b): Au:Ag=2:1 and (c): Au:Ag=1:1

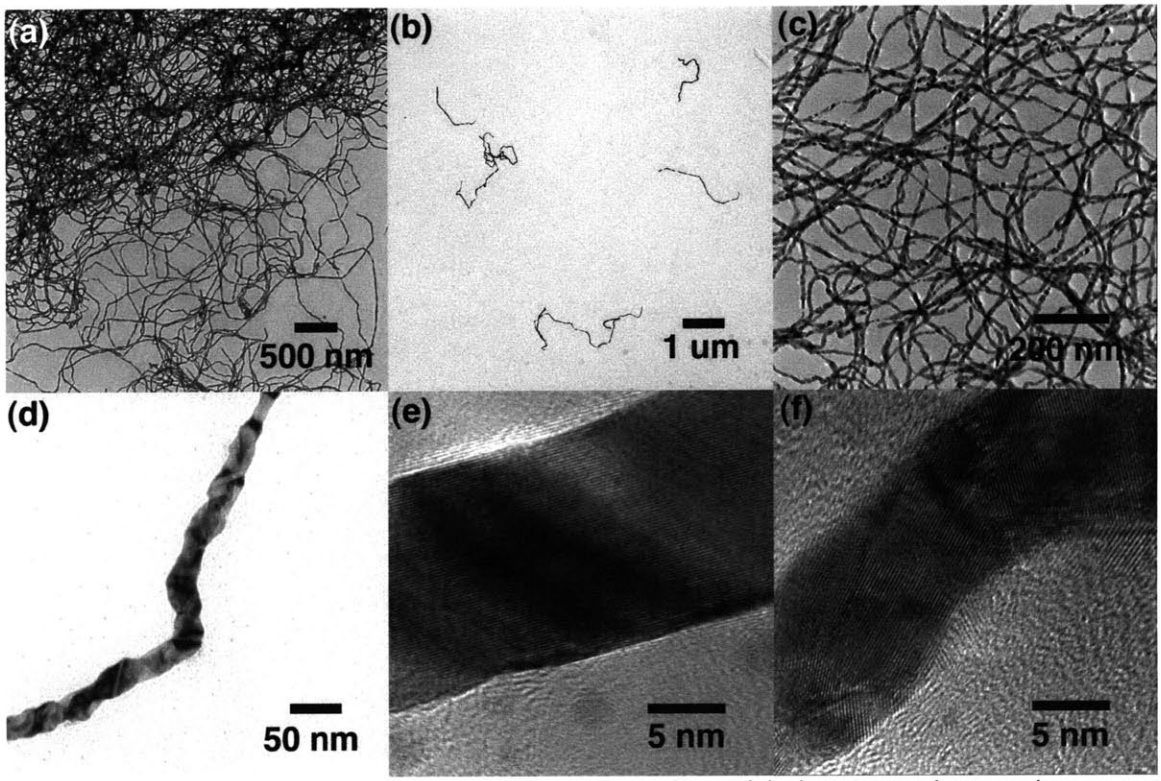

Figure 4.7 TEM images of $Au_{0.5}Ag_{0.5}$ alloy nanowires. (a) As-prepared nanowires were entangled each other but showed uniform diameter size along the nanowire length. (b) Individual nanowires were observed when the nanowire solution was diluted and sonicated. Any big nanoparticles were not visible from the nanowire solution without purification process. (c) Under high-resolution TEM with increased beam intensity, nanowires showed different contrasting color with brighter and darker regions as clearly shown in (d). The Au-Ag alloy nanowires are composed of smaller crystal domains with different crystallographic direction shown as dark and bright patterns. The lattice image clearly showed different crystal domains, single crystalline (e) and polycrystalline (f).

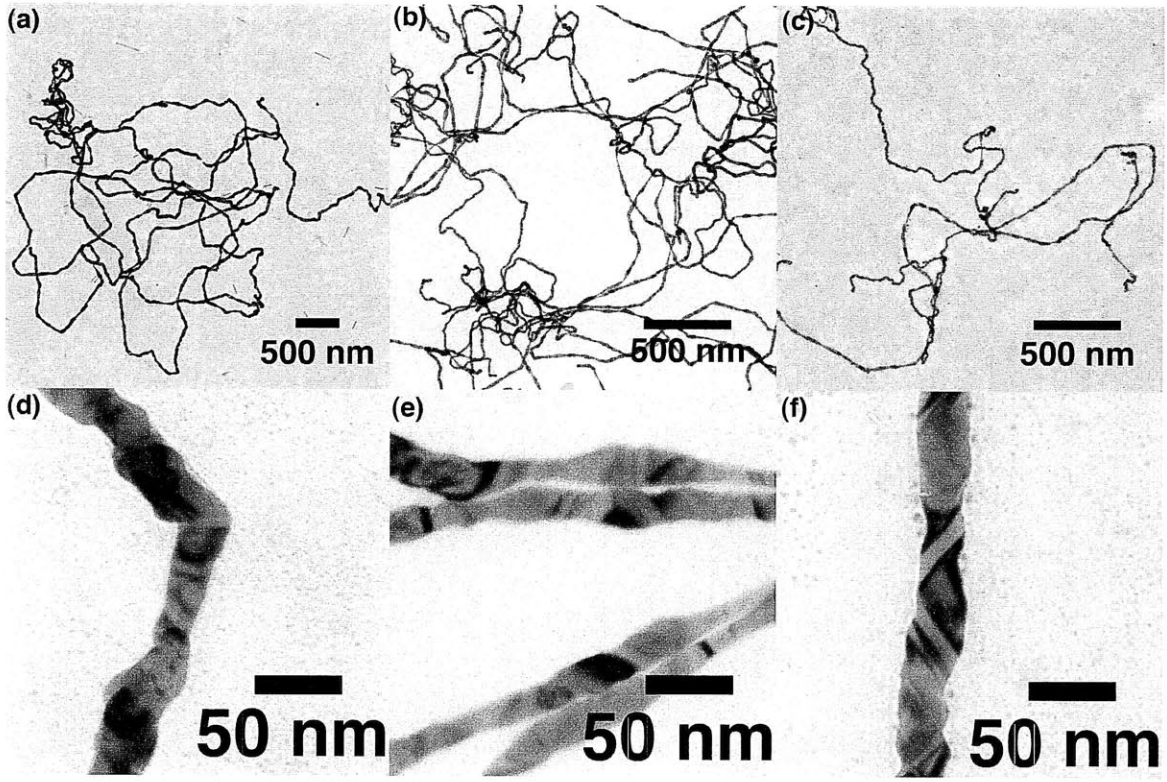

Figure 4.8 TEM images of Au_xAg_{1-x} alloy nanowires with various x. TEM images of (a) and (d): $Au_{0.8}Ag_{0.2}$, (b) and (e): $Au_{0.67}Ag_{0.33}$, and (c) and (f): $Au_{0.33}Ag_{0.67}$. All nanowires were imaged without purification.

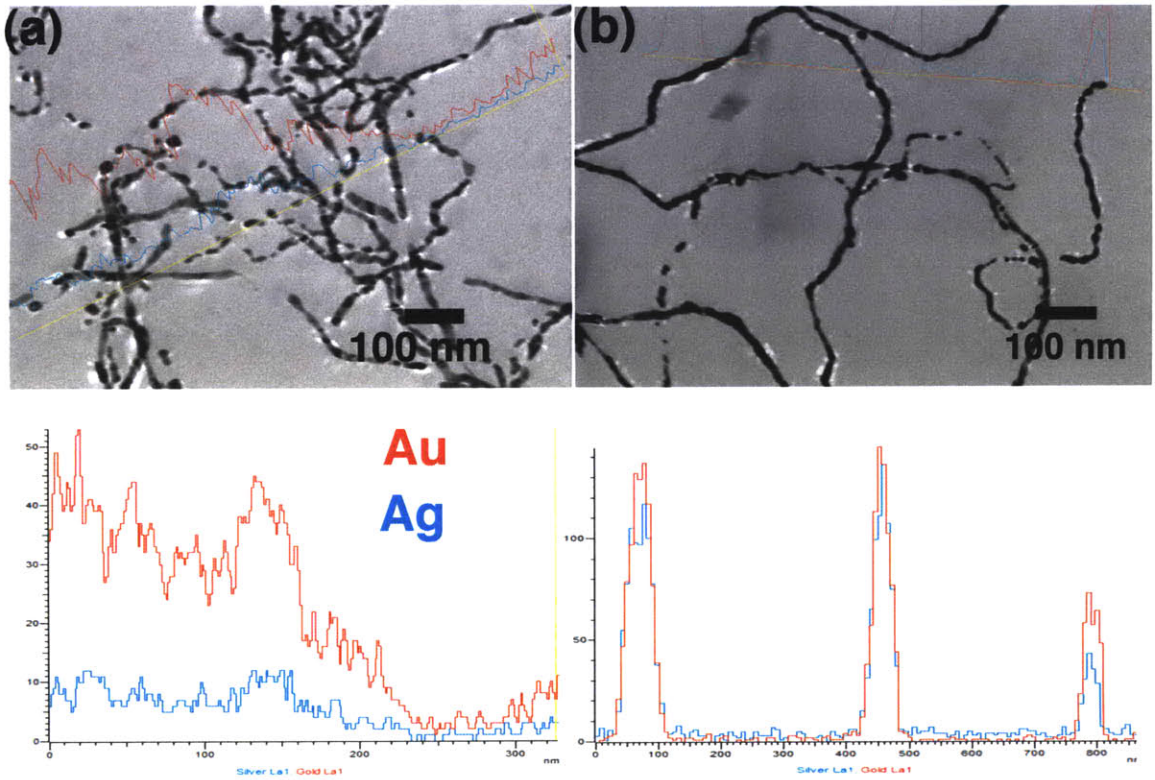

Figure 4.9 Au-Ag alloy nanowires prepared at different conditions. (a) The templating effect of p8#9 was significantly disrupted when excess Ag was introduced. The failure to make alloy nanowires with higher Ag contents (Au:Ag=1:4) appeared both in structures and compositions. (b) The advantage of p8#9 template was also confirmed from the synthesis of Au-Ag alloy with 1:1 ionic ratio of two atoms. Even though the elongated nanowire structure was given from the wild type M13 template, the ability to contain both atoms in homogeneous composition was far from that of p8#9. The final peak clearly showed different pattern from other two peaks.

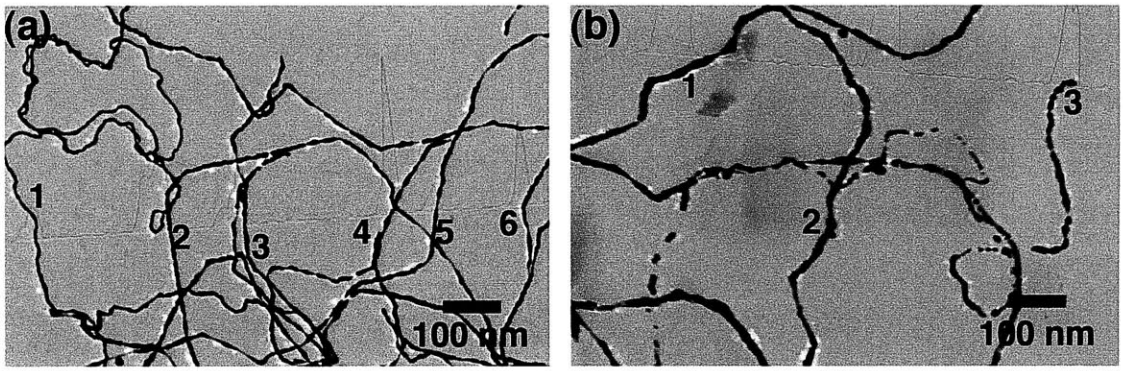

Template	P8#9		Wild type	
point	Au	Ag	Au	Ag
1	51.2	48.4	59	41
2	52.6	47.4	67	33
3	52.1	47.9	83	17
4	49.6	50.2		
5	50.5	49.5		
6	50.2	49.8		

Figure 4.10 Point analysis result of Au-Ag alloy nanowires from p8#9 and wild type M13 phage. (a) The point analysis of nanowires prepared from p8#9 showed consistent numbers of Au and Ag atomic percentage between the nanowires in one batch synthesis. (b) The atomic percentage of Au and Ag from the nanowires grown from wild type M13 phage showed random variation of two atoms.

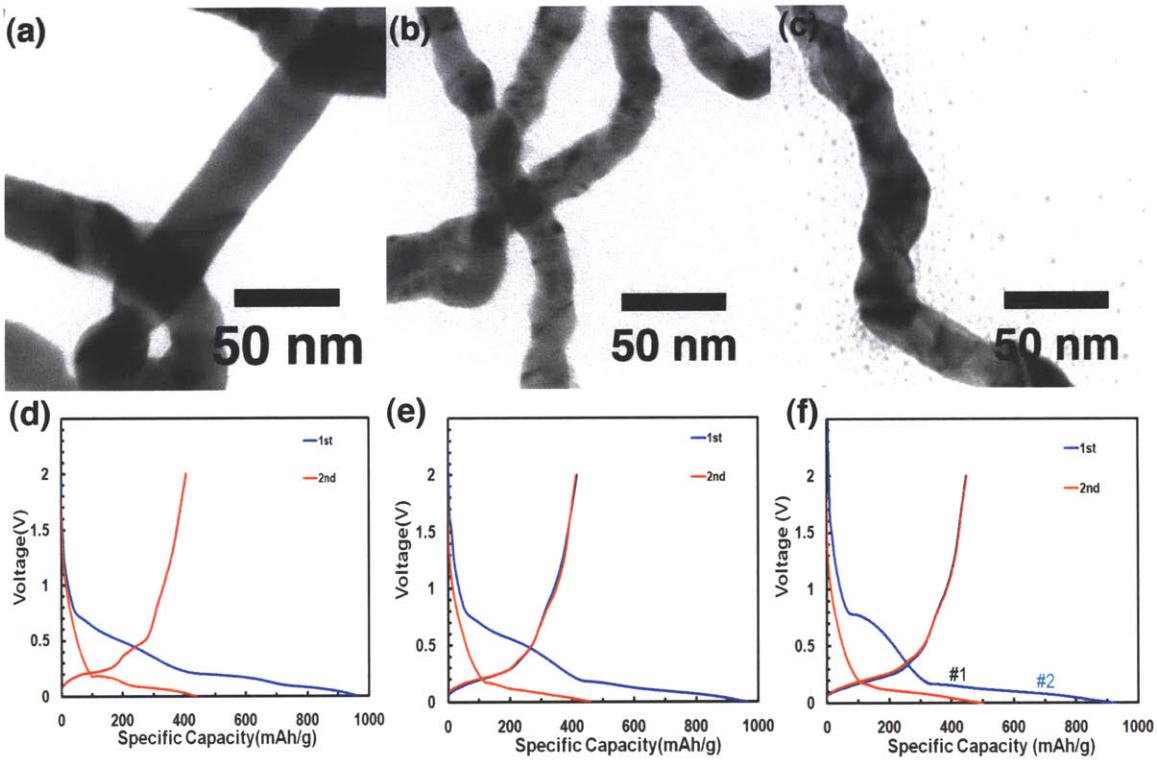

Figure 4.11 Representative TEM images of Au_xAg_{1-x} alloy nanowires and the potential profiles from the first two discharge/charge. The TEM images were taken from various Au-Ag alloy compositions: (a) $Au_{0.9}Ag_{0.1}$, (b) $Au_{0.67}Ag_{0.33}$, and (c) $Au_{0.5}Ag_{0.5}$. The first two discharge/charge curves were tested between potential 0 and 2.0 V with active material loading of (d): 5.11 mg/cm^2, (e): 4.47 mg/cm^2, and (f): 3.89 mg/cm^2.

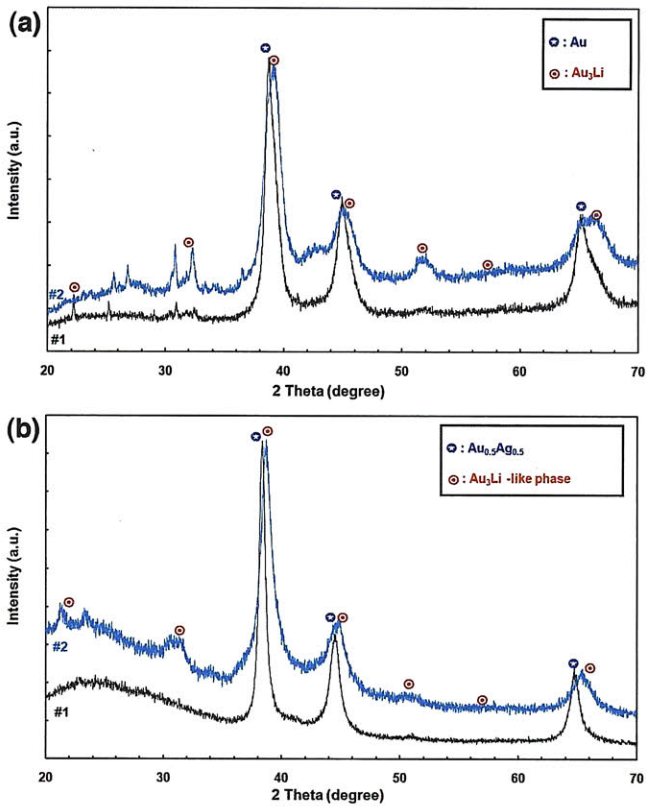

Figure 4.12 XRD evolutionary patterns at different stages of alloying process. Stage #1 is denoted at the potential profile of pure Au in Fig. 4.4(b) and stage #2 is available in Fig. 4.10 (f), the alloy nanowires with composition of $Au_{0.5}Ag_{0.5}$.

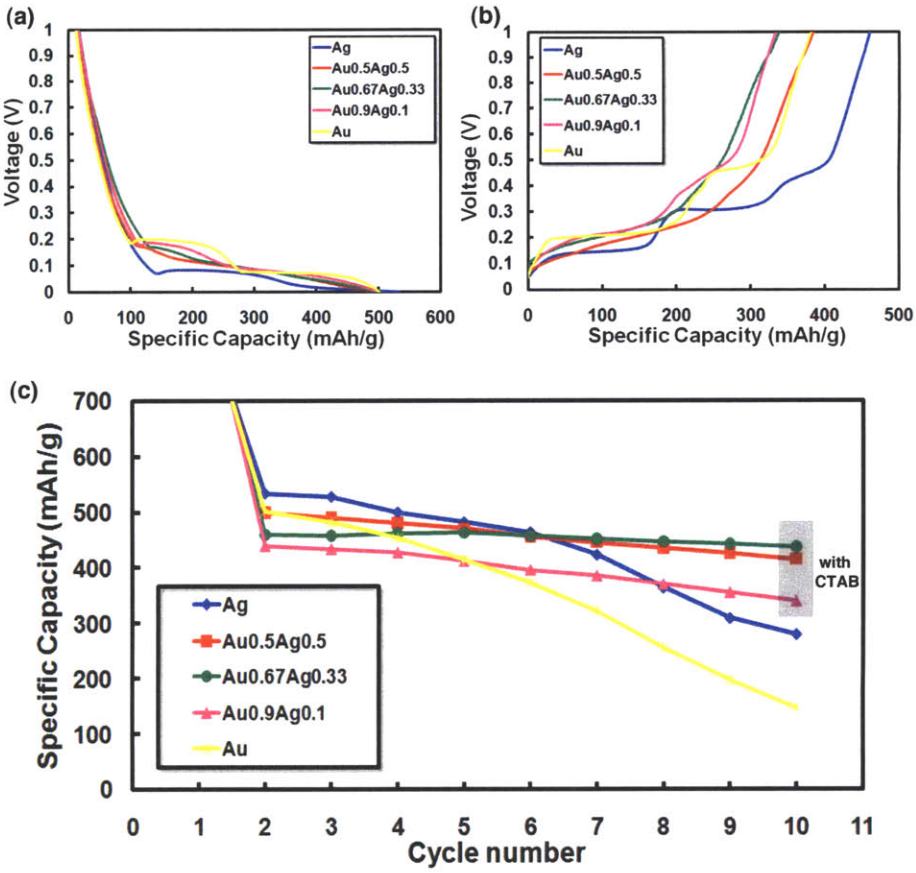

Figure 4.13 Electrochemical properties of Au_xAg_{1-x} alloy nanowires with various compositions (x: 0, 0.5, 0.67, 0.9, and 1). The second discharge (a) and charge (b) curves plotted together showing gradual shift in potential profiles between Au and Ag. (c) The capacity retention of each battery assemble distinguishes nanowires prepared with and without surfactant (CTAB).

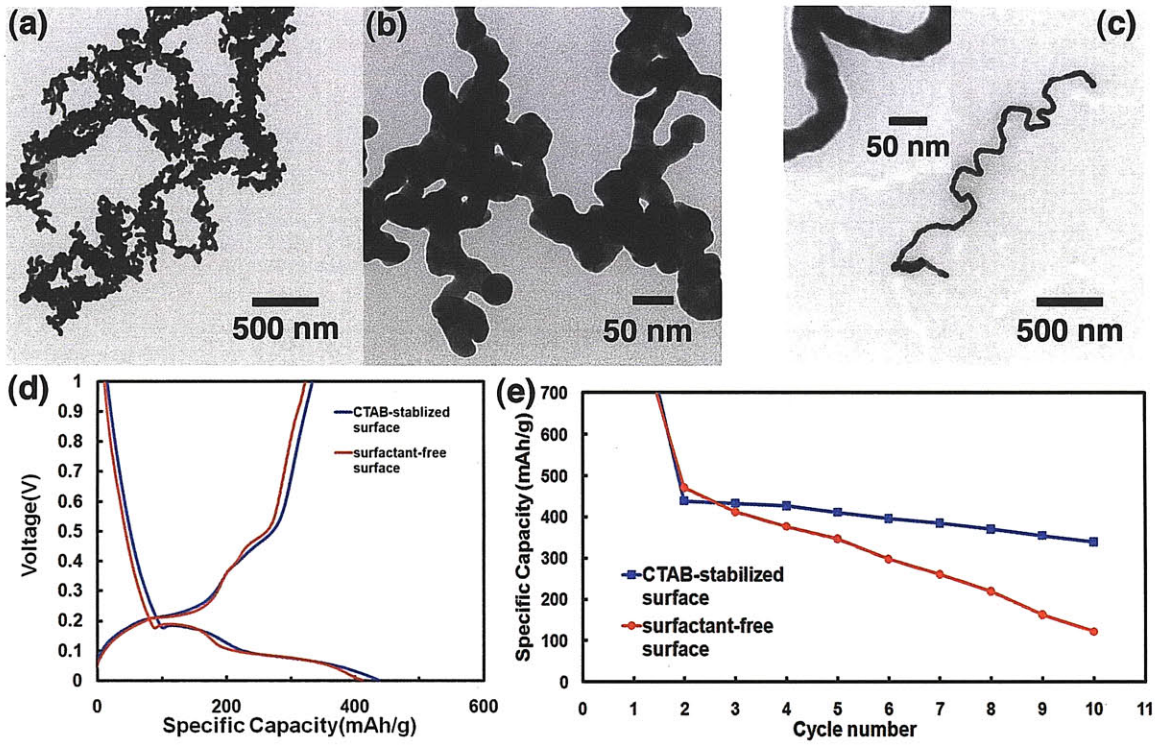

Figure 4.14 Surfactant effects on capacity retention of $Au_{0.9}Ag_{0.1}$ alloy nanowires. (a) Alloy nanowires prepared in the absence of surfactant resulted in interconnected bundle of nanowires with branches. (b) The $Au_{0.9}Ag_{0.1}$ alloy nanowires of free surfaces showed smoother surface than that of pure Au viral nanowires with free surfaces. (c) The alloy nanowires with same composition but with surfactant showed elongated nanowires without branches. (d) The first two discharge/charge curves both from free surfaced alloy nanowires and from surfactant stabilized ones are very similar in potential profiles. (d) The capacity retention over the first 10 cycle clearly distinguished the excellence of CTAB-stabilized nanowires over free surfaced ones.

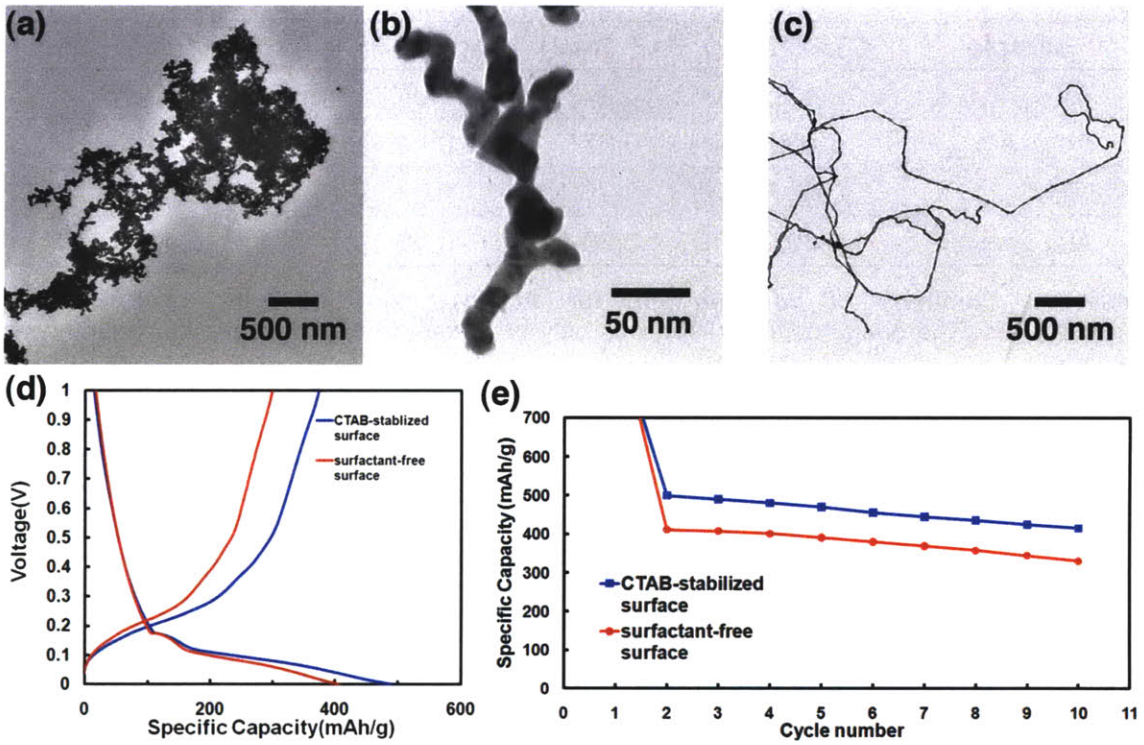

Figure 4.15 Comparisons of $Au_{0.5}Ag_{0.5}$ alloy nanowires with different surfaces. (a) The surfactant free $Au_{0.5}Ag_{0.5}$ alloy nanowires are also interconnected and not easily dispersed due to the absence of CTAB. (b) The detailed image of $Au_{0.5}Ag_{0.5}$ showed sharper angles than $Au_{0.9}Ag_{0.1}$ nanowires shown in Fig. 4.14(b). (c) $Au_{0.5}Ag_{0.5}$ alloy nanowires with CTAB exhibited more even surfaces. (d) The first and second discharge/charge curves were similar as expected from the result of $Au_{0.9}Ag_{0.1}$ nanowires. (e) The capacity retention of surfactant free $Au_{0.9}Ag_{0.1}$ alloy nanowires is close to nanowires with surfactant despite smaller capacity value about 20%.

sample	CTAB[M]	Au^{3+} [mM]	Ag^{+} [mM]	Ascorbic acid [mM]
$Au_{0.9}Ag_{0.1}$	0.412	0.27	0.04	0.82
$Au_{0.67}Ag_{0.33}$	0.409	0.27	0.14	0.41
$Au_{0.5}Ag_{0.5}$	0.404	0.27	0.27	0.41
$Au_{0.33}Ag_{0.67}$	0.401	0.20	0.40	0.41

Table 4-1 Summary of concentration for Au_xAg_{1-x} alloy nanowires with various compositions. The phage concentration was only differerent in $Au_{0.9}Ag_{0.1}$ but the volume was the same.

	Materials		Capacity [mAh/g]	
	composition	diameter	2^{nd} cycle	10^{th} cycle
surfactant free	Au	40 nm	502	146
	$Au_{0.9}Ag_{0.1}$	35 nm	471	122
	$Au_{0.5}Ag_{0.5}$	30 nm	411	330
	Ag	15 nm	534	280
CTAB stabilized	$Au_{0.9}Ag_{0.1}$	30 nm	439	340
	$Au_{0.67}Ag_{0.33}$	20 nm	459	437
	$Au_{0.5}Ag_{0.5}$	25 nm	499	415

Table 4-2 Summary of material information and the capacity values of Au_xAg_{1-x} nanowires. The second and tenth discharge capacities of Au, Ag, and Au-Ag alloy nanowires with various compositions.

Chapter 5. Synthesis of Au-Pt alloy nanowires and the electrocatalytic activity in O_2 reduction reaction

5-1. Introduction

One significant advantage of the Au-specific M13 phage as a nanowire template is that using this bio-template, new Au-based alloy nanowires can be synthesized where the alloy compositions are homogeneous and can be finely tuned by sequential addition of other noble metal salts (Pt^{4+}, Pd^{2+}, and Ag^{+}). As confirmed in previous chapter for the preparation of Au-Ag alloy nanowires, the p8#9 phage can serve as a versatile template for synthesizing other Au-based noble metal alloy nanowires, despite the fact that other noble metals do not have the same affinity to p8#9 phage as Au. The Au^{3+} ions have been found to be an essential component for the growth of nanowires on the p8#9 template with high yields, inasmuch no metal nanowires grown from surfactant-mediated p8#9 phage system without an Au component have been reproducibly synthesized so far. The addition of noble metal component to the Au nanowire synthesis enabled us to develop catalysts in various fields by utilizing the activities from elemental components independently or by exploiting any new properties combined[1]. Moreover, recent reports in Au not as an inert species but an active component in bi-metallic catalysts stimulating various reactions in various fields, evoked the preparation of Au-containing bi-metallic nanomaterials and their properties[2]. As examples, the catalytic and chemical properties of Au-based nanomaterials which can be tuned by controlling their diameter and their composition leading to catalytically interesting materials were reported recently[3,4,5,6].

Au, Ag, Pd, and Pt lie closely on periodic table implying similar atomic structure, properties, and even in sizes. The properties of each atom are summarized in Table 5-1. Au and Ag are very similar in size and electronic structure despite the big differences in atomic weight, so the X-ray diffraction pattern from pure Au and pure Ag nearly overlap.

The atomic weights of Pt and Au differ only about 1%, but the electronic structure of not-fully filled *d* orbital distinguishes Pt from other noble metals. As a result, unlike Au-Ag and Au-Pd systems that make homogeneous alloy solution over the entire mixing ranges, Au-Pt has very deep miscibility gap as shown in Fig. 5.1. The uptake of each atom at ambient temperature is limited to 17% in Au solution and 4% in Pt solution. However, the separation of two phases, especially in small nanoparticles, vanished and homogeneous alloy of Au-Pt has been prepared successfully[7]. These alloy nanoparticles exhibited systematic changes in lattice parameters, calculated from the X-ray diffraction data, well matched with Vegard's law. The critical size of stable Au-Pt alloy nanoparticle is not clearly reported yet, but nanoparticles less than 5 nm in diameter are considered to form true solid solution[8].

Here we report Au-Pt alloy nanowires with various compositions prepared from modified synthetic route discussed in previous chapter for the preparation of Au and Au-Ag alloy nanowires. This expandable synthesis technique for the preparation of various bi-metallic or multi-metallic nanowires stresses the importance of specific Au-binding M13 phage template for the preparation of Au-based alloy nanowires with homogeneous compositions, which can be further controlled without difficulties.

5-2. Synthesis of Au-Pt alloy nanowires

The noble metal nanowires were prepared by adding the precursors in a different incubation step, as depicted in Fig. 5.2. The synthesis of Au-Pt alloy nanowires was done by simple modification of the synthesis of Au nanowires in chapter 3. The addition of Pt^{4+} ions after the incubation of Au^{3+} ions followed by the addition of ascorbic acid as reducing agent yields Au-Pt alloy nanowires (scheme 1). The stoichiometric ratios of AA (Ascorbic Acid): Metal to reduce Au^{3+} ions and Pt^{4+} are 3:2 for Au and 5:1 for Pt. For the synthesis of Au nanowires, ascorbic acid with ratio of 3:2 [AA:Au] was added for the reaction, but for the reduction of Pt, excess ascorbic acid from 10:1 [AA:Pt] up to 20:1 [AA:Pt] was used. As a modified method, the metal precursors added to the phage solution simultaneously and reduced by ascorbic acid (scheme 2). After the addition of ascorbic acids, the incubated solution of both Au^{3+} and Pt^{4+} ions formed Au-Pt alloy nanowires with 5 to 40 atomic% of Pt. The two methods described in Fig. 5.2 resulted in slight differences in nanowires. For example, in the synthetic method from scheme 1, the introduction of Pt^{4+} ions after three hours of incubation of Au^{3+} ions to Au^{+} ions resulted Au-Pt alloy nanowires where the composition of Pt decreased about 15% from the same reactant concentration prepared from scheme 2. Detailed information about the synthetic method is described below.

Methods

Au-Pt nanowires were prepared by adding different amount of 10 mM Pt^{4+} ions into the solution for the synthesis of 40 nm Au nanowires in two different reaction paths.

Scheme 1: 15 mL of 0.6 M CTAB solution and 10 mL of p8#9 phage ($3.5x10^{10}$ pfu/mL) were mixed with slight vortexing. As in the synthesis of Au nanowires, 1 mL of 10 mM Au^{3+} ions was added to the phage solution and the whole mixture was incubated for three hours. Addition of ascorbic acid with 0.1 M concentration was added (1.3 mL or more) and various amounts (from 0.25 mL to 2 mL) of Pt^{4+} ions from hexachloroplatinic acid ($H_2PtCl_6 \cdot 6H_2O$) were added to the solution. The solution was kept at static condition for overnight to form Au-Pt alloy nanowires at various temperatures (50 and 80 °C).

Scheme 2: Phage and CTAB solution mixture was prepared as described in scheme 1. The Pt^{4+} ions and Au^{3+} ions were added together to the dispersion of p8#9 phage in CTAB solution, so the Au^{3+} ions reduced to Au^{+} in the existence of Pt^{4+} ions. After the addition of two metal salts, solution was incubated for two hours and then ascorbic acid was added. To reduce Au^{3+} and Pt^{4+} ions to metal nanowires, excess ascorbic acid than the stoichiometric molar ratio was added to the solution (up to six times of Au and ten times of Pt). Solution was gently mixed in a rocking machine for five minutes and then kept static condition. Reaction was done either room temperature or in the oven (50 °C or 80 °C). Nanowires after the overnight reaction washed with de-ionized water and ethanol with consecutive centrifugation.

5-3. Confirmation of Au-Pt alloy nanowires

Figure 5.3 represents TEM images of Au-Pt alloy nanowires formed at different reaction temperatures – room temperature (20-25 °C), 50 °C, and 80 °C. Even though the amount of Au^{3+} and Pt^{4+} added to the dispersion of p8#9 in CTAB solution was similar, the reaction yield was increased at higher temperature and the final products varied with the small temperature windows less than 60 °C. Nanowires prepared at room temperature have smoother surfaces as shown in inset image of Fig. 5.3(a). This relatively flat surface is not observed when the reaction temperature increased to 50 °C, and the new surface, prepared at higher temperature, is composed of smaller nanoparticles less than 5 nm in diameter. The inset in Fig. 5.3(b) is a representative image of secondary structure of Au-Pt alloy nanowires prepared at 50 °C. The smaller nanoparticles of Au-Pt alloy nanowires prepared at 50 °C can be explained from the theory of overcoming the miscibility gap of Au and Pt when the domain size gets smaller.

When the reaction temperature was increased to 80 °C, the homogeneity of synthesized nanowires was regressed and as a result, Au-rich and Pt-rich nanowires were produced from one batch synthesis. The nanowires shown in Fig. 5.3 (c) exhibited reduced contrast compared with other nanowires in (a), (b), and (d). As already shown as inset images both on (c) and (d), the line scanning result confirmed the different composition of Au and Pt on each sample even though the quantitative analysis from the line scanning is limited (the smaller nanoparticle showed higher Pt content than Au more than 10 times) but the crystalline nanowires with higher contrast contained more Au than Pt. However, we confirmed that considerable amount of the Pt was structured in Fig.

5.3(d). The two samples could be separated by centrifugation due to the difference in weight of nanowires.

Therefore, the reaction temperature, 50 °C, for the preparation of Au-Pt alloy nanowires was chosen because of the improved homogeneity over that 80 °C and the better yield than room temperature. The nanowires prepared at 50 °C already resulted in very fine nanoparticles along the M13 phage structure to overcome the miscibility gap. The detailed structural information of Au-Pt alloy nanowires is available in Fig. 5.4. The flower-like ends of Au-Pt alloy nanowires also have the same composition as that of the main body of the nanowires (Fig. 5.4(a) and (b)). The flower-like shape of Au-Pt alloy nanoparticles was reported before in the synthesis from polyamidoamine dendrimer-assisted electro-deposition, but the actual shape of the nanoparticles are close to the main body of nanowires in that they are composed of small nanoparticles[9]. The flower-like ends of the Au-Pt alloy nanowires are similar in shape with Au-Pt nano-dendrite synthesized from Ti-catalyzed hydrothermal reaction process[10]. Analytical TEM analysis also confirmed the uniform distribution of Au and Pt atoms over the nanowire structure as shown in Fig. 5.4 (d)-(f). The normal TEM imaging was done on an end of discrete nanowire with a flower-like end (d). The selective mapping provided the position of Au (e) and Pt (f) atoms respectively. There was no evidence of phase separation between the two atoms.

EDX analysis confirmed the homogeneous compositions of two atoms in the alloy nanowires, which matched the ICP-OES analysis of the final reaction products. To examine the structural change from the composition of Pt in Au-Pt alloy nanowires, X-ray diffraction of two different Au-Pt alloy nanowires was investigated. The XRD peaks

of the Au-Pt alloy nanowires fell between the characteristic peaks of Au and Pt in JCPDS data from Au-Pt alloy nanowires with compositions of 13 (Fig. 5.5(a)) and 40 (Fig. 5.5(b)) atomic% Pt. The 2θ values observed from the two different samples, plotted with pure Au and Pt as a reference, shifted in the direction of Pt as the composition of Pt increased[11]. This is also supported by the broadening of peaks the nanowires of 40% Pt composition compared to that of 13% Pt nanowires observed in the XRD peaks shown in Fig. 5.5(b). This observation is also supported by the TEM image in a later section.

5-4. Control of the composition of Au-Pt alloy nanowires

Increasing the concentration of Pt^{4+} resulted in Au-Pt alloy nanowires with higher Pt contents. The compositions of alloy nanowires were easily controlled by changing the amount of metal precursors, but the general morphologies remained largely unchanged at a given condition: the primary particle size less than 5 nm and the secondary dimension of diameter size larger than 30 nm. The TEM images of Au-Pt alloy nanowires with different ratios are available in Fig. 5.6. To better understand the detailed structure, images were taken both from the flower-like end and the main body of nanowires. The final compositions of Au-Pt alloy nanowires were slightly affected by the way of preparation of nanowires as shown in Fig. 5.2 as schematics, however, nanowires with higher Pt contents were obtained when more Pt^{4+} was added.

One interesting feature is that increasing Pt concentration resulted in Au-Pt alloy nanowires with smaller primary particle sizes in nanowires, in other words, the increased roughness of the surfaces. As we can see by comparing the nanowire image (c) and (h), the nanowire in (c) is similar to Au nanowires with undulated surfaces, but the nanowire in (h) looks like a dendrite structure of smaller particles with increased roughness. This could be explained from the miscibility gap in Au-Pt referred in introduction. The nanowire shown in (c) contains about 12% of Pt, which is within the boundary of single-phase region of Au and Pt, but the nanowires in (h) contains 40% of Pt, which is far beyond the limit of miscibility of Pt in Au. The formation of smaller nanoparticles in nanowires with higher concentration of Pt could indirectly support the homogeneity of nanowires without phase segregation[2,11]. The nanowires shown in Fig. 5.6 are all prepared using the method based on scheme 1 in Fig. 5.2. The information of the

concentration both in precursors and in final nanowires shown in Fig. 5.6 is available in Table 5.2.

For Au-Ag alloy nanowires, the composition of the final product reflected the relative amounts of Au and Ag added to the synthesis, but for alloy nanowires incorporating Pt added right after the addition of ascorbic acids, less than 30 % of the precursor introduced into the reaction were integrated into the alloy nanowires under the assumption of 100% Au conversion. The conversion efficiency of Au^{3+} in the Au-Pt alloy nanowires was confirmed higher than 95% from ICP-OES in synthesis with phage concentration of $7x10^{10}$ pfu/mL, but was lower when the phage concentration was decreased.

The high affinity between Au^{3+} ions and p8#9 template and the weaker interaction between Pt^{4+} and CTAB molecules occasionally produced two different morphologies within one sample as shown in Fig 5.3(c) and (d). Reducing the concentration of p8#9 templates decreased the conversion yield of Au^{3+} ions to around 70%, but produced Au-Pt alloy nanowires with better reproducibility. The Au-Pt alloy nanowires with various ratios of Au:Pt, from 9:1 to 2:1 were prepared from lower phage concentration and reduced metal ions from the way described in scheme 2. Table 5-3 summarized the detail concentration of reactants.

5-5. Electrochemical analysis of Au-Pt alloy nanowires

As prepared Au-Pt alloy nanowires were dispersed in a mixture of CTAB and TBS buffer, so the nanowires were washed with de-ionized water for three times. After the washing step, the nanowires in de-ionized water precipitated in the bottom but became a homogeneous solution after sonication for a short time. We confirmed the existence of CTAB layer on the surface of nanowires from the discrete nanowire images from TEM and weight differences in TGA result. The working electrode was prepared by casting 20 μL solution of the Au-Pt alloy nanowire suspension in Milli-Q water onto a glassy carbon disk electrode (0.196 cm^2 geometrical surface area) substrate at a Au-Pt nanowire loading of several μg. All the electrodes have very comparable loadings of ~20 $\mu g/cm^2_{disk}$. After evaporating the solvent, the deposited Au-Pt nanowires thin film was covered with 15 μL of 0.05 wt% Nafion® solution to attach the Au-Pt nanowires to the glassy carbon disk. The electrode was then dried under air atmosphere with a cover glass and transferred to the electrochemical cell in Ar saturated 0.1 M KOH electrolyte.

The electrochemical studies were carried out in a three-electrode cell using a saturated calomel electrode (SCE) as the reference and a platinum wire as the counter electrode. The electrochemical measurements were conducted by using a voltamaster potentiostat (Radiometer analytical, France). All potentials, however, are referenced to the reversible hydrogen electrode (RHE) potential, calibrated via the hydrogen oxidation/reduction reaction on a pure Pt rotating disk electrode in the same cell and electrolyte at the same temperature. Oxygen reduction was measured in O_2 saturated 0.1 M KOH at a potential scan rate of 10 mV/s, after bubbling O_2 for 25 min. In the rotating

disk electrode (RDE) experiments, the working electrode was rotated in the range of 100 - 2500 rpm using a PINE Instruments AFMSRCE rotator.

5-6. Electrocatalytic activity of Au-Pt alloy nanowires for O_2 reduction reaction

One of the major challenges for utilization of Au catalysts in low-temperature fuel cells is the inferior activity of Au to Pt, which is expensive and supply-limited but the most active catalyst for O_2 reduction. Therefore, we examined the electro-catalytic activity of Au-Pt alloy nanowires with different ratios (i.e. 9:1, 4:1 and 2:1) for O_2 reduction in O_2-saturated 0.1 M KOH using rotating disk electrode (RDE). As shown in Fig. 5.7(a), appreciable voltammetric currents were detected on Au-Pt nanowires with CTAB organic surfactants as described above, suggesting ready access of oxygen to the nanowire surface. To compare the ratio-dependent catalytic activity, we combined ORR curves at the same rotation speed 1600 rpm for the 9:1, 4:1 and 2:1 Au-Pt nanowires together (Fig. 5.7(a)). The current is normalized by the weight of total metal nanowires. The ORR onset potentials for 2:1 ratio of Au-Pt nanowires had positive shifts to ~0.95 V (vs. RHE), suggesting considerably higher ORR electrocatalytic activity of 2:1 ratio than that of nanowires with 9:1 and 4:1 ratios. The ORR electrocatalytic activity of Au-Pt nanowires (2:1) normalized to metal weight is remarkably high, which is comparable to that of conventional supported Pt/C catalyst reported previously[12].

In order to obtain insight into the reaction pathway for O_2 reduction, viz., whether the main reaction product is water ($4e^-$ reduction) or hydrogen peroxide ($2e^-$ reduction), a Koutecky-Levich analysis was done[13]. The Koutecky-Levich plots (i^{-1} vs $\omega^{-1/2}$) at four different potentials 0.85 V, 0.75 V, 0.65 V and 0.55 V vs. RHE shows that rotated disk electrode currents change linearly with square root of rotation rate ($\omega^{1/2}$) (Fig. 6c):

$$\frac{1}{i} = \frac{1}{i_k} + \frac{1}{i_d} = \frac{1}{nFAkC_{O_2}^b} + \frac{1}{0.62nFAD_{O_2}^{2/3}\upsilon^{-1/6}C_{O_2}^b\omega^{1/2}} \quad (1)$$

where i is the measured current, n is the number of electrons in the O_2 reduction reaction, F is the Faraday constant, A is the geometric electrode area, D is the diffusion coefficient of O_2 in solution, υ is the kinematic viscosity of the electrolyte, c_o is the O_2 solubility in the electrolyte, and ω is the rotation rate.[14]

Furthermore, equation (1) can be simply formed by equation (2).

$$\frac{1}{i} = \frac{1}{i_k} + \frac{1}{Bc_{O_2}^b\omega^{1/2}} \quad (2)$$

Kinetic currents for O_2 reduction, i_k, were calculated based on the equation (1); having these Bc_0 values (Fig. 6(b), Equation 2), kinetic currents [15] as a function of potential was calculated from equation 3.

$$i_k = \frac{i \times i_d}{i_d - i} \quad (3)$$

In addition, the diffusion component can be simplified and expressed by the Koutecky-Levich equation, $i_d = Bc_0\omega^{1/2}$. A slope defined by Bc_0, where $B = 0.62nFD^{2/3}\upsilon^{-1/6}$. The number of electrons (n) transferred can be calculated by $n = (B/0.62F)\, D^{-2/3}\upsilon^{1/6}$.

From the analysis, the average number of transferred electrons for O_2 reduction on 2:1 ratio of Au-Pt nanowires is calculated to be 3.7, corresponding to 85% of O_2 directly converted to water. Thus, the O_2 reduction on the 2:1 ratio of Au-Pt nanowires approaches the desired $4e^-$ process despite its high Au content. The electrocatalytic activity of the CTAB capped Au-Pt alloy nanowires based on metal weight could also be enhanced by removing surfactant layer to increase active surface sites on the alloy nanowires. An important figure-of-merit for commercially viable fuel cell catalysts is the

O_2 reduction current which can be produced per weight of noble metal, and is commonly expressed as the so-called mass-activity measured at 0.9 V vs. RHE, $i_{m(0.9\ V)}$ (in units of mA/mg_{metal}). The mass activity 23 $mA/mg_{Au\text{-}Pt}$ of the Au-Pt (2:1) nanowires is quite comparable to that of a commercial 10 wt% Pt/C catalyst (35 mA/mg_{Pt}), as shown in the Figure 6(d). If evaluated on a platinum weight basis, i.e., in terms of mA/mg_{Pt}, the mass activity of the Au-Pt nanowires is actually 1.8 times larger than that of Pt[16] (Fig. 5.7 (d) inset).

5-7. Synthesis of Au-Pd-Pt tri-metallic alloy nanowires.

As one of the expansion of the synthetic method for the preparation of noble metal alloy nanowires, the combination of Au and Pd was also tested. The combination of Au and Pd appeared uncomplicated at first based on many reports about the bi-metallic cluster of Au-Pd accomplished in theoretically and experimentally[16,17,18]. The phase diagram of Au-Pd system forms a continuous miscible solution at any range of the composition like in Au-Ag system[17]. The incubation of Pd^{2+} ions with Au^{3+} results in small nanoparticles with sharp edges showing templating effect of p8#9 as shown in Fig. 5.8 (a-c), but the nanoparticles were random in size and shape and any continuous wires were not observed. This structure is very similar with the Au-Pd alloy nanoparticles decorated on 1-dimensional silicon nanowires reported before[18]. The absence of strong absorption peak from the UV-Vis absorption data suggests a lower possibility of formation pure Au nanoparticles. However, despite the favorable mixing of Au and Pd expected from thermodynamic point of view, the formation of Au-Pd alloy nanowires with continuous shape and homogeneous composition has not successfully been done so far.

The addition of Pt^{4+} precursor into the dispersion of phage with Pd^{2+} and Au^{3+} produced tri-metallic alloy nanowires (Fig. 5.8(d-f)). As seen from the phase diagram of Au, Pd, and Pt at higher temperature shown in Fig. 5.9, the three metals can form tri-metallic solution at ranges colored in blue[19]. The area of solid solution was reduced when the temperature is lowered to 800 °C (Fig. 5.9(a)), which is much higher than the reaction temperature chosen here. The two-phase region colored in white could be speculated to be much wider at temperature below 100 °C, the actual temperature of the synthesis, so

the segregation of two-phase with different atomic ratios was expected. However, as shown in Fig. 5.10, the line scanning and elemental mapping results shows the three metals are uniformly contained within the nanowire structure, and point analysis confirmed the atomic composition of Au: Pd: Pt to be 5:3:2 from a precursor composition of 1: 1: 1. This suggests better incorporation of Pd than Pt into the nanowires from the bio-mineralization of p8#9. One interesting feature of the result is that the atomic composition of 5:3:2 is situated in white region, the two-phase region, in phase diagram at 800 °C. The vanishing miscibility gap in smaller nanoparticles in Au-Pt alloy nanoparticle system could also explain this exceptional composition of three metals, which was originally considered to be two-phase. The individual nanoparticle size imaged in Fig. 5.8(f) is as small as that of Au-Pt nanoparticles covering the Au-Pt nanowires in Fig. 5.3(b).

Methods

The tri-metallic nanowires were prepared by adding the three different metal ions into the mixture of p8#9 phage and the CTAB. Sequential addition of Pt^{4+} ions followed by Pd^{2+} ions to Au^{3+} ion-templated p8#9 phage resulted tri-metallic alloy nanowires with homogeneous composition of three different metals. Here, we also added excess ascorbic acid (three times of Au, ten times of Pt, and five times of Pd). The solution was also kept in oven (50 and 80 °C). 10 mL of p8#9 phage with concentration of $3.5x10^{10}$ pfu/mL was mixed with 25 mL of 0.1 M CTAB solution. 10 mM-concentrated metal precursors with 5 mL volume was added to the phage dispersion and incubated for one hour. After the incubation, metal precursors were reduced by 2.5 mL of 0.1 M ascorbic acid. The resultant solution was then kept at static conditions in the oven.

5-8. Synthesis of Au-Pt alloy nanowires with free surfaces.

Even though the increasing concentration of Pt^{4+} produced Au-Pt alloy nanowires with higher Pt content in the surfactant mediated system, there exists an upper limit of Pt content as 40% atomic concentration of Pt. Undoubtedly, the specific Au binding of p8#9 could not guarantee preferable binding of p8#9 with other noble metals such as Ag, Pd, and Pt. However, considering the maximum limit of 67% Ag in Au-Ag alloy nanowires, this reduced number of 40% in Au-Pt alloy nanowires could result from the different ability to interact with surfactant molecules. The reduced interaction between Pt and CTAB is sometime utilized for the preparation of Pt catalyst to increase the number of available surface sites of Pt nanoparticles, which could be blocked from the strong interaction between the surfactant and Pt[20]. Therefore, we might increase the Pt content in synthesis of Au-Pt alloy nanowires without CTAB.

We already confirmed the homogeneity of the composition in Au-Ag alloy nanowires with free surfaces to examine the surface-stabilization effects on capacity retention in Chapter 4. Regardless the surface morphologies came from the absence of surfactant molecules, Au-Ag alloy nanowires with free surfaces (without surfactant) exhibited materials properties agreed with the compositions of Au and Ag. Figure 5.11 represents TEM images of Au-Pt alloy nanowires with free surfaces prepared from the scheme 2 in Fig. 5.2. To optimize template concentration in the synthesis of a surfactant free system, p8#9 with various concentrations was added to the synthetic reactions. P8#9 phage after amplification was diluted with 1X TBS buffer into three different set with concentration of $4x10^9$ pfu/mL, $3.5x10^{10}$ pfu/mL, and $1.5x10^{11}$ pfu/mL (The phage solutions were further diluted into de-ionized water, and Au^{3+} and Pt^{4+} ions were added

together.). The solution was incubated for half hour and then reduced with the addition of ascorbic acid. The solutions were kept at 50 °C in the oven overnight. The final concentration of p8#9 in the solution was calculated to be $1.1x10^9$, $9.4x10^9$, and $4.0x10^{10}$ pfu/mL respectively. As shown in Fig. 5.11, nanowires prepared from lowest phage concentration appeared thicker than others, however, all clear different features observed are seen in Fig. 5.11 (b) and (c).

By changing the relative concentration of Pt^{4+}, Au-Pt alloy nanowires with various compositions were prepared as shown in Fig. 5.12. The morphologies and yields varied with reaction temperature and composition of Pt. The alloy nanowires with 10% atomic Pt exhibited undulated surfaces when they were prepared at room temperature (Fig. 5.12(a)) but the yield of nanowires was lower than 40%. Increasing the temperature to 50 °C significantly increased the yield and the surface roughness (Fig. 5.12(b)). As we already confirmed in Au-Pt alloy nanowires and Au-Pd-Pt alloy nanowires from surfactant-mediated synthesis, nanowires composed of small nanoparticles were observed when Pt composition was increased. Au-Pt alloy nanowires with 50% atomic Pt prepared at room temperature (Fig. 5.12(c)) have enhanced uniformity in diameter size (the secondary structure of nanowire) than nanowires prepared at 50 °C (Fig. 5.12(d)). The reduced roughness of surfaces in nanowires prepared at low temperature was observed in synthesis with different Pt concentrations.

5-9. Synthesis of pure Pt nanowires from p8#9

Even though the template p8#9 has specific binding against Au, it also appeared to have affinity to Pt in moderate level. When the concentration of Pt was further increased to 100%, pure Pt without Au, Pt nanowires from various conditions were prepared as shown in Fig. 5.13. When the Pt nanowires were synthesized from the typical CTAB-mediated biomineralization from stepwise incubation and reduction of Pt^{4+}, Pt nanowires mixed with nanoparticles were prepared as shown in Fig. 5.13(a). The increased population of Pt nanoparticles was expected due to the weaker interaction between Pt^{4+} and p8#9. Moreover, the reduced tendency for mixing Pt with CTAB significantly diminished the yield of nanowires. To rule out the CTAB effect, Pt nanowires of free surfaces were also prepared as shown in Fig. 5.13(b). By eliminating the barrier between Pt^{4+} and p8#9, templating of Pt onto the surface of p8#9 was enhanced, thus very few Pt nanoparticles were observed. However, the yield, less than 30%, was not enough to apply this synthetic method in applications. To increase the conversion of Pt^{4+}, sodium borohydride ($NaBH_4$), a strong reducing agent, was added to the solution of p8#9 templated with Pt^{4+} ions (Fig. 5.13(c)). While the yield of nanowires prepared from Pt^{4+} ions was increased up to 95%, the increased reducing power of sodium borohydride strikingly changed the morphology of Pt nanowires. Bio-mineralization of Pt occurred on p8#9 templates, but from the unconstrained reaction of Pt, the as-prepared Pt nanowires were entangled with each other and the individual particles have sharp edges in random directions. The synthetic method of Pt nanowires shown in Fig. 5.13(b) was further modified to increase the yield of nanowires. When the temperature was increased to 50 °C, the yield of nanowires exceeded 60% and the

diameters of nanowires also thickened, but the with the increased yield, the number of free particles also increased (Fig. 5.13(d)).

P8#9 can also serve as template for the preparation of pure Pt nanowires. While the structural uniformity of nanowires was acquired from the synthesis of Pt nanowires with free surfaces, the yield still needs to be improved. M13 phage with specific Pt binding could remarkably increase the yield and improve the morphologies as confirmed in synthesis of various Au nanowires from the p8#9, the specific Au binding phage.

5-10. Conclusion

P8#9 phage was applied to synthesis of Au-Pt alloy nanowires at various conditions. Even though the affinity of p8#9 against Pt^{4+} was much lower than that of Au and Au ions, p8#9 served as an excellent template for the preparation of Au-Pt alloy nanowires with uniform composition along the nanowire length by cooperating binding of Pt^{4+} ions. In spite of the wide miscibility gap between Au and Pt, the alloy nanowires with various compositions were successfully prepared by forming small alloy nanoparticles along p8#9. The alloy nanowires exhibited crystal structure in between pure Au and pure Pt in a XRD crystallographic study, which also showed compositional dependence. The compositional dependency of Au-Pt alloy nanowires were also confirmed in an electrochemical study of oxygen reduction reaction on the surface of Au-Pt alloy nanowires with various alloy compositions. The Au-Pt alloy nanowires with Au: Pt atomic ratio of 2:1 exhibited Pt-like reaction pathway both in kinetic and thermodynamic points despite the high content of Au atoms. The addition of Pd^{2+} resulted in tri-metallic nanowires composed of smaller nanoparticles as their primary structure in a similar way of Au-Pt nanowires.

Removal of the CTAB surfactant in the synthesis of Au-Pt alloy nanowires enabled us to increase Pt content up to 60%, and the structural change was also confirmed from TEM. The morphology of nanowires was controlled via composition of Pt and the reaction temperatures. Pt nanowires could also be produced from p8#9 phage, but a high yield of optimized nanowires has not yet been achieved.

5-11. References

1 Chen, M. S., Kumar, D., Yi, C. W. & Goodman, D. W. The promotional effect of gold in catalysis by palladium-gold. *Science* **310**, 291-293 (2005).

2 Bond, G. C. The Electronic Structure of Platinum-Gold Alloy Particles: Better catalysts for selective oxidations. *Platinum Metals Review* **51**, 63-68 (2007).

3 Cheng, D. J., Wang, W. C., Huang, S. P. & Cao, D. P. Atomistic modeling of multishell onion-ring bimetallic nanowires and clusters. *J. Phys. Chem. C* **112**, 4855-4860 (2008).

4 Lim, B. *et al.* Pd-Pt Bimetallic Nanodendrites with High Activity for Oxygen Reduction. *Science* **324**, 1302-1305 (2009).

5 Zhang, J., Sasaki, K., Sutter, E. & Adzic, R. R. Stabilization of platinum oxygen-reduction electrocatalysts using gold clusters. *Science* **315**, 220-222 (2007).

6 Davis, D. J., Kyriakou, G. & Lambert, R. M. Uptake of n-Hexane, 1-Butene, and Toluene by Au/Pt Bimetallic Surfaces: A Tool for Selective Sensing of Hydrocarbons under High-Vacuum Conditions. *J. Phys. Chem. B* **110**, 11958-11961 (2006).

7 Xu, J., Zhao, T., Liang, Z. & Zhu, L. Facile Preparation of AuPt Alloy Nanoparticles from Organometallic Complex Precursor. *Chemistry of Materials* **20**, 1688-1690 (2008).

8 Vazquez-Zavala, A., Garcia-Gomez, J. & Gomez-Cortes, A. Study of the structure and selectivity of Pt-Au catalysts supported on Al2O3, TiO2, and SiO2. *Appl. Surf. Sci.* **167**, 177-183 (2000).

9 Qian, L. & Yang, X. Polyamidoamine Dendrimers-Assisted Electrodeposition of Gold-Platinum Bimetallic Nanoflowers. *J. Phys. Chem. B* **110**, 16672-16678 (2006).

10 Wang, J., Thomas, D. F. & Chen, A. Direct growth of novel alloyed PtAu nanodendrites. *Chem. Commun.*, 5010-5012 (2008).

11 Habrioux, A. *et al.* Structural and electrochemical studies of Au-Pt nanoalloys. *Phys. Chem. Chem. Phys.* **11**, 3573-3579 (2009).

12 Lima, F. H. B. *et al.* Catalytic Activity d-Band Center Correlation for the O2 Reduction Reaction on Platinum in Alkaline Solutions. *J. Phys. Chem. C* **111**, 404-410 (2006).

13 Bard, A. J., Faulkner, L.R. *Electrochemical Methods Fundamentals and Applications*. (Wiley).

14 Strbac, S. & Adzic, R. R. The influence of OH- chemisorption on the catalytic properties of gold single crystal surfaces for oxygen reduction in alkaline solutions. *J. Electroanal. Chem.* **403**, 169-181 (1996).

15 Nikoobakht, B. & El-Sayed, M. A. Preparation and Growth Mechanism of Gold Nanorods (NRs) Using Seed-Mediated Growth Method. *Chem. Mater.* **15**, 1957-1962 (2003).

16 M. Piana, S. C., H. A. Gasteiger. *ECS Transactions* **16**, 2045 (2008).

17 *Phase Diagrams*. 2nd ed edn, Vol. 1 (ASM International, 1992).

18 Zhang, P., Zhou, X., Tang, Y. & Sham, T. K. Organosulfur-Functionalized Au, Pd, and Au-Pd Nanoparticles on 1D Silicon Nanowire Substrates: Preparation and XAFS Studies. *Langmuir* **21**, 8502-8508 (2005).

[19] *Au-Pd-Pt Phase Diagram (1990 Raynor G.V.)*, <http://www.asminternational.org.libproxy.mit.edu/asmenterprise/APD/ViewAPD.aspx?id=977618> (

[20] Lee, H. *et al.* Morphological Control of Catalytically Active Platinum Nanocrystals13. *Angew. Chem. Int. Ed.* **45**, 7824-7828 (2006).

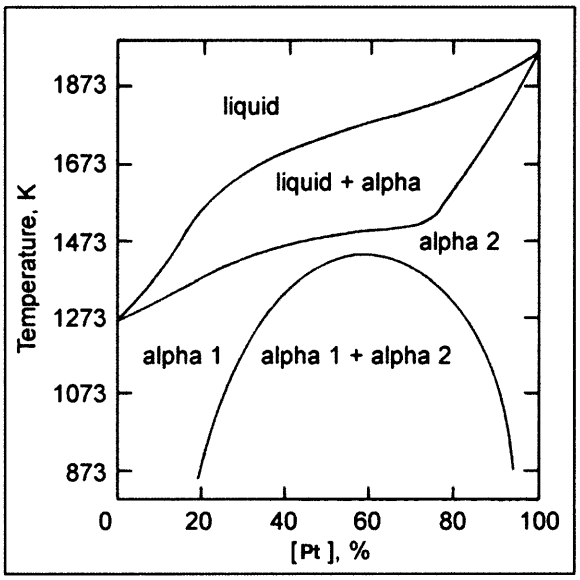

Figure 5.1 Phase diagram for Au-Pt system[2]. The phase diagram of Au-Pt represents deep miscibility gap from about 20% Pt to 5% Au. The segregation of two atoms in wide range of Au-Pt phase diagram suggests the difficulty in formation of single-phase alloy.

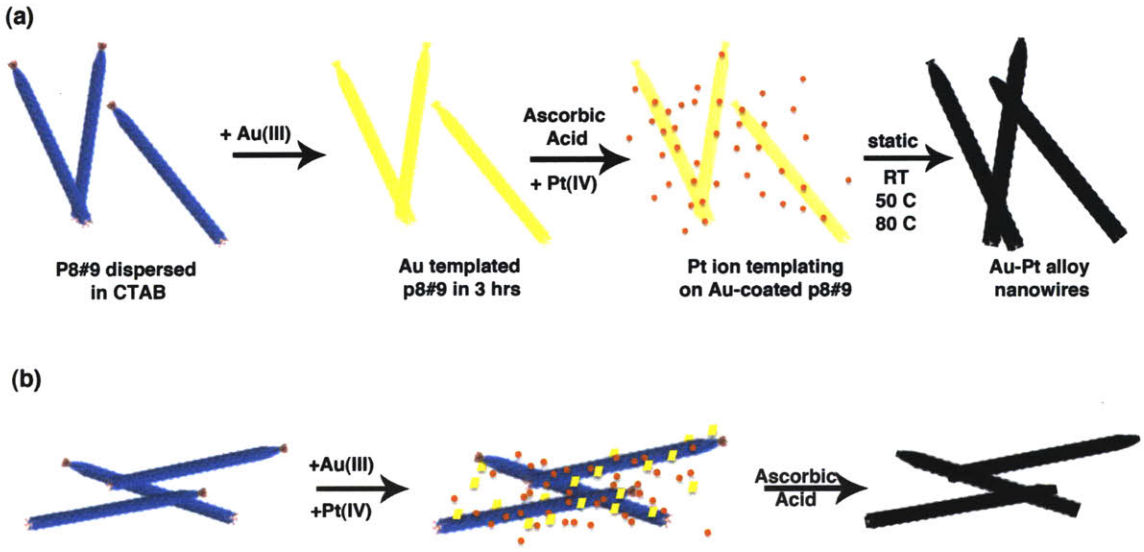

Figure 5.2 Schematic diagram for the preparation of Au-Pt alloy nanowires. Au-Pt alloy nanowires could be prepared in several different ways. Here, the two methods for the preparation of Au-Pt alloy nanowires with higher reproducibility are summarized as simple pictures. (a) P8#9 phage was dispersed in CTAB solution like in the synthesis of Au nanowires. The addition of Au^{3+} ions resulted in p8#9 phage templated with Au ions in three hours. Various amount of Pt^{4+} ions were introduced to the solution and the resultant mixture was further shaken for five minutes at room temperature. Finally, with the addition of excessive ascorbic acid, the Au-Pt alloy nanowires were prepared at room temperature, 50 °C, or 80 °C. (b) The addition of Au^{3+} and Pt^{4+} ions at the same time also produced Au-Pt alloy nanowires with similar structure. In the second method, the phage solution was dispersed in CTAB solution and the metal ions were introduced to the solution together. The solution was incubated for about two hours at room temperature with slight agitation. The addition of ascorbic acid reduced the metal ions to Au-Pt alloy nanowires.

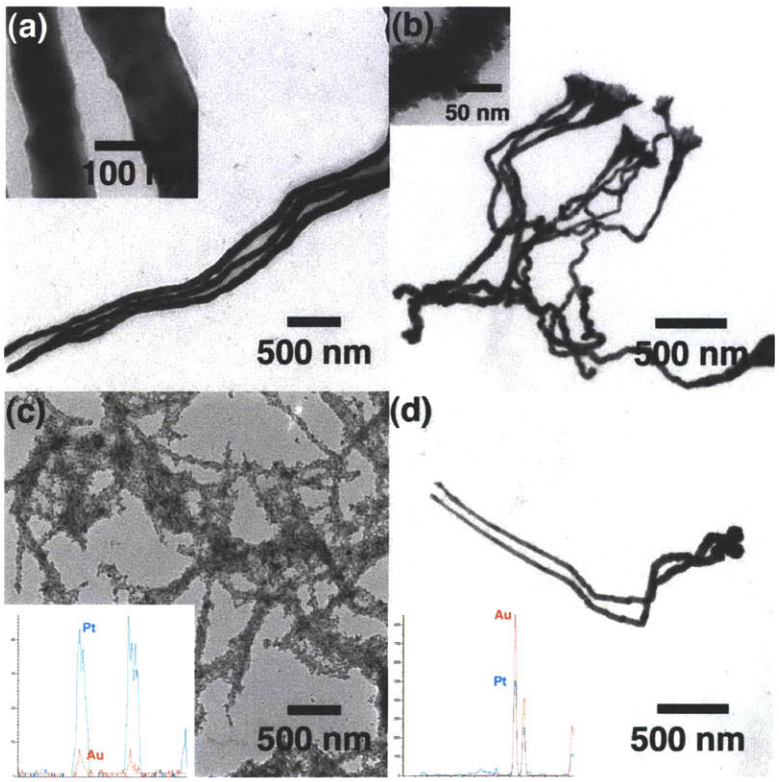

Figure 5.3 TEM images of Au-Pt alloy nanowires prepared at different temperatures. (a) Au-Pt alloy nanowires prepared at room temperature showed smoother surfaces than other nanowires prepared at higher temperature. (b) The nanowires prepared at 50 °C yielded nanowires with flower-like head. The primary structure of Au-Pt nanowires is composed of small nanoparticles as shown in the inset image. Increasing the reaction temperature to 80°C resulted in two different morphologies from a reaction batch: (c) very fine nanoparticles (Pt rich) were coordinated along the phage structure and (d) highly crystalline nanowires (Au rich) with tapered structure.

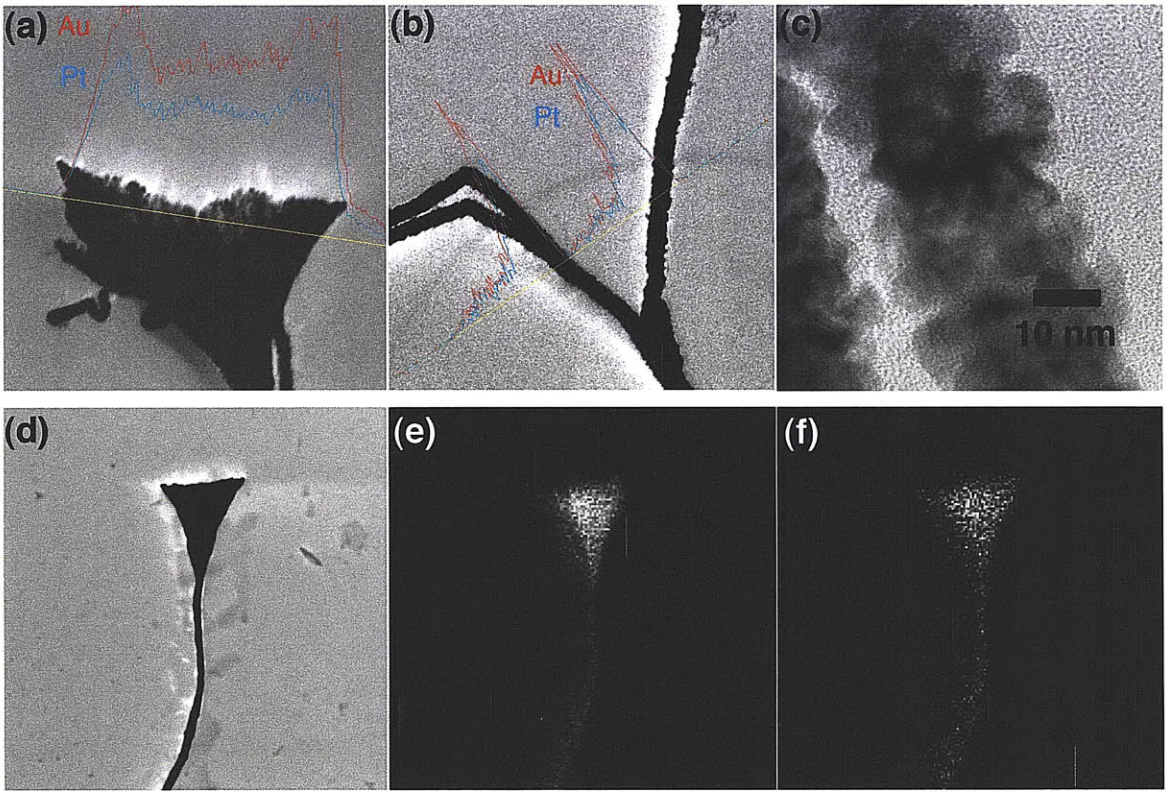

Figure 5.4 EDX line scanning and atomic mapping result of Au-Pt alloy nanowires. For qualitative analysis of Au and Pt, elemental line-scanning was done on the Au-Pt alloy nanowires prepared at 50 °C. (a): on nanowire body and (b): on flower-like end. (c) The main body is composed of smaller nanoparticles. For confirming homogeneous distribution of Au and Pt, elemental mapping was done. (d): Au-Pt alloy nanowires exposed to mapping, (e): trace of Au atom only, and (f) trace of Pt atom only.

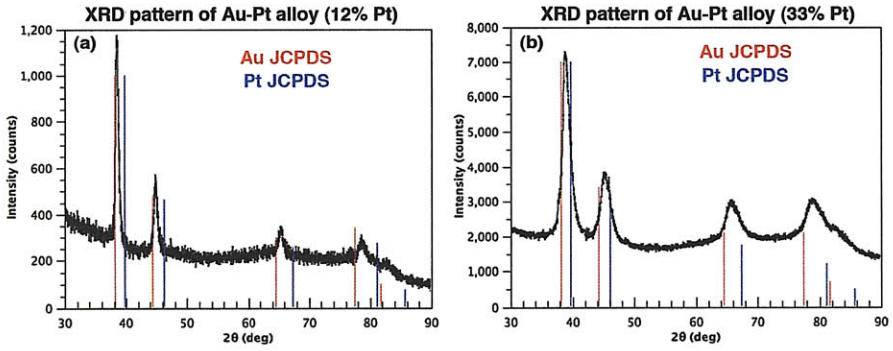

Figure 5.5 XRD results of Au-Pt alloy nanowires with different compositions. The XRD pattern of Au-Pt alloy nanowires fell between the peaks from pure Au and Pt. (a) The XRD peaks from Au-Pt alloy nanowires with the ratio of Au:Pt=7:1 are located closer to that of Au. (b) When the ratio of Pt increased, the peak shifted in the direction to that of Pt. The atomic ratio was Au:Pt=2:1 in Fig. 5.6(b). The peaks in (b) look broader than that of (a), due to the smaller particle sizes with the increased Pt content.

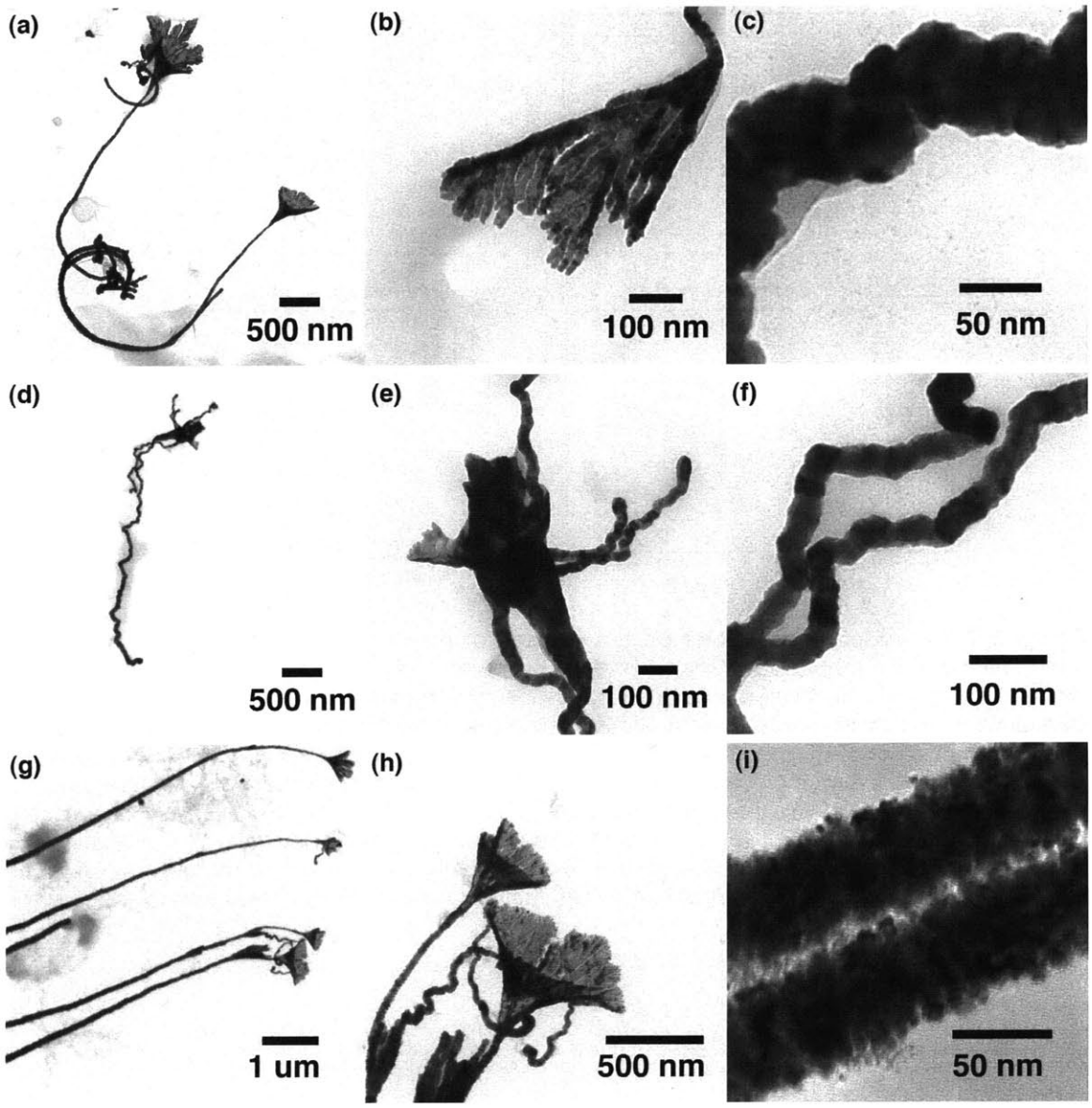

Figure 5.6 TEM images of Au-Pt alloy nanowires with various compositions. The Au-Pt alloy nanowires with various compositions (a, d, g) were prepared at 50 °C. The low-resolution image (b,c and e,f and h,i) showed typical shape of nanowires and the two images were from the end of the nanowire and from the main body. The ratio of $[Pt^{4+}]/[Au^{3+}]$ was 0.5 for (a), 1 for (d), and (2) for (g). The actual composition was different from the ratio of the precursors. The alloy Au:Pt ratios from the final nanowires were calculated to be (a) 7:1, (b) 4:1, and (c) 4:3.

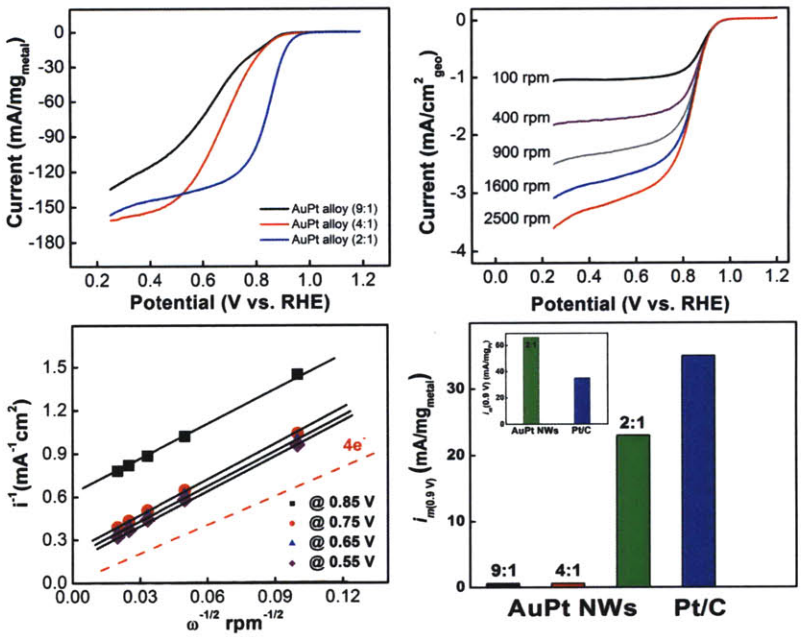

Figure 5.7 O_2 reduction reactions on the surface of Au-Pt alloy nanowires. (a) I-V curve of the 9:1, 4:1 and 2:1 ratio of Au-Pt nanowires in O2 saturated 0.1 M KOH at a rotation rate of 1600 rpm. (b) Au-Pt (2:1) nanowires supported on a glassy carbon disk electrode was tested for their O_2 reduction activity in O_2 saturated 0.1 M KOH and a voltage scan rate of 10 mV/s under various rotation rates at 25°C. Currents are normalized by the geometric disk electrode area and are shown for the positive-going voltage sweep. (c) Koutecky-Levich analysis of the oxygen reduction data on Au-Pt nanowires (from (b)) at 0.85, 0.75, 0.65, and 0.55 V (vs. RHE); the dashed line indicate the expected slope for a 4-electron reduction of oxygen to water. (d) Mass activity comparison of the oxygen reduction at 0.9 V vs. RHE, $i_{m(0.9\ V)}$ (in unit of mA/mg$_{metal}$), of Au-Pt Nanowires and a conventional 10 weight% Pt/C fuel cell catalyst (inset: mass activity comparison in terms of Pt loading).

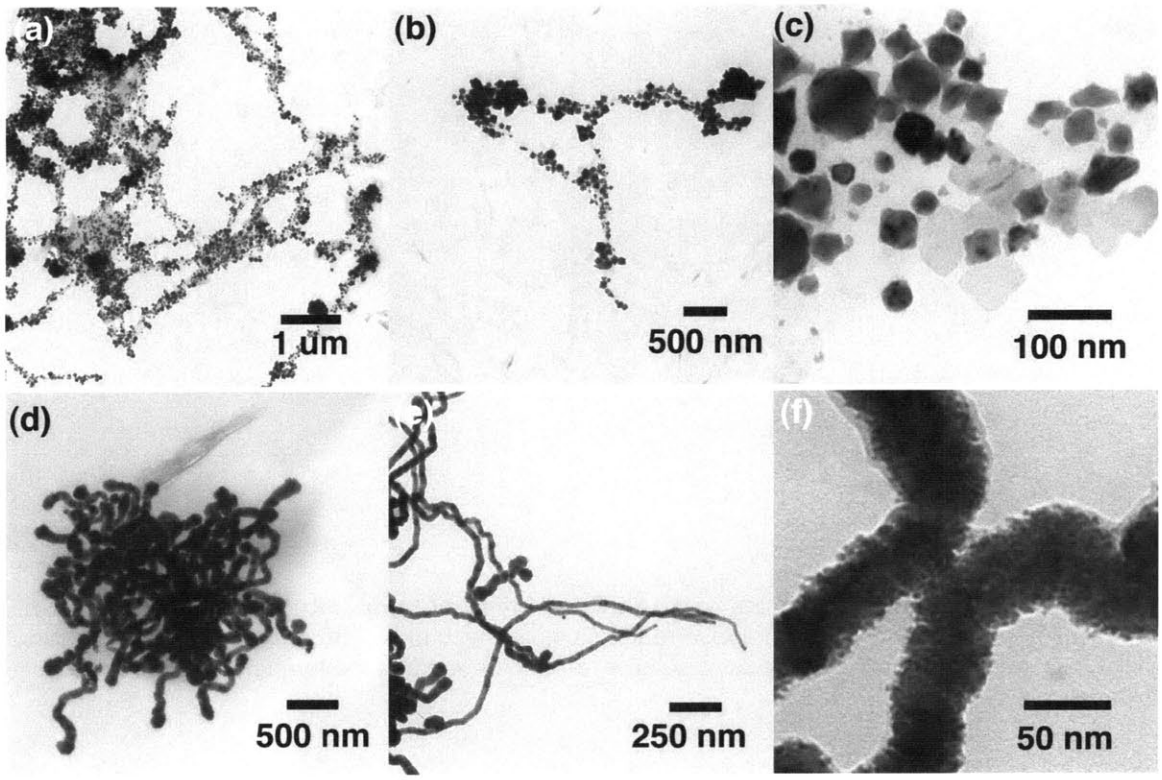

Figure 5.8 TEM images of Au-Pd and Au-Pd-Pt tri-metallic alloy nanowires. Incubation of Au and Pd ions with p8#9 phage resulted in nanoparticles random in sizes and distribution. The TEM images, shown in the first row (a)-(c), represent product obtained by the addition of Pd ions during the synthesis of Au nanowires. The addition of Pt ions into the mixture of Au, Pd, and p8#9 phage resulted in elongated structure as shown in (d) and (e). The Au-Pd-Pt tri-metallic alloy nanowires are also composed of small nanoparticles (f).

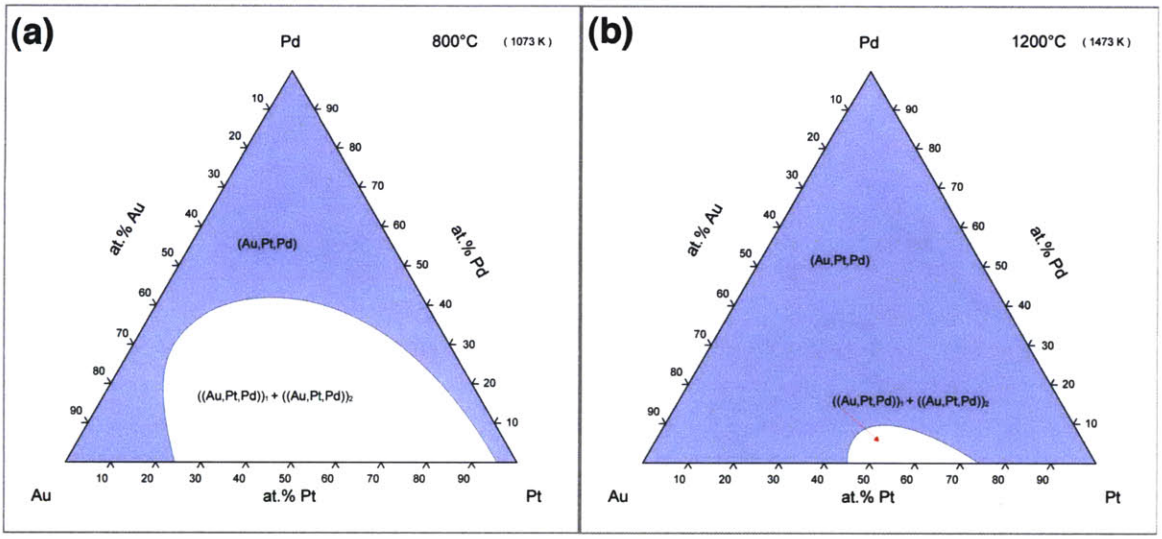

Figure 5.9 Ternary phase diagram of Au-Pt-Pd at different temperatures[19]**.** The Au, Pt, and Pd forms homogeneous solid solution in regions colored with blue. The phase separation occurs in regions colored with white. The solid solution area increased as the temperature increased from (a):800 °C to (b): 1200 °C

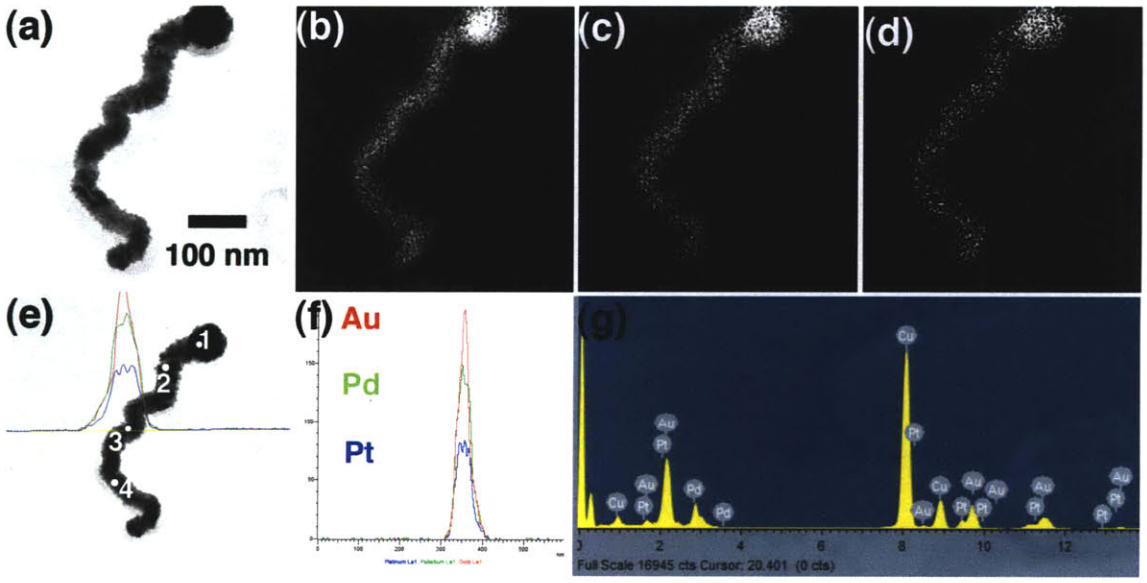

Figure 5.10 Elemental mapping and EDX line scanning of Au-Pd-Pt tri-metallic alloy nanowires. The tri-metallic Au-Pd-Pt alloy nanowire shows homogeneous distribution of each component (b): Au, (c): Pd, and (d): Pt. From the point analysis and the line scanning result, the composition was determined to be Au:Pd:Pt = 5:3:2.

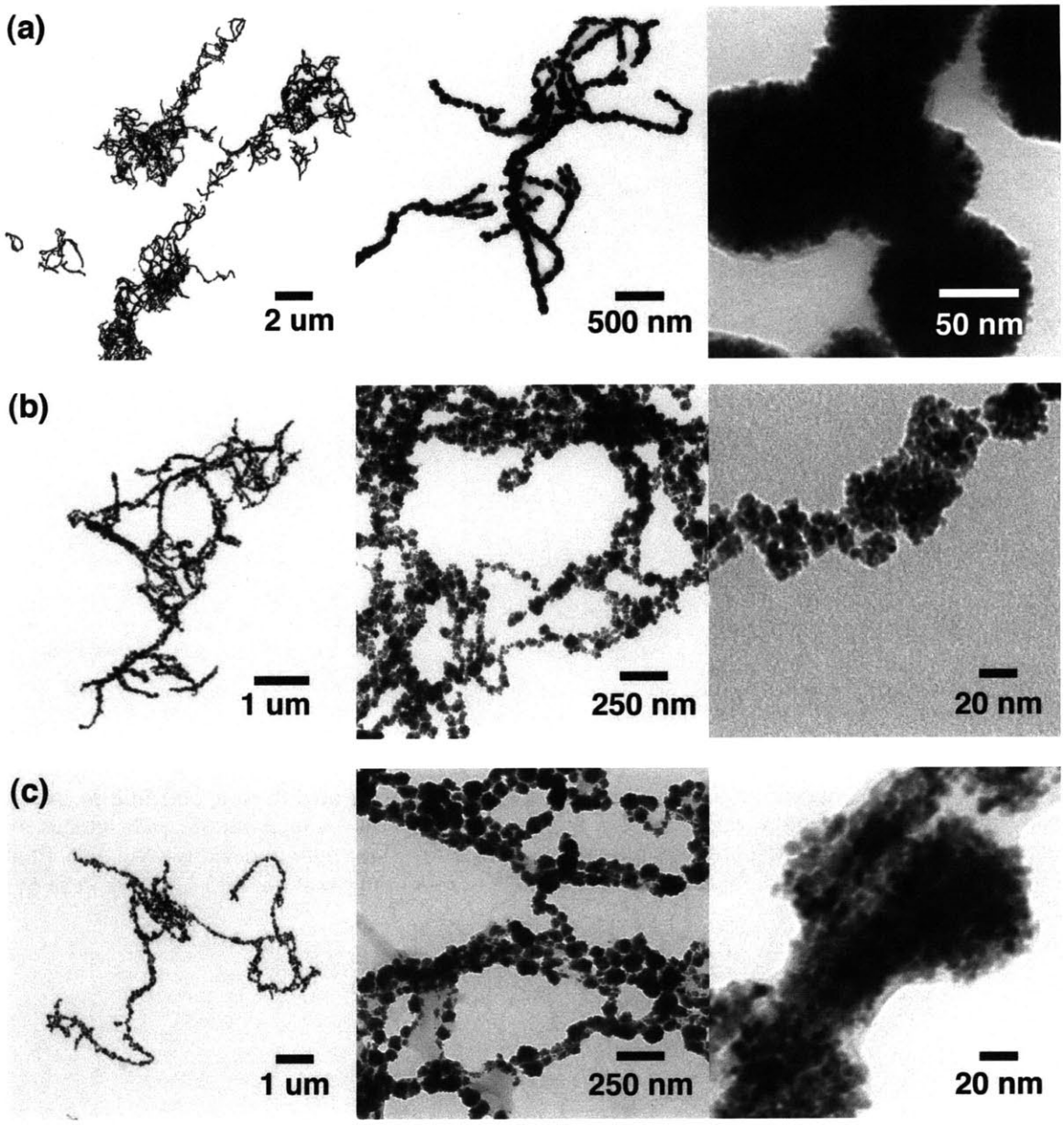

Figure 5.11 TEM images of surfactant-free Au-Pt nanowires from various phage concentrations. The as-prepared nanowires were prepared by varying the concentration of template, the p8#9 phage. The concentrations of p8#9 in each experimental set were (a): 1.1×10^{9} pfu/mL, (b): 9.4×10^{9} pfu/mL, and (c): 4.0×10^{10} pfu/mL.

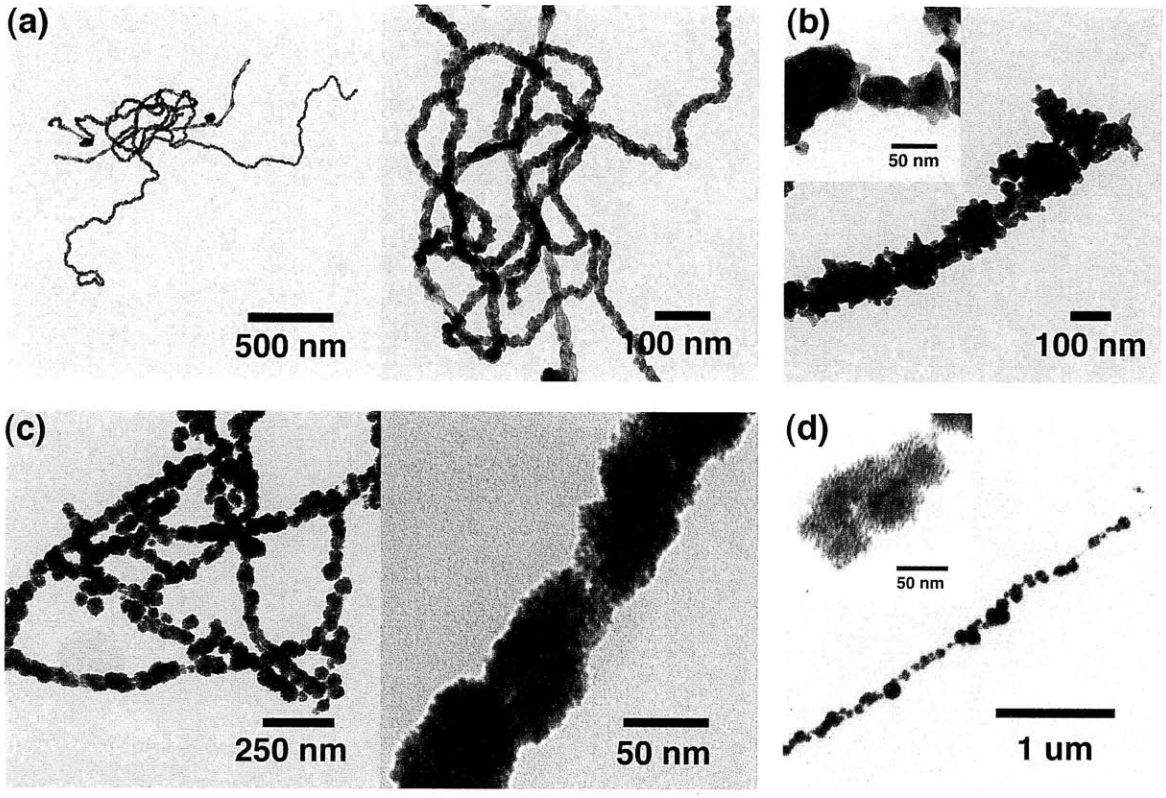

Figure 5.12 TEM images of Au-Pt alloy nanowires prepared at different conditions. Au-Pt alloy nanowires with phage concentration around $9x10^9$ pfu/mL were prepared with various Pt compositions at two different reaction temperatures (room temperature and 50° C). (a): 10% Pt at room temperature, (b): 10% Pt at 50° C, (c): 50% Pt at room temperature, and (d): 50% Pt at 50° C.

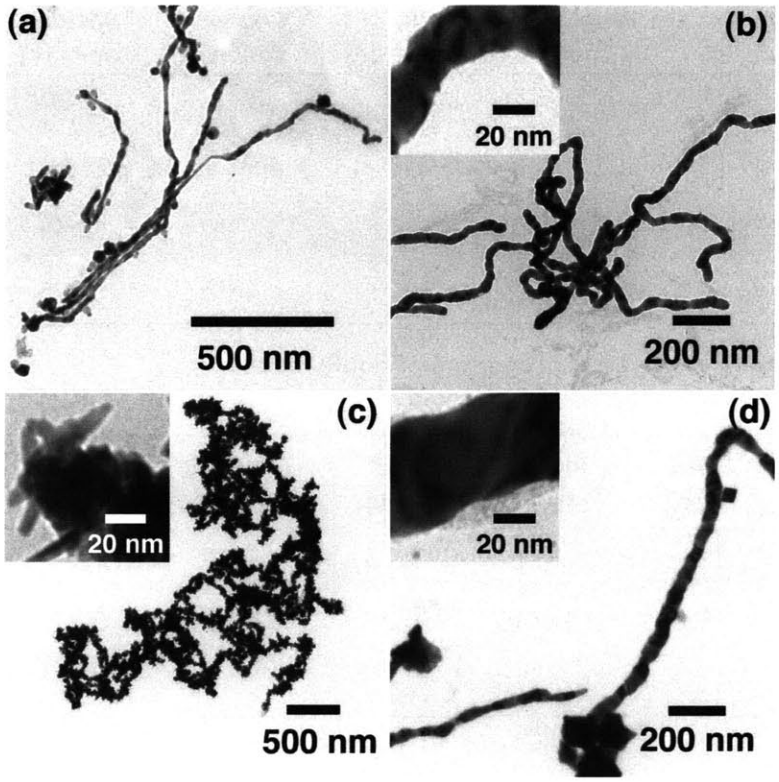

Figure 5.13 TEM images of Pt nanowires prepared from p8#9 templates. (a) Pt nanowires stabilized with CTAB molecule prepared at room temperature. (b) Pt nanowires with free surfaces reduced by ascorbic acid at room temperature. (c) Pt nano-bundles reduced by sodium borohydride at room temperature. (d) Pt nanowires with free surfaces reduced by ascorbic acid at 50 °C.

	Atomic number	Weight [g/mol]	Lattice parameter [Å]	Electronic structure	Melting point [K]	Density [g/cm^3]
Au	79	196.97	4.080	$5d^{10}\,6s^1$	1337.6	19.3
Ag	47	107.87	4.090	$4d^{10}\,5s^1$	1235.1	10.5
Pt	78	195.08	3.920	$5d^9\,6s^1$	2045	21.45
Pd	46	106.42	3.890	$4d^{10}$	1825	12.02

Table 5-1. Summary of physical properties of noble metals.

Sample	CTAB [mM]	PHAGE [pfu/mL]	Au^{3+} [mM]	Ascorbic acid [mM]	Pt^{4+} [mM]	Au:Pt in nanowires
(a)	39.7	$9.26X10^9$	0.26	3.44	0.13	7:1
(d)	39.2	$9.14X10^9$	0.26	3.40	0.26	4:1
(g)	39.7	$9.26X10^9$	0.13	3.44	0.25	4:3

Table 5-2. Concentration of reactants for the preparation of Au-Pt alloy nanowires shown in Fig. 5.5. All the concentration was summarized in mM [m mol/L]. The unit pfu means plaque-forming units for counting active colony of M13 phage after each amplification. Final composition was determined from ICP-OES and EDX point analysis.

Sample	CTAB [mM]	PHAGE [pfu/mL]	Au^{3+} [mM]	Pt^{4+} [mM]	Ascorbic acid [mM]	Au:Pt in nanowires
A	41.3	$1.10x10^9$	0.14	0.069	1.51	9:1
B	40.8	$1.09x10^9$	0.14	0.14	2.17	5.5:1
C	41.2	$1.10x10^9$	0.69	0.14	1.79	4:1
D	40.1	$1.07x10^9$	0.067	0.27	2.71	2:1

Table 5-3. Concentration of reactants for the preparation of Au-Pt alloy nanowires from reduced phage concentration. In this synthesis, the Au^{3+} and Pt^{4+} ions were added into the phage solution together as explained in scheme 2.

Chapter 6. Synthesis of Au/Pt core/shell nanowires and the electrocatalytic activities in O_2 reduction and ethanol oxidation reactions

6-1. Introduction

Platinum (Pt) is an essential component in catalyst of various fields. Much research has been focused on the design of catalysts to compete with the outstanding catalytic activity of Pt because it is supply-limited and less cost-effective, but the intrinsic property of Pt is not easily compensated by with other noble metals. Therefore, the fabrication of Pt catalyst has been developed in the direction to maximize the active surface sites of Pt: porous Pt nano-structure, branched dendritic Pt, multi-pods nanowires, and core/shell structures[1,2,3]. Core/shell nanoparticles were initially designed either for increasing the surface exposed outside by combining less important material as core with more active one as shell, or for utilizing multi-functionality from one material domain. For example, a core/shell material could have a magnetic core for magnetic control and a silica shell for embedding enzymes[4,5].

However, recent reports about the unusual electronic, optical, and catalytic properties synergistically arising from the corresponding elements of core/shell nanoparticles have drawn much attention to build various core/shell nanoparticles with properties finely tuned by size, crystallographic direction, and structure[1]. For example, from the electronic interaction between Au and Pd, Pd-decorated Au nanoparticles showed catalytic activity, which was substantially increased on hydrodechlorination reaction[2]. Addition of secondary metal component such as Ru and Sn on Pt catalysts enhanced the activities of Pt in methanol oxidation[3]. The promotional effects utilized the electronic interaction between two atoms or the changes in lattice parameter from alloying[4,5,6]. Even though Pt is the main catalysts in various fields with highest activities, the applications of Pt nanoparticles in oxidation reaction of alcohols are challenging. The

stepwise dehydrogenation of alcohol leaves intermediate chemical species, such as CO and CHO, on the surface of Pt catalyst, which results in gradual loss of catalytic activity of Pt. The problematic poisoning of Pt catalysts by CO and CHO especially at low temperature has been resolved by adding oxophilic metal component such as Sn and Ru[7,8]. Therefore, the development of Pt shell nano-structure on a metal core, which could help the removal of CO and CHO, is consequential not only for extending the active surface area but also for exploring any advantage from the core materials[9].

The bottom-up synthesis of Pt nanoparticles are usually stabilized with surfactant and polymers to maintain small domains in several nm sizes. However, the catalytic activity of Pt could be drastically deteriorated by impurities especially having strong interaction with Pt surfaces, so the selection of surfactant molecule that interacts with Pt stable enough to keep the nano-structure and moderate enough to catalyze reaction appropriately is a challenge. The interaction between Pt and CTAB, one of the ionic alkyl ammonium surfactant, is found to be weaker than that of other metal-surfactant pairs[10]. The weaker interaction of Pt-CTAB than that of Au-CTAB was also confirmed in previous chapter for the preparation of CTAB mediated Au-M alloy nanowires in that the composition of Pt was lower than that of Pd and Ag: almost 100% of Ag and 60% of Pd were incorporated to the alloy nanowires, but less than 40% of Pt was incorporated to Au-Pt alloy nanowires. The number was increased when the nanowires were prepared without CTAB.

To increase the high-energy Pt surfaces covered by surfactant molecules with less-strong interaction with Pt, here we report, a facile synthesis of Au/Pt core/shell nanowires from the extended synthetic method of Au nanowires as shown in figure 6.1

(a). Previous reports of Au/Pt core/shell nanoparticles are also promising in that they showed enhanced catalytic activity of Pt when they were prepared as hybrid core/shell structures, but the systematic study for more precise correlation between the shell thicknesses and the catalytic activities is not clearly reported due to the difficulties in preparing uniform cores and in controlling homogeneous shell thickness[11]. Since we confirmed the activities of Au and Au-Pt alloy nanowires as a co-catalyst and a catalyst in the low temperature fuel cell electrodes in previous chapters, we also measured the electro-catalytic activities of Au/Pt core/shell nanowires with various Pt shell thickness, various ratio of Au:Pt atomic ratios, on oxygen reduction reactions and ethanol oxidation reactions.

6-2. The virus fuel cells

Fuel cells are a type of clean energy device that converts chemical energy stored from hydrogen or hydrocarbon fuels into the electrical energy. It has higher specific energy [Wh/kg] than batteries and capacitors, thus is comparable with the combustion engines[12]. Fuel cells and batteries have similarities in that they utilize chemical energy through redox reactions at the anodes and cathodes. However, unlike the closed system of batteries where the anodes and cathodes participate in the charge-transfer redox reaction by themselves and thus carry out the active roles, the fuel cell anodes and cathodes only transfer charges to the reactants supplied from external source. Therefore, the fuel cell is called an open system. Figure 6.1 (b) represents simple low temperature fuel cells composed of an anode, cathode, and the electrolyte. At the anode, the oxidation reaction of fuels produces electrons and ionic species transferred to cathodes through the electrolyte. At cathode, O_2 undergoes a reduction reaction to produce water either by the direct formation of water or the serial reaction with hydrogen peroxide (H_2O_2) intermediates, which could erode the electrode materials. The introduction of Pt or a Pt-based catalyst improves both the dissociation of fuels at the anode and the direct formation of water at the cathode. To facilitate the direct formation of water from O_2, enough loading of Pt is required, but in the oxidation of hydrocarbon fuels, Pt catalyst that can tolerate decaying from CO poisoning is essential. With the excellent activity of Au nanowires in the oxidation reaction of CO in chapter 3 and the Au-Pt alloy nanowires in reduction of oxygen in chapter 5, here we propose the virus fuel cell based on the Au/Pt core/shell catalysts for both electrodes with desired criteria (Fig. 6.1(c)).

6-3. Synthesis of Au/Pt core/shell nanowires

The Au/Pt core/shell nanowires were prepared by utilizing the Au nanowires discussed in chapter 3. The as-prepared Au nanowire is a good candidate as core material for several reasons: (i) the Au nanowires are homogeneous without size selection, (ii) high conversion yield of Au^{3+} to Au nanowires rules out any possible reactions between un-reacted Au^{3+} ions and Pt^{4+}, (iii) the stability of Au nanowires provide robust building blocks for Pt shells, and (iv) the three layer structure (p8#9, gold, and platinum) reduces cost of noble metals, which are usually sacrificed as dead volume. Au core nanowires were prepared as described in chapter 3-3. 15 mL of 0.1 M CTAB solution was mixed with 10 mL of de-ionized water and 10 mL of p8#9 phage solution with 3.5×10^{10} pfu/mL. 1mL of 10 mM Au^{3+} solution was added to the mixture of phage and CTAB surfactant and incubated for three hours. The Au-p8#9 complex with partially reduced Au^{+} was then further reduced by ascorbic acid and Ag ions. The solution was kept for one day to complete the formation of nanowires and then used as core material for core/shell nanowires. Considering the high conversion of Au^{3+} ions to Au nanowires, which is more than 98% in most cases, the concentration of Au nanowires in the as-prepared solution is about 55 ppm [mg/L or μg/mL].

Figure 6.1(a) is the simplified schematic diagram for the preparation of Au/Pt core/shell nanowires from p8#9 phage template. From the specific interaction between the p8#9 phage and Au^{3+} ions, the Au nanowires were prepared first, and Pt^{4+} ions were added to the dispersion of Au nanowires in CTAB solution. The Au nanowire solution was used without any purification or separation, and no extra CTAB solution was added. The mixture of Au nanowires with Pt^{4+} ions was then incubated for two hours with gentle

shaking at room temperature. After the incubation, ascorbic acid was added and the solution was shaken for another five minutes at room temperature. The solution was then transferred to the 50 °C oven and kept for overnight to form rough Pt shells composed of dendritic Pt nanoparticles on Au cores. Lowering the reaction temperature to 20 °C (room temperature) resulted in monolithic Pt shells with smoother surface and lower Pt content. Strictly speaking, the Au/Pt core/shell nanowire is a triple layer of M13 phage, Au, and Pt metals as shown in cross-sectional image in Fig. 6.1(a).

Figure 6.2 is the TEM image of Au core and Au/Pt core/shell nanowires taken at the same magnification ((a) and (b), (c) and (d)). Obviously, the diameter of the core/shell nanowire (Fig. 6.2(b)) is thicker than that of the Au core (Fig. 6.2(a)), and the surface structure is also changed with the formation of Pt shells as shown in Fig. 6.2(d). While the core Au nanowires show rippled surfaces coming from the coarsening of Au nanoparticles along the p8#9 phage, the Au/Pt core/shell nanowires exhibit very fine nanoparticles covering of the Au cores (Fig. 6.3). The Pt nanoparticles, coating the Au core nanowire, are dendritically dispersed over the whole surface nanowires and the individual nanoparticle size is less than 3 nm. The method for the preparation of Au/Pt core/shell with dendritic Pt nanoparticle is described below.

Experimental procedures

For the preparation of Au/Pt core/shell with a 1:1 atomic ratio of Au:Pt, 3 mL of homogeneous Au nanowire solution was transferred to a 15 mL falcone tube, and 200 μL of 10 mM Pt^{4+} solution from chloroplatinic acid hexahydrate ($H_2PtCl_6 \bullet 6H_2O$) was added. The solution was incubated for two hours on a

rocking platform with gentle shaking to induce Pt^{4+} ions to the surface of Au nanowires, and then 400 μL of 0.1 M ascorbic acid was added to reduce Pt^{4+} ions to Pt nano-shells. The solution was kept at 50 °C overnight without agitation.

TEM preparation

10 μL of the as-prepared nanowire solution was drop casted into the carbon coated copper grid and left static for 20 minutes. Before the water evaporation, additional de-ionized water was casted to wash out salts and excess surfactant and removed by adsorbent paper by contacting the edge of grid.

6-4. Confirmation of Au/Pt core/shell structure

As a simple analysis for confirming the existence of Pt shell on Au nanowires, UV-Vis absorption spectra were measured from the nanowire solutions with different Pt concentrations. The absorption spectrum from Au core is also attached as a reference to compare the change in absorption phenomena. Figure 6.4 (a) shows the absorption spectrum of Au/Pt core/shell nanowires with 2.6:1 (Au excess) atomic ratio still retains the characteristic surface plasmon resonance peak around 520 nm implying the detection of Au surfaces. The exposure of core materials from the dendrite Pt nanoparticles on Au core is common especially for structures with Au/Pt atomic ratio larger than 1[13]. The characteristic Au peak disappeared when the Pt shell thickness increased and also the atomic composition of Pt becomes comparable with that of Au (Fig. 6.4(b)). Contrary to the sharp peak from the aqueous Pt^{4+} solution, the peak from Pt nanoparticles shows a gradual increase in absorbance from the longer wavelength edge of visible light to UV[14].

To further visualize the core/shell structure, scanning transmission electron microscopy (STEM) and dark field TEM analysis with selective atomic mapping was done on the nanowires with Au:Pt atomic ratio of 1:1 (Fig. 6.5). As shown in Fig. 6.5 (a), Au (red) atoms are located inside while the Pt (green) atoms are found mostly outside of the nanowires. The very dilute green colors mixed with red dots are from the Pt shells positioned on top of the Au nanowires under the electron beam. From the nanowires shown in Fig. 6.5 (b), each Au (c) and Pt (d) atom was chosen to image separately. When imaged from the position of nanowire, the displayed Au atoms are more focused to the nanowire center and the distribution of Pt appears broader than that of Au, implying the existence of Pt as a shell layer of the nanowires.

The crystallographic structure of Au/Pt core/shell nanowires was studied from powder X-ray diffraction methods. The XRD pattern of core/shell nano-materials strongly depends on various parameters: class of materials, thickness of shell, and the position of each component. For example, the combination of Pt and Cu, having FCC structure with different lattice parameters (Pt: 3.920 Å and Cu: 3.610 Å), could create Pt/Cu core/shell, Cu/Pt core/shell, and Pt-Cu alloys with various XRD peaks. Despite the big difference in atomic weight of Cu and Pt, both peaks were independently observed in Cu/Pt core/shell nanoparticles[15]. Au/Pd core/shell systems for electrochemical applications mostly features strong Au peaks in the absence of Pd peaks[16,17], but separate Pd peaks are also reported when the thickness of Pd shell increased[18]. The magnetic/Au core/shell nanoparticles heterogeneous catalysts were known to exhibit only Au peaks from heavy atom effects[19,20], but the peak pattern from magnetic nanoparticles was visible when decreasing Au layers less than 2 nm[21].

The X-ray diffraction (XRD) pattern from the Au/Pt core/shell nanowires (composition of Au:Pt = 1.8:1), plotted with the peaks of pure Au and pure Pt in JCPDS data, clearly depicts characteristic peaks fit very well with pure Au (Fig. 6.6(a)). Considering the similar atomic weight of Au and Pt, the heavy atom effect obliterating crystallographic diffraction pattern from the lighter atom cannot explain the absence of peak from Pt. The absence of a XRD peak from Pt shell could be explained by the particle size and shell thickness. The dendritic Pt nanoparticles covering the Au nanowire are much small than the monolithic Au core: the Au nanowires used as the core have an average diameter size of 30 nm and are continuous, but the sizes of individual Pt nanoparticles range from 2 to 3 nm. Assuming the Pt shell as monolithic metal layer

resulted in a 3 nm shell thickness for nanowires with a 1.8:1 (Au:Pt) atomic ratio from calculations based on a 30 nm diameter of Au core and a 6 nm of M13 phage. Therefore, we believe the Au core in these Au/Pt core/shell nanowires are covered with one or two Pt nanoparticles with spaces between the particles. As we can see from the TEM image in Fig. 6.6(c), taken from Au/Pt core/shell nanowires used for XRD analysis, the whole nanowire appeared to have a diameter of about 35~40 nm, which is congruent with the values calculated above.

A closer look at the XRD peak pattern from the Au/Pt core/shell nanowires revealed the un-symmetric peaks in the direction of larger 2θ values and as shown in the inset, the Pt characteristic peaks are positioned in the middle of the shoulder peak. The incremental peaks are considered to be overlapping the peaks from Au and Pt, and the XRD intensity data from the first peak of Au to that of Pt could be divided into the sharp Au peak and the broad Pt peak (Fig. 6.6(b)). Therefore, the high intensity peaks with un-symmetric shoulder resulted from the overlapping of the main peaks from Au cores and the reduced peaks from Pt shells. The smaller particle sizes and thinner shell of Pt compared with that of core Au resulted in much weaker diffraction from Pt despite the similar atomic weight and its location at the outer shell. The core Au nanowire and the thin Pt shell nanoparticles are visible from the TEM image (Fig. 6.6 (d)).

6-5. Control of shell thickness of Au/Pt core/shell nanowires

A great advantage of Au/Pt core/shell nanowires is the ease of tuning Pt shell thickness by changing the concentration of Pt^{4+} ions added during the incubation step. From the selective reaction only occurring on the surface of Au nanowires with uniform shell thickness, Au/Pt core/shell nanowires with different Pt shell thickness were successfully prepared. The atomic % of Pt, related to the shell thickness, was increased systematically from 3:1 to 1:1.2 (Au:Pt atomic ratio) in synthesis of dendritic Pt shells and from 13:1 to 6:1 in synthesis of monolithic Pt shells (reaction completed at 20 °C). We will discuss various reaction conditions for the preparation of Au/Pt core/shell nanowires below. There is slight deviation (less than 10%) of atomic ratios in Au/Pt, but controlling Pt shell thickness by adjusting the amount of Pt^{4+} ions and ascorbic acid is reproducible.

Figure 6.7 represents line-scanning results of Au/Pt alloy nanowires from different reaction conditions: the room temperature synthesis resulted in very thin monolithic Pt with a Au:Pt atomic ratio of 13:1 as shown in Fig. 6.7 (a) and Fig. 6.7 (b) is the line scanning of nanowires prepared at a higher reaction temperature (50 °C) showing increased Pt shell thickness with atomic ratio of 1.8:1 (Au:Pt). The change in temperature from 20 °C to 50 °C greatly affected the thickness of Pt shell formed on the surface of Au nanowires, in other words, the yield of Pt (the amount of Pt^{4+} reduced to Pt metal). The conversion yield of Pt at 50 °C, the percentage of Pt^{4+} reduced to Pt nanoshells, calculated from the ICP-OES result of Au and Pt under the assumption of 100 % conversion of Au^{3+} was 40%. Therefore, considering the same concentration of Pt^{4+} in

both cases, the yield of Pt in the reaction at 20 °C was lower than 10%. This yield was further increased to about 50% when the reaction temperature was increased to 100 °C.

Figure 6.8 is the TEM images of Au/Pt core/shell nanowires with different Pt shell thickness prepared from one batch of Au core nanowires. To control consistency in the Au core, one large batch of Au nanowires was prepared with a narrow size distribution of diameter size. The four samples shown in Fig. 6.8 were prepared by adding different amount of Pt^{4+} ions and ascorbic acids. The thickness of the nanowires was increased with increasing Pt^{4+} concentration and the surface of monolithic Au nanowires is only visible in images of lower Pt content implying coverage of Au nanowires with Pt nanoparticles. Au nanowires, composed of smaller crystalline domains connected along a single nanowire, resulted TEM images with alternating dark and bright regions under the beam of TEM due to the different transmittance of light depends on the crystalline structures: for FCC crystal, the atomic density on directions (100), (110), and (111) varies. With the full coverage of Pt nanoparticles, the alternating dark and bright pattern from the Au crystallites was not observed in Fig. 6.8(d).

The detail experimental procedure is summarized as Table 6-1.

6-6. Application of Au/Pt core/shell nanowires as catalysts in low temperature fuel cell electrodes

For application of Pt as catalysts, Au/Pt core/shell nanowires with dendritic Pt shell are more attractive than those of monolithic Pt layer for several reasons: higher yield of Pt^{4+} for cost effective catalysts and larger surface area of Pt for more active sites. As the applications of Au nano-materials as new catalysts have been reported recently, exploring the catalytic activity of Au/Pt core/shell nanowires with different Pt shell thickness is important not only to investigate the activity changing with the thickness of Pt shell but also to examine any synergic effect of the Au core to improve the activity of Pt shell. For the measurements of Au/Pt core/shell nanowires in their electrocatalytic activities, nanowires were washed with de-ionized water three times. The atomic concentrations of Au and Pt of Au/Pt core/shell nanowires used for electrochemical study are summarized in Table 6-2.

The working electrode was prepared as described in previous sections (section 5-5). 20 μL of nanowire suspension was applied onto a glassy carbon rotating disk electrode (RDE), which has 0.196 cm^2 geometrical surface area. Therefore, we have several μg loading of Au/Pt core/shell nanowires. After evaporating the water, 15 μL of 0.05 wt% Nafion® solution was casted onto the film of Au/Pt core/shell nanowires deposited to fix the nanowire films physically and to ensure ionic conductivity for measurement. Figure 6.9 represents cyclic voltammograms of Au/Pt core/shell nanowires with various compositions (Au:Pt = 2.6:1, 1.8:1, and 1:1). Because we used the same Au cores for the synthesis, the notation for composition with Au:Pt = 1:0.38, 1:0.55, and 1:1 would represents the composition more accurately. The atomic % of Pt is 28, 35, and

50% respectively. The CV curves exhibited two distinctive potential regions associated with under-potentially deposited hydrogen (H_{upd}) and adsorbed hydroxyl species (OH_{ad}). H_{upd} happens in a potential range from 0 to 0.4 V vs. RHE and OH_{ad} at over 0.6 V vs. RHE respectively. The strong peak at 0.60 V vs. RHE is associated with the reduction of Pt oxide species, which were built on the surface of Pt nanoshell during the positive sweep of potential.

As shown in Fig. 3.12 (c), the measurement of active surface area of Au at alkaline condition, Au nanowires underwent oxidation and reduction during the CV measurement. The peak potential would shift slightly due to the change in scan rate [mV/s], but the oxidation of Au occurred during the positive sweep over 1.0 V vs. RHE and the Au-oxide reduced to Au during the reverse sweep under 1.0 V vs. RHE. Even though the Au nanowires were coated with Pt shell, the dendrite Pt shell allowed Au surfaces as shown smaller figure in Fig. 6.9. The characteristic reduction peak of Au oxide was not observed in nanowires with increased Pt shell. It supports the full coverage of Pt shell on the surface of Au nanowires as confirmed in UV-Vis absorption in Fig. 6.4. Form this CV measurements, the mass of nanowire catalysts was quantified in terms of active surface areas in alkaline medium of 0.1 M KOH solution.

6-7. O_2 reduction reaction on Au/Pt core/shell nanowires

The Au nanowires showed excellent activity toward CO oxidation as reported in Chapter 3.10, but the reduction of O_2 on the surface of Au nanowires was not efficient both in onset potential and the kinetics of reduction pathway as described in Chapter 3.11. However, a promising result was acquired from the reduction of O_2 on the surface of Au-Pt alloy nanowires with higher Au contents as reported in Chapter 5.6. The addition of Pt component on Au nanowires enhanced the activity of Au-Pt alloy nanowires close to that of Pt. This could be explained by the change in electronic structure and in lattice parameter of Au by alloying with Pt as confirmed in other alloy catalysts[22]. Here, we tested nanowires with same combination of Au and Pt but with different structure to the reduction of O_2. To test the dependency of Pt shell thickness in O_2 reduction reaction, RDE polarization curves were obtained from Au core, Au/Pt core/shell nanowires and the commercial Pt/C catalysts.

Figure 6.10 represents the RDE curves obtained from various rotating speed at scan rate of 10 mV/s on the surface of Au and Au/Pt core/shell nanowires with various Pt shell thickness. The RDE curves all showed typical current-potential curves for O_2 reduction. For further insights into the O_2 reduction dynamics, Koutecky-Levich plots were done for each case and added to RDE curves[23]. To compare the effects of Pt shell thickness on the reaction, RDE voltammograms of Au and Au/Pt core/shell nanowires at 1600 rpm were collected together (Fig. 6.10(e)). Even though the amount of loading was slightly different in each case, the onset potential, which is independent of loading amount, clearly revealed the positive shift as the Pt shell thickness increased. The onset potential of pure Au was about 0.8 V vs. RHE but the onset potential of Au/Pt core/shell

nanowires with 1:1 atomic composition is close to 1.0 V vs. RHE, which is typical value of pure Pt. The commercial Pt/C tested in the same electrochemical analysis system started reaction at 1.0 V vs. RHE as shown in Fig. 6.10 (f).

As already shown in potential profiles in Fig. 6.10(e), the Au/Pt core/shell nanowires with atomic ratio of Au:Pt=1:1 showed better activity toward O_2 reduction reaction. A Koutecky-Levich plot at 0.6 V vs. RHE provided apprehensive insights into the reaction pathways whether the main reaction of O_2 reduction to water molecule is $4e^-$ process or $2e^-$ process (Fig. 6.11(a)). The number of electrons involved in the reduction of oxygen was systematically increased from 3.7 to 4.4 with the contents of Pt increased. The number 3.7 from nanowires with composition of Au:Pt=2.6:1 was also calculated from the Au-Pt alloy nanowires with 2:1 atomic ratio in Chapter 5.6. The same efficiency was found from nanowires with different morphologies and compositions: the atomic % of Pt was 33% for Au-Pt alloy nanowires and 28% for Au/Pt core/shell nanowires. Even though less Pt was used in Au/Pt core/shell nanowires than in Au-Pt alloy nanowires, considering the fact that electrochemical reaction occurs on the surface of materials, the synergic effect originated from alloying Au and Pt as solid solution can be addressed.

To quantitatively compare the activity of nanowires with various shell thicknesses, specific activity and mass activity at 0.9 V vs. RHE were plotted with the activities from commercial Pt/C in the same reaction condition. The specific activity is normalized by the electrochemical surface area of Pt measured by the CV curves in Fig. 6.9. The activity of Au/Pt core/shell nanowires increased as the thickness of Pt shell increased as was expected. Theoretically, the specific activity of Au/Pt core/shell nanowires would saturate over a critical point because the reaction only happens on the

surface of nanowires. The activities of Au/Pt core/shell nanowires of 1.8:1.0 and 1.0:1.0 are quite comparable despite the considerable difference in composition of Pt about 14% as shown in Fig. 6.11(b). The optimized composition of Au/Pt core/shell nanowires in terms of efficiency and the cost of catalyst is expected between the composition of 1.8:1 and 1:1.

The mass activities were normalized with the total metal mass, the sum of Au and Pt in Au/Pt core/shell nanowires and Pt in commercial Pt/C. The mass activity was also enhanced as the thickness of Pt shell increased. The mass activity of Au/Pt core/shell nanowires with 1:1 atomic ratio exhibited higher activity than that of commercial Pt/C about 1.5 times. If the activities were normalized with pure Pt mass, the activity of Au/Pt core/shell nanowires with 1.8:1 atomic ratio would be higher than that of commercial Pt/C and the activity of nanowires with 1:1 atomic ratio would be three times of that of Pt/C.

6-8. Ethanol oxidation reaction on Au/Pt core/shell nanowires.

As we already referred in Chapter 6-1, the application of Pt catalysts was not efficient in reduction of alcohols due to the susceptible to decay of Pt activity from well-known CO poisonings. Recent improvement of catalytic activity in methanol oxidation from the ensemble effect of Pt with Au and Ru was reported[24]. By controlling the coverage of second metal on Pt catalysts from the electro-deposition, quantitative analysis of catalytic activity with the degree of coverage was successfully done. The Au core in our Au/Pt core/shell nanowires does not meet previous criteria for Au catalysts with activities for electrocatalysis: Au nanoparticle size should be smaller than 5 nm, or the Au nanoparticles should be conjugated with active oxide supports[25]. However, as we confirmed in Chapter 3-10, the as-prepared Au nanowires showed excellent catalytic activity for CO oxidation despite the larger diameter sizes of up to 40 nm.

Mostly, research on fuel cell anodes has been focused on methanol oxidation because methanol is the simplest alcohol that overcomes the storage problem of hydrogen gas with much higher energy density than that of compressed hydrogen. Due to the difficulty in breaking C-C bond in ethanol, the application of ethanol in low temperature fuel cell anode material has been limited despite several advantages of ethanol fuel cells: (i) higher mass energy density (8.1 kW•h/kg) than methanol (6.1 kW•h/kg), (ii) less toxic and more accessible than methanol, and (iii) renewable fuel produced from biomass[26]. Thus, we tested Au/Pt core/shell nanowires in ethanol electro-oxidation reaction (EER) by utilizing the Au core for CO oxidation to prevent Pt shell catalyst from decaying to confirm the ensemble effects.

Figure 6.12 (a) represents polarization curves of Au, Au/Pt core/shell nanowires, and the commercial Pt/C catalysts on ethanol oxidation in O_2 saturated KOH solution at 1600 rpm. The Au nanowires do not show EOR activity because Au itself cannot initiate the breakage of chemical bonds in ethanol molecule. The activity of commercial Pt/C is much lower than that of other Au/Pt core/shell nanowires because the surface of Pt is blocked from intermediate species such as CO and CHO produced from the breakage of ethanol. The enhancement of specific activity of Au/Pt core/shell nanowires, which is normalized by the electrochemical surface area, is strong evidence of the ensemble effect of Au in ethanol oxidation reaction. The dissociative adsorption of ethanol undoubtedly occurs only on the active site of Pt surface both in commercial Pt/C and Au/Pt core/shell nanowires. The higher current density in Au/Pt core/shell nanowires could be explained from the dual function model; The Au atoms strongly adsorb hydroxyl species (OH_{ads}), which can oxidize the CO_{ads} on Pt sites and result in recovery of active Pt surfaces. Further analysis on the surface structure of Au and Pt atoms during the electro-oxidation and the final products of the reaction is under study.

As shown in Fig. 6.12 (b), at potential 0.5 V vs. RHE, the specific activity of Au/Pt core/shell nanowires with a Au:Pt atomic ratio of 2.6:1 was greater than that of commercial Pt/C about 8.3 times. The dendritic Pt shell on the surface of Au nanowires increases the available Pt surface area on Au core more than the increase in mass. Those enhancements of catalytic activity of Au/Pt core/shell nanowires with increased Pt shell thickness contradicts general theory of Au-Pt interfaces that a thin Pt shell provides a greater number of Pt-Au interfaces per Pt atoms in typical monolithic Pt shell[4].

The chronoamperometry measurement on Fig. 6.12(c) clearly visualizes the differences in durability of CO poisoning effect on the surface of Pt. From the time point 0 second, with the beginning of continuous oxidation of ethanol at 0.5 V vs. RHE, the tenacious accumulation of CO intermediate on the surface of the Pt catalysts in the absence of removal of CO in an adequate rate abruptly decreases the activity of Pt. The slope of current density with time represents the susceptibility of the Pt catalysts to CO poisoning. Even the potential 0.5 V, which is far from the oxidation of CO on the surface of Au, the existence of Au core retards the fast decay of catalysts.

The comparison of activity of Au/Pt core/shell nanowires with 1:1 atomic ratio both in acidic and alkaline solution clearly showed reduced activity of nanowires (Fig. 6.13) in acidic conditions similar to other Au-Pt systems for electocatalysis[27]. Therefore the Au/Pt core/shell nanowires are more adequate in applications alkaline fuel cell electrodes.

6-9. Conclusion

Further modification of Au nanowires with Pt^{4+} resulted in Au/Pt core/shell nanowires with well-defined Pt surfaces. The as-synthesized nanowire solution provided homogeneous nanowires with uniform shell thickness. The shell thickness was also successfully tuned by changing the concentration of Pt^{4+} ions and the amount of ascorbic acid as reducing agents. Both EDX and ICP-OES results confirmed the atomic ratio of Au core: Pt shell, and XRD data showed a Au-like pattern with a small shoulder peak at higher 2θ region. The UV-Vis absorption and CV measurement of Au/Pt core/shell nanowires confirmed the full coverage of the Au surface by a Pt shell in nanowires of 1:1 atomic ratio. The electro-catalytic activity study was carried out on the surface of Au core, Au/Pt core/shell with various shell thickness, and commercial Pt/C nanowires. The Au/Pt core/shell nanowires with atomic ratio of 1:1 showed excellent catalytic activities both in the oxygen reduction reaction (application in fuel cell cathode) and the ethanol oxidation reaction (application in fuel cell anode) compared to commercial Pt/C under alkaline solution. The Au/Pt core/shell nanowires could be utilized in low temperature fuel cell electrodes for both in anodes and cathodes. From the synergistic interaction between Au and Pt, promotional activities were confirmed through electro-chemical measurements. Moreover, the existence of M13 phage as core material also significantly reduces the cost for the preparation of catalysts from the high conversion efficiency of Au with the enhanced durability of Pt catalysts.

6-10. References

1 Jeong, U., Kim, J.-U., Xia, Y. & Li, Z.-Y. Monodispersed Spherical Colloids of Se@CdSe: Synthesis and Use as Building Blocks in Fabricating Photonic Crystals. *Nano Lett.* **5**, 937-942 (2005).

2 Nutt, M. O., Hughes, J. B. & Wong, M. S. Designing Pd-on-Au Bimetallic Nanoparticle Catalysts for Trichloroethene Hydrodechlorination. *Environ. Sci. Technol.* **39**, 1346-1353 (2005).

3 Kim, J., Jung, C., Rhee, C. K. & Lim, T.-h. Electrocatalytic Oxidation of Formic Acid and Methanol on Pt Deposits on Au(111). *Langmuir* **23**, 10831-10836 (2007).

4 Zeng, J., Yang, J., Lee, J. Y. & Zhou, W. Preparation of Carbon-Supported Core-Shell Au-Pt Nanoparticles for Methanol Oxidation Reaction: The Promotional Effect of the Au Core. *J. Phys. Chem. B* **110**, 24606-24611, doi:10.1021/jp0640979 (2006).

5 He, W. *et al.* Pt-Guided Formation of Pt-Ag Alloy Nanoislands on Au Nanorods and Improved Methanol Electro-Oxidation. *J. Phys. Chem. C* **113**, 10505-10510 (2009).

6 Zhou, W. *et al.* Pt based anode catalysts for direct ethanol fuel cells. *Appl. Catal., B* **46**, 273-285 (2003).

7 Gasteiger, H. A., Markovic, N. M. & Ross, P. N. Electrooxidation of CO and H2/CO Mixtures on a Well-Characterized Pt3Sn Electrode Surface. *J. Phys. Chem.* **99**, 8945-8949 (1995).

8 Wang, Y., Mi, Y., Redmon, N. & Holiday, J. Understanding Electrocatalytic Activity Enhancement of Bimetallic Particles to Ethanol Electro-oxidation. 1. Water Adsorption and Decomposition on PtnM (n = 2, 3, and 9; M = Pt, Ru, and Sn). *J. Phys. Chem. C* **114**, 317-326 (2010).

9 Zhou, S., Jackson, G. S. & Eichhorn, B. AuPt Alloy Nanoparticles for CO-Tolerant Hydrogen Activation: Architectural Effects in Au-Pt Bimetallic Nanocatalysts. *Adv. Funct. Mater.* **17**, 3099-3104 (2007).

10 Lee, H. *et al.* Morphological Control of Catalytically Active Platinum Nanocrystals13. *Angew. Chem. Int. Ed.* **45**, 7824-7828 (2006).

11 Guo, S., Fang, Y., Dong, S. & Wang, E. High-Efficiency and Low-Cost Hybrid Nanomaterial as Enhancing Electrocatalyst: Spongelike Au/Pt Core/Shell Nanomaterial with Hollow Cavity. *J. Phys. Chem. C* **111**, 17104-17109 (2007).

12 Winter, M. & Brodd, R. J. What Are Batteries, Fuel Cells, and Supercapacitors? *Chem. Rev.* **104**, 4245-4270 (2004).

13 Wang, S., Kristian, N., Jiang, S. & Wang, X. Controlled synthesis of dendritic Au@Pt core@shell nanomaterials for use as an effective fuel cell electrocatalyst. *Nanotechnology* **20**, 25605 (2009).

14 Teranishi, T., Hosoe, M., Tanaka, T. & Miyake, M. Size Control of Monodispersed Pt Nanoparticles and Their 2D Organization by Electrophoretic Deposition. *J. Phys. Chem. B* **103**, 3818-3827 (1999).

15 Zhou, S., Varughese, B., Eichhorn, B., Jackson, G. & McIlwrath, K. Pt-Cu Core-Shell and Alloy Nanoparticles for Heterogeneous Reduction: Anomalous Stability

and Reactivity of a Core-Shell Nanostructure13. *Angew. Chem. Int. Ed.* **44**, 4539-4543 (2005).

16 Jose, D. & Jagirdar, B. R. Au@Pd Core-Shell Nanoparticles through Digestive Ripening. *J. Phys. Chem. C* **112**, 10089-10094 (2008).

17 Zhou, W. & Lee, J. Y. Highly active core-shell Au@Pd catalyst for formic acid electrooxidation. *Electrochem. Commun.* **9**, 1725-1729 (2007).

18 Harpeness, R. & Gedanken, A. Microwave Synthesis of Core/Shell Gold/Palladium Bimetallic Nanoparticles. *Langmuir* **20**, 3431-3434 (2004).

19 WangWang *et al.* Monodispersed Core/Shell Fe3O4@Au Nanoparticles. *J. Phys. Chem. B* **109**, 21593-21601 (2005).

20 Yano, K. *et al.* Synthesis and Characterization of Magnetic FePt/Au Core/Shell Nanoparticles. *J. Phys. Chem. C* **113**, 13088-13091 (2009).

21 Xu, Z., Hou, Y. & Sun, S. Magnetic Core/Shell Fe3O4/Au and Fe3O4/Au/Ag Nanoparticles with Tunable Plasmonic Properties. *J. Am. Chem. Soc.* **129**, 8698-8699 (2007).

22 Mukerjee, S. & McBreen, J. An In Situ X-Ray Absorption Spectroscopy Investigation of the Effect of Sn Additions to Carbon-Supported Pt Electrocatalysts: Part I. *J. Electrochem. Soc.* **146**, 600-606 (1999).

23 Bard, A. J., Faulkner, L.R. *Electrochemical Methods Fundamentals and Applications*. (Wiley).

24 Du, B. & Tong. A Coverage-Dependent Study of Pt Spontaneously Deposited onto Au and Ru Surfaces: Direct Experimental Evidence of the Ensemble Effect for Methanol Electro-Oxidation on Pt. *J. Phys. Chem. B* **109**, 17775-17780 (2005).

25 Valden, M., Lai, X. & Goodman, D. W. Onset of Catalytic Activity of Gold Clusters on Titania with the Appearance of Nonmetallic Properties. *Science* **281**, 1647-1650 (1998).

26 Vigier, F., Coutanceau, C., Perrard, A., Belgsir, E. M. & Lamy, C. Development of anode catalysts for a direct ethanol fuel cell. *J. Appl. Electrochem.* **34**, 439-446 (2004).

27 Tang, W., Jayaraman, S., Jaramillo, T. F., Stucky, G. D. & McFarland, E. W. Electrocatalytic Activity of Gold#Platinum Clusters for Low Temperature Fuel Cell Applications. *J. Phys. Chem. C* **113**, 5014-5024 (2009).

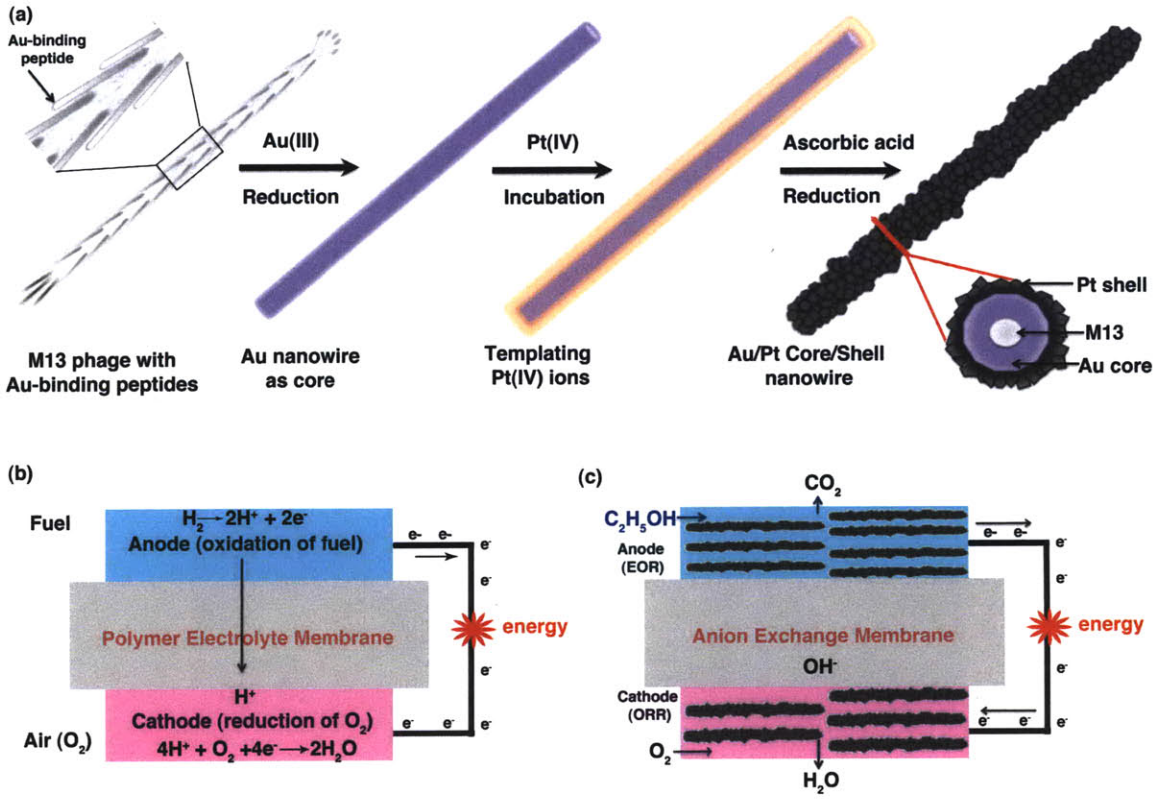

Figure 6.1 Schematic diagram for the preparation of Au/Pt core/shell nanowires and the virus fuel cells. (a) The M13 phage with specific Au-binding peptide motif was used for the preparation of Au nanowires as described in previous chapter. As-prepared Au nanowires were slightly sonicated to make homogeneous solution. The Pt^{4+} ions were added to the Au nanowire dispersion and incubated for two hours at room temperature. To reduce the Pt^{4+} ions, excess ascorbic acid was introduced and the solution was kept in 50 °C oven to make Pt shell composed of small Pt nanoparticles over Au core. (b) Simple low temperature fuel cell diagram. (c) Virus fuel cell from Au/Pt core/shell nanowires with different Pt loading as catalysts in both electrodes.

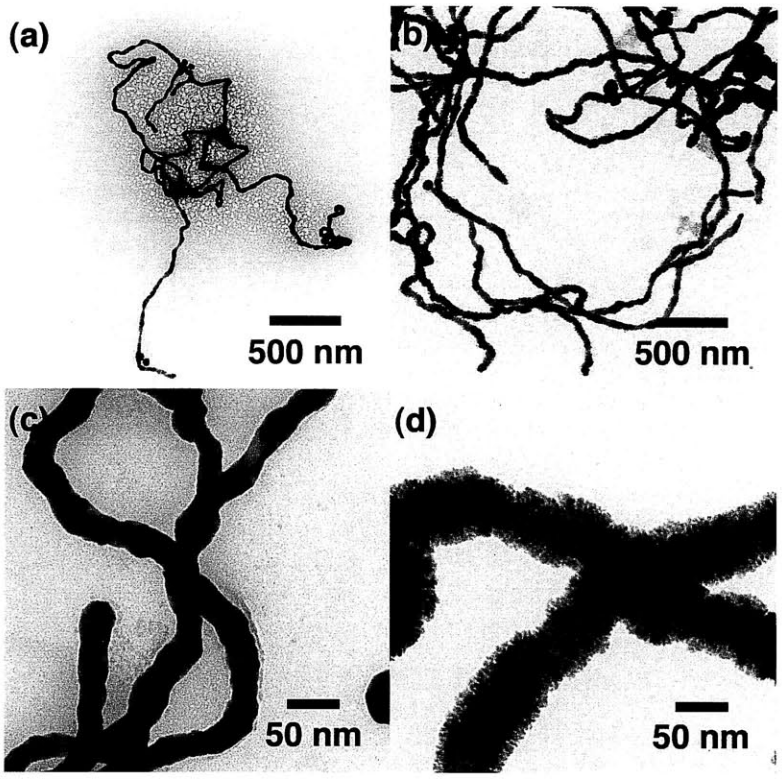

Figure 6.2 TEM images of Au core and Au/Pt core/shell nanowires. The TEM images in the first row are (a) Au core and (b) Au/Pt core/shell nanowires taken at 6,800x magnification. The diameter of nanowires is clearly increased with the formation of Pt shell. The images (c) and (d) were taken at 50,000x magnification. The plain surface of Au core (c) is completely covered with Pt shells (d) after the formation of Pt shell.

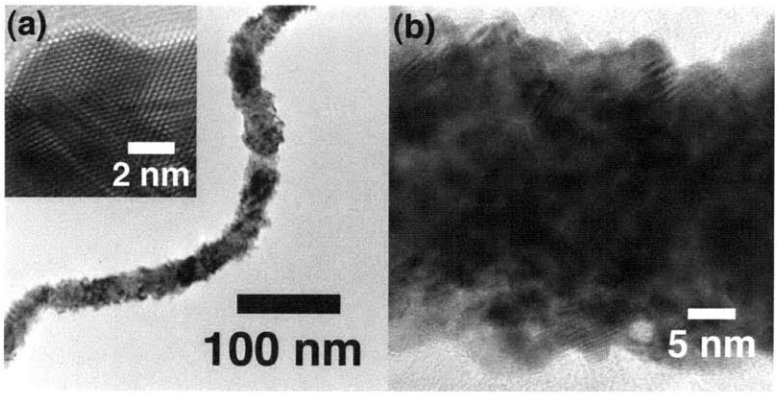

Figure 6.3 High-resolution TEM images of Pt shell. (a) High-resolution TEM image of Au/Pt core/shell nanowires are covered with high-crystalline Pt nanoparticles shown in inset image. (b) The Pt nanoparticles were grown dendritically with average particle size about 2-3 nm.

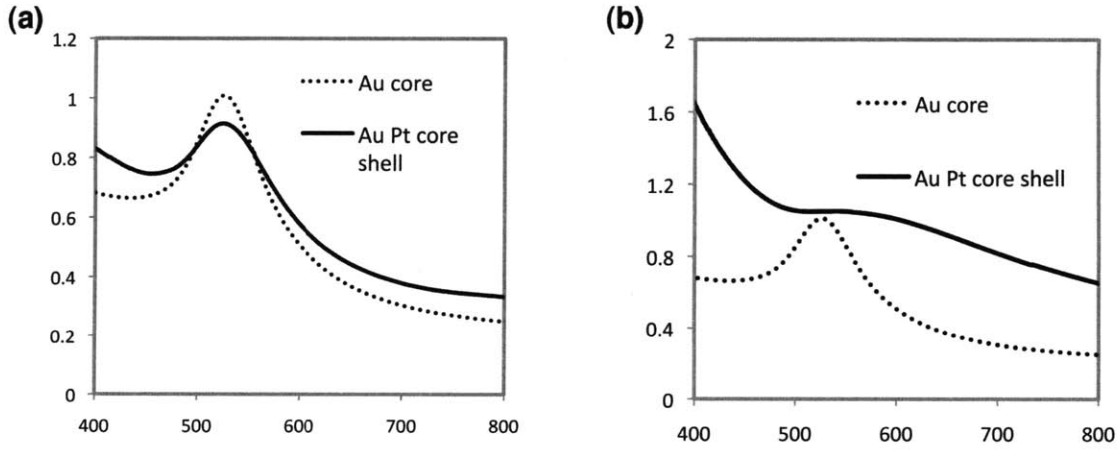

Figure 6.4 UV-Vis absorption spectra of Au/Pt core/shell nanowires with different shell thickness. (a) Au/Pt core/shell nanowires with Au:Pt atomic ratio of 2.6:1 showed slightly broad peak of transversal absorption at 520 nm and started to absorb light with shorter wavelength (< 450 nm). (b) With increased Pt atomic concentration (Au:Pt=1:1), the shell thickness was also enlarged and the absorption pattern was completely changed: the specific Au transversal absorption peak around 520 nm was shielded perfectly and the characteristic peak from Pt nanoparticles appeared.

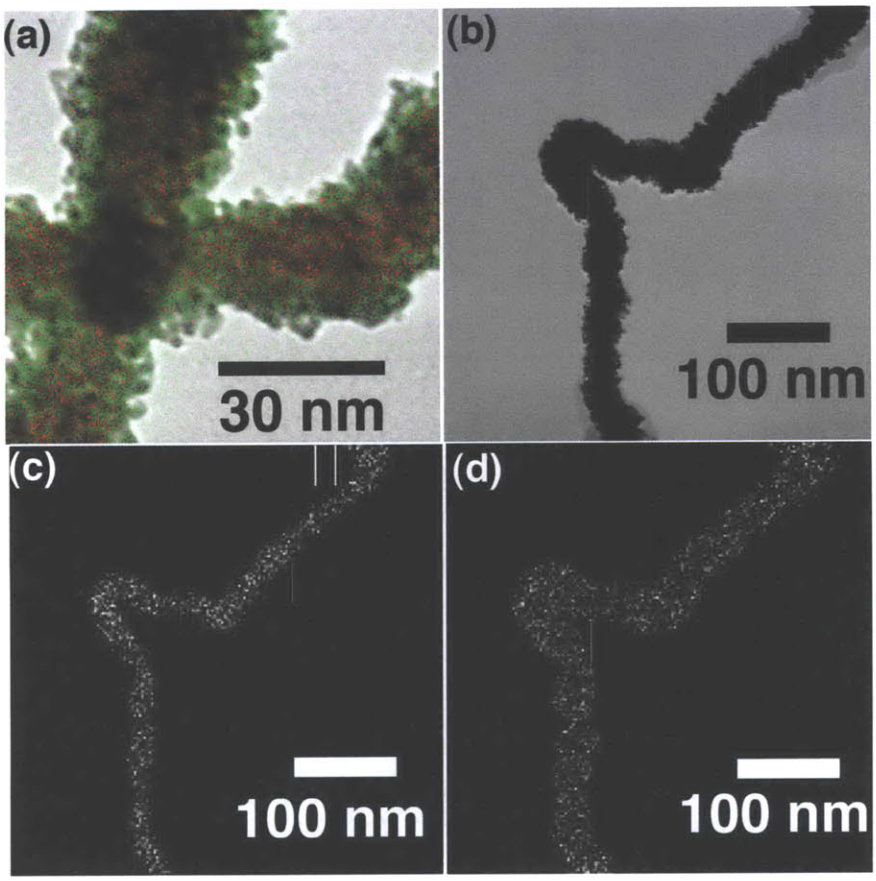

Figure 6.5 TEM analysis confirming the core/shell structures. (a) The electron mapping of two different atoms [green: Au, red: Pt] on the surface of Au/Pt core/shell nanowires show the distribution of Au and Pt. The red spots located in the middle of wire are from the shell layer on top of the nanowires from the perpendicular view to zone axis. (b) Dark field imaging of Au/Pt core/shell nanowires. (c) Selective mapping of Au under dark field confirmed existence of Au atoms close to center of nanowires as core material. (d) Pt atoms are more dissipated than Au.

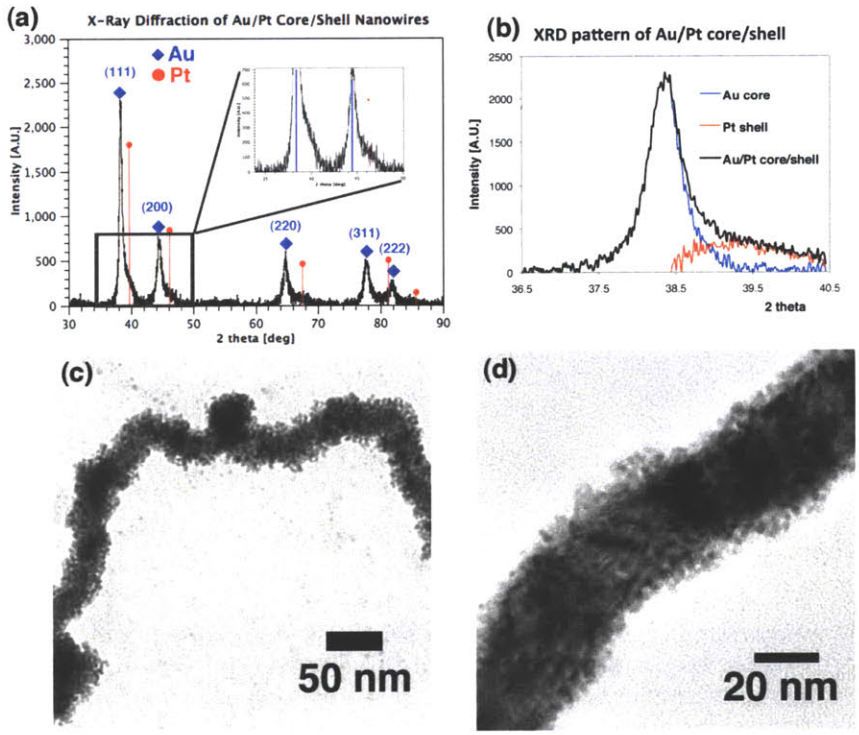

Figure 6.6 Representative XRD Result from Au/Pt core/shell nanowires. (a) The XRD peaks from nanowires with 1.8:1 atomic ratio of Au:Pt exhibits patterns close to Au. The blue diamonds are the main peaks of pure Au and the red circles for Pt from the JCPDS data. The Au main peaks are not symmetric and shoulder peaks are followed at the edges in the direction of larger 2θ. The inset image of (a) clearly shows the existence of shoulder peak near the Pt peak position. (b) The first peak centered at Au (111) was divided into the sharp and symmetric Au peak (blue) and the broad Pt peak [8]. (c) and (d) are the TEM image of Au/Pt core/shell Nanowires used for the XRD sample preparation. Homogeneous structure (c) with relatively thin Pt shell (d) is observed.

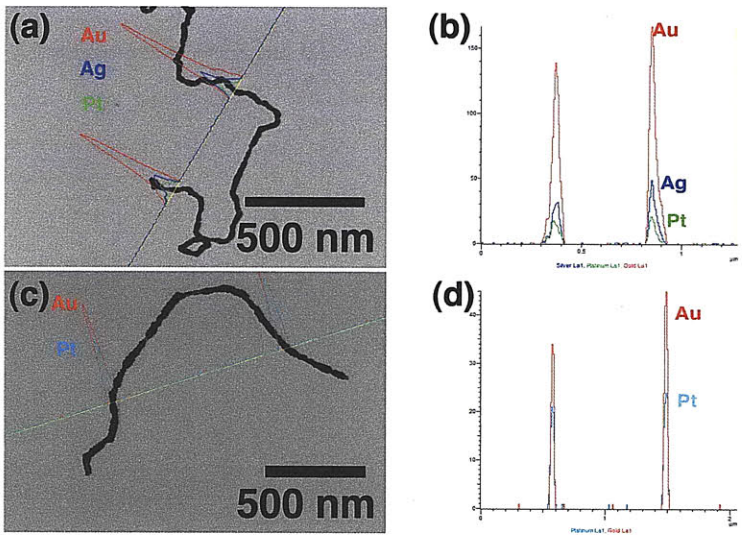

Figure 6.7 Line-scanning result of Au/Pt core/shell nanowires prepared at different temperature. (a) Room temperature synthesis of Pt shell from the same Au nanowire as core material resulted in Au:Pt atomic ratio of 13:1. (b) Raising the reaction temperature to 50 °C while keeping other conditions the same increased the amount of Pt on Au nanowires.

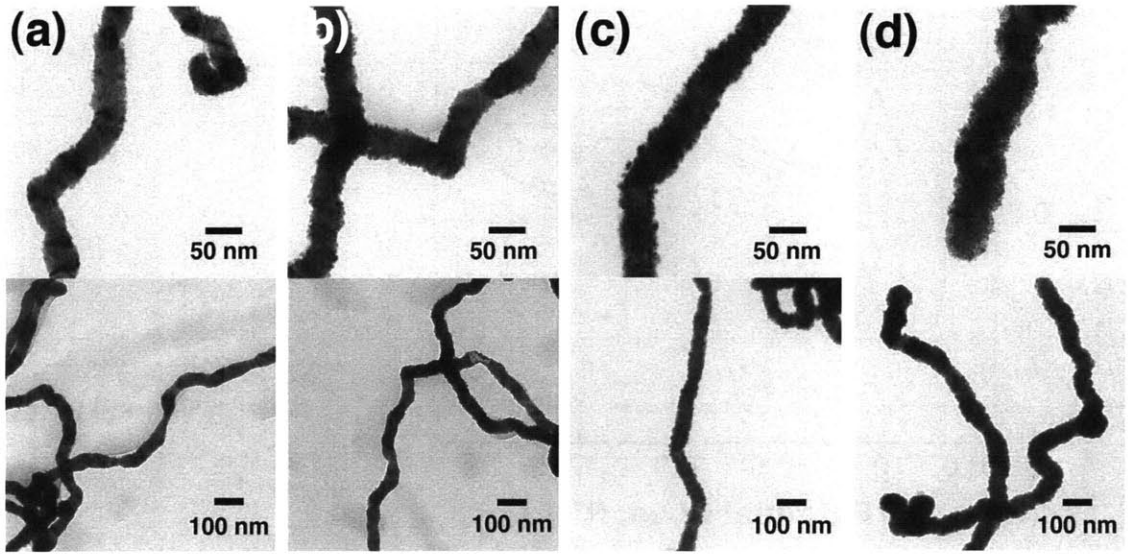

Figure 6.8 TEM images of Au/Pt core/shell nanowires with different shell thickness. The Pt atomic ratio was increased systematically from (a) to (d). The atomic ratios of each sample is (a): 2.6:1, (b): 1.8:1, (c): 1:1, and (d): 1:1.2. The TEM images shown at the first row were taken from 50,000X magnification showing surface morphologies with increasing roughness with increasing Pt shell thickness (the atomic ratio). The second row represents the homogeneity of nanowires at lower magnification of each sample shown at first row.

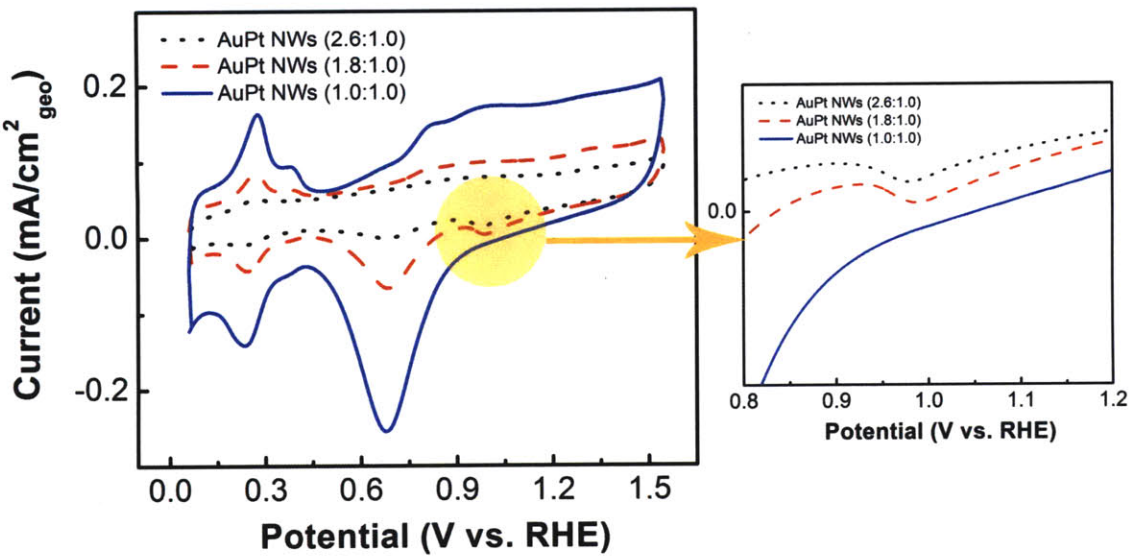

Figure 6.9 Cyclic voltammograms of Au/Pt core/shell nanowires with various shell thicknesses. The CV measurement was done on Au/Pt core/shell nanowires with atomic ratio of Au:Pt (2.6:1, 1.8:1, and 1:1) deposited on GCE in Ar-saturated alkaline solution (0.1 M KOH) at 50 mV/s scan rate. The peak around 0.6V vs. RHE is characteristic peak of reduction of Pt oxides and ~1.0 V vs. RHE is characteristic reduction peak of Au-oxide formed during the forwarding scan. The peak disappeared in Au/Pt core/shell nanowires with 1:1 atomic ratio as seen in magnified graph on right side (solid blue line). The difference of integrated peak area was both from the active surface area of nanowires and the deviation of loading amount.

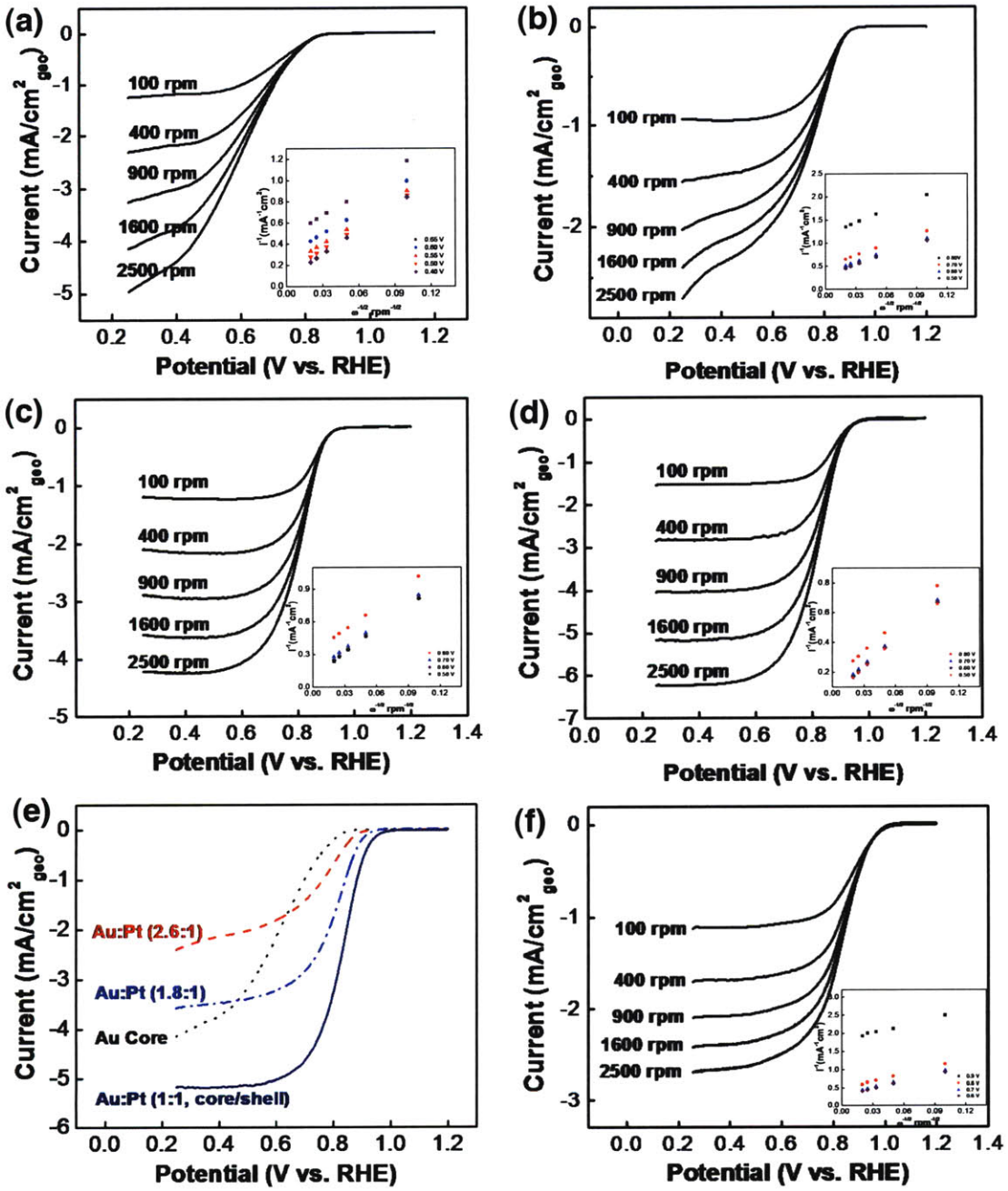

Figure 6.10 RDE voltammograms of Au, Au/Pt core/shell, and commercial Pt/C nanowires on GCE in O_2 saturated 0.1 M KOH solution (scan rate: 10 mV/s). The rotating speed was ranged from 100 rpm to 2500 rpm in all cases (a): Au core, (b): Au/Pt core/shell with atomic ratio of Au:Pt =2.6:1.0, (c) Au/Pt core/shell with atomic ratio of Au:Pt =1.8:1.0, (d) Au/Pt core/shell with atomic ratio of Au:Pt =1.0:1.0, and (f): commercial Pt/C [14]. (e) The polarization curves of different nanowires show potential shift with the increased Pt amounts.

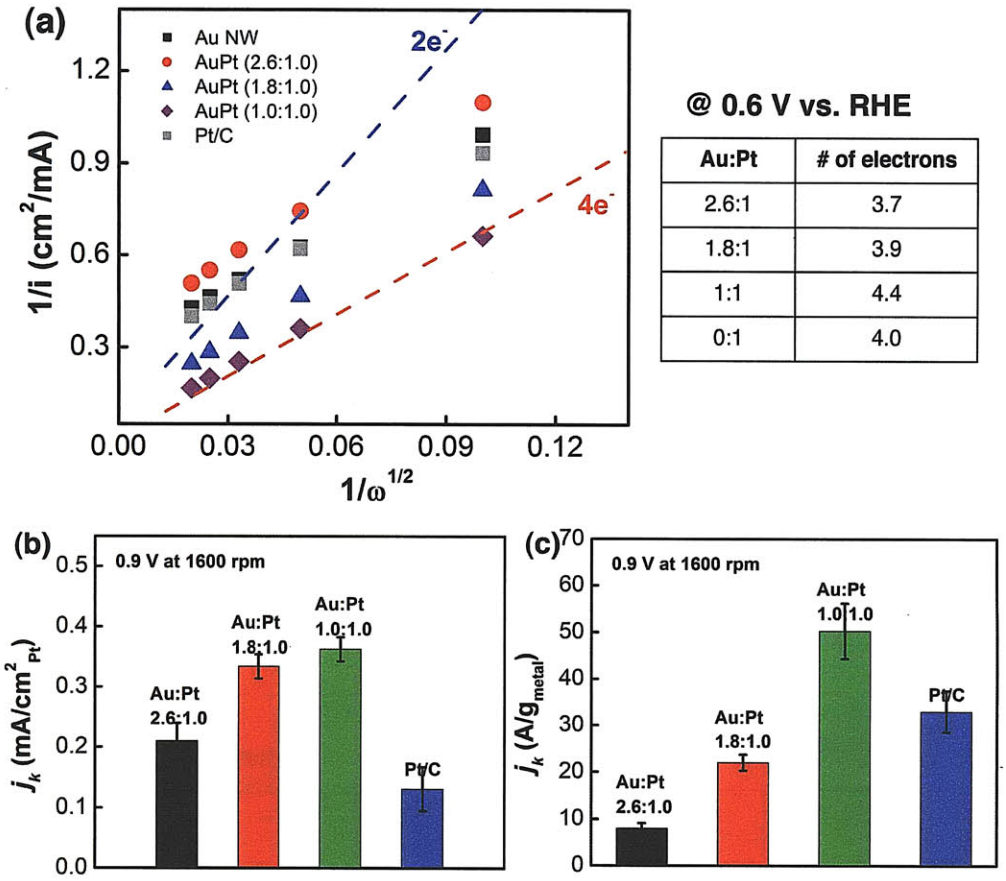

@ 0.6 V vs. RHE

Au:Pt	# of electrons
2.6:1	3.7
1.8:1	3.9
1:1	4.4
0:1	4.0

Figure 6.11 Electrocatalytic properties on O_2 reduction reaction of Au/Pt core/shell nanowires and commercial Pt/C. (a) The Koutecky-Levich plot provided number of electrons participate in the reduction of O_2, which is systematically increased from 3.7 to 4.4. The commercial Pt/C resulted electron number 4, a good agreement with reports before. (b) The specific activity of Pt compared at potential 0.9V vs. RHE confirmed increased activity with the thickness of Pt shell. The core/shell nanowires with Au:Pt atomic ratio of 1:1 showed higher specific activity than 2.8 times higher. (c) The mass activities of Au/Pt core/shell nanowires calculated from the total metal mass (the sum of Au and Pt in core/shell nanowires) also confirmed the better activity of Au/Pt core/shell about 1.5 times.

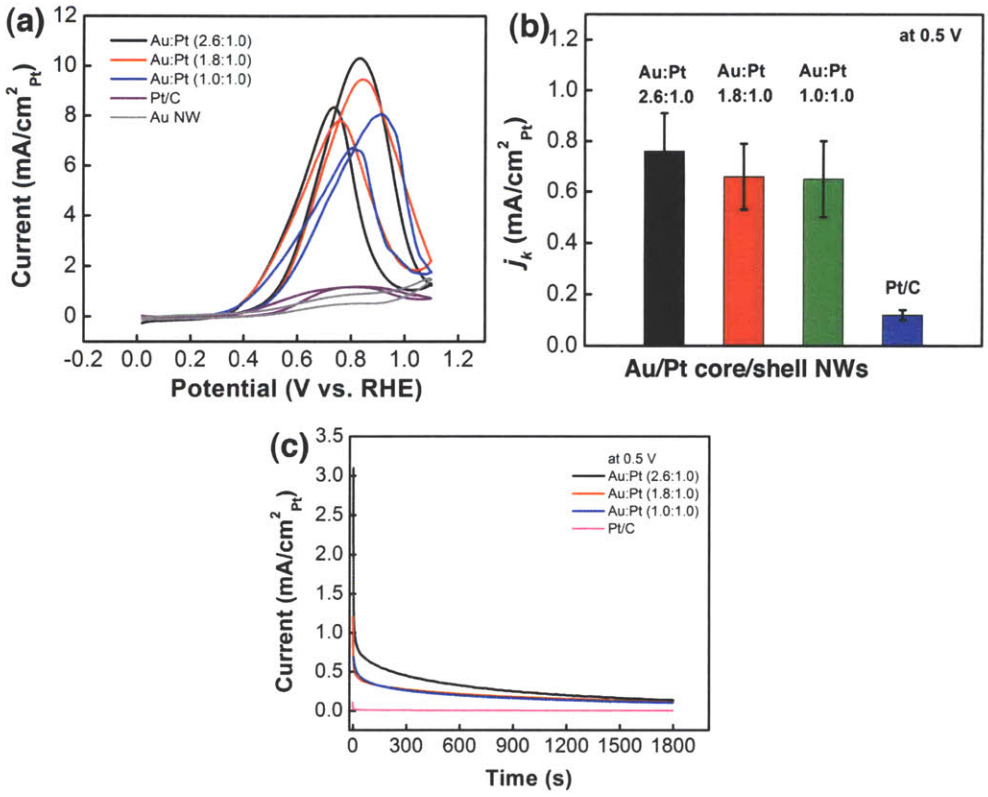

Figure 6.12 Ethanol electro-oxidation reaction (EOR) on Au core, Au/Pt core/shell with various shell thickness, and commercial Pt/C nanowires. (a)Ethanol oxidation polarization curves from nanowires in 1.0 M ethanol and 0.1 M KOH solution at 50 mV/s scan rate. (b) Comparison of specific activity of the Au/Pt core/shell nanowires and commercial electrocatalyst Pt/C at 0.5 V vs. RHE. The specific activity is normalized by the electrochemically active surface area of Pt. (c) Chronoamperometry measurements of ethanol oxidation on Au/Pt core/shell nanowires and commercial Pt/C RDE in Ar-saturated 0.1 M KOH.

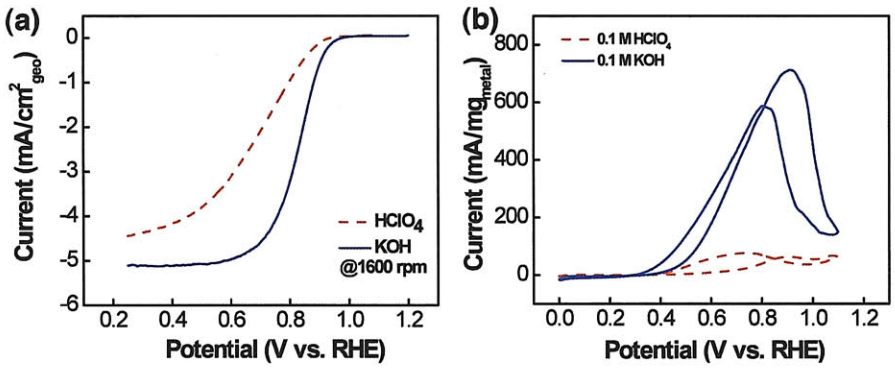

Figure 6.13 Activity tests of Au/Pt core/shell nanowires in acidic conditions. (a) Oxygen reduction reaction on Au/Pt core/shell nanowires with Au:Pt atomic ratio of 1:1 showed negative shift in onset potential in acidic solution (red dotted lines). (b) Ethanol electro-oxidation scanning in acidic condition also resulted in much reduced current density than in alkaline solution.

Au:Pt ratio	Au [mM]	Pt^{4+} [mM]	Ascorbic acid [mM]
1:0	0.274	0	0
2.6:1	0.249	0.30	6.06
1.8:1	0.238	0.43	8.70
1:1	0.228	0.56	11.1

Table 6-1. Summary of concentration for the preparation of Au/Pt core/shell nanowires with various shell thickness.

Au:Pt	Au [ppm]	Pt [ppm]
2.6:1	54.6	20.7
1.8:1	61.5	33.3
1:1	64.5	62.7
Au core	67	0

Table 6-2. Concentration information of Au/Pt core/shell nanowires used for electrochemical measurements.

Au:Pt catalyst	loading		Coulomb [μC_{Pt}]	ESA of Pt [cm^2_{Pt}]	Onset potential [V vs. RHE]
	Au	Pt			
2.6:1	1.09	0.41	12.6±2.1	0.06±0.01	0.92
1.8:1	1.23	0.67	26.1±0.8	0.124±0.004	0.95
1:1	1.29	1.25	73.5±6.3	0.35±0.03	0.99
0:1	0	3.6	218.4±16.8	1.04±0.08	1.01

Table 6-3. Summary of electrochemical measurement data of Au/Pt core/shell nanowires with various shell thickness and commercial Pt/C.